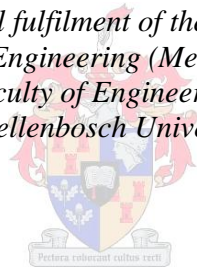# Design and performance evaluation of a HYDROSOL space heating and cooling system

by

Johann Pierre Terblanche

Thesis presented in partial fulfilment of the requirements for the degree
of Master of Engineering (Mechatronic) in the
Faculty of Engineering at
Stellenbosch University

Supervisor: Prof HCR Reuter

March 2015

Declaration

By submitting this thesis electronically, I declare that the entirety of the work contained therein is my own, original work, that I am the sole author thereof (save to the extent explicitly otherwise stated), that reproduction and publication thereof by Stellenbosch University will not infringe any third party rights and that I have not previously in its entirety or in part submitted it for obtaining any qualification.

Date: ....

Abstract

Space heating and cooling, as required for chicken poultry farming, is an energy intensive operation. Due to the continuous rise in the prices of fossil fuel, water and electricity, there is a need to develop renewable and sustainable energy systems that minimise the use of fuel or electricity, for heating, and water, for cooling of air. The HYDROSOL (HYDro ROck SOLar) system, developed at Stellenbosch University, is such a renewable energy system that potentially provides a low cost solution. Instead of using conventional gas and electricity heaters for the heating of air during winter, the HYDROSOL system collects solar heat, stores it in a packed bed of rocks and dispatches the heat as required. During hot summer days, when cooling is needed, the rocks are cooled during the night when the ambient temperatures are low and/ or by evaporative cooling by spraying water onto them. During the day, hot air is then cooled when it passes through the colder rocks with minimal water consumption compared to current systems. In this thesis, a prototype of the HYDROSOL system is presented, designed and built for experimental testing. A transient 2-D thermo flow model is developed and presented for the analytical and experimental performance evaluation of this system for solar heating and night air cooling operation. This model is used to conduct a parametric study on HYDROSOL to gain a better understanding of the operation and control of the system.

The HYDROSOL concept is intended to be used for heating and cooling of residential buildings, office suites, warehouses, shopping centres, food processing industries e.g. drying of foods, and various agricultural industries e.g. greenhouses. In this thesis, a HYDROSOL system is developed mainly for poultry broiler houses in South Africa focussing on convective dry cooling, charging the rock bed with night-time ambient air, and convective heating, harvesting solar heat during the day, with different modes of operation available.

Opsomming

Ruimte verhitting en verkoeling, soos benodig vir hoender pluimvee boerdery, is 'n energie intensiewe bedryf. As gevolg van die voortdurende styging in fossiel brandstof-, water- en elektrisiteitpryse, het 'n behoefte ontstaan om hernubare en volhoubare energie-stelsels te ontwikkel wat minder brandstof of elektrisiteit, vir verhitting, en water, vir verkoeling van lug, gebruik. Die HYDROSOL (HYDro ROck SOLar) stelsel, wat ontwikkel is by die Universiteit van Stellenbosch, is 'n hernubare energie-stelsel wat 'n potensiële lae koste oplossing bied. In plaas daarvan om konvensionele gas en elektrisiteit verwarmers vir verhitting van lug gedurende die winter te gebruik, maak HYDROSOL gebruik van son warmte, stoor dit in `n gepakte bed van klip en onttrek die warmte soos benodig. Gedurende die warm somer dae wanneer verkoeling benodig word, word die klippe gedurende die nag, met kouer omgewings lug en/of met verdampingsverkoeling, deur water op die klippe te spuit, afgekoel. Gedurende die dag word warm lug afgekoel deur die lug oor die koue klippe te forseer met minimale waterverbruik in vergelyking met huidige stelsels. 'n Prototipe van die HYDROSOL word voorgestel, ontwerp en gebou vir eksperimentele doeleindes. 'n 2-D tyd afhanklike termo- vloei model word voorgestel vir die analitiese en eksperimentele verrigting evaluering vir son verhitting en nag lug verkoeling. Hierdie model word gebruik om 'n parametriese studie te doen om die werking en beheer van HYDROSOL beter te verstaan.

Die HYDROSOL stelsel is bedoel om die verwarming en verkoeling vereistes van residensiële geboue, kantoor areas, pakhuise, winkelsentrums, voedsel verwerking nywerhede, soos bv. die droging van voedsel, en verskeie landboubedrywe, soos bv. kweekhuise, te bevredig. In hierdie tesis word 'n HYDROSOL stelsel, hoofsaaklik vir pluimvee kuikenhuise in Suid- Afrika, ondersoek en fokus op die droë verkoeling, deur die rotsbed te laai gedurende die nag, asook droë-verhitting, wat gebruik maak van son energie gedurende die dag en kan beheer word op verskillende maniere.

Acknowledgements

I would like to thank the following people for all the support, conversations and jokes that helped me to find inspiration through this project.

- Prof. Reuter for the opportunity, inputs, guidance, support and keeping me motivated throughout the project.
- Prof. Kröger for the valuable time and inputs. I am privileged for the short time we have spent together on this project.
- Gené Pienaar for all her patience, support and endless love.
- NRF for providing me with a bursary.
- Mr. CJ Zietsman and the rest of the workshop team who always had time and squeezed in my late requests.
- The people in the Lasraam office who had to deal with all the moods.
- My friends and family for their love and support.

Contents

List of figures

List of tables

x

Nomenclature

A	Area/ Ergun constant	[m^2]
a_{Ri}	Interfacial rock area	[m^{-1}]
Af	Anti-freeze	
B	Ergun constant	
c_p	Specific heat at constant pressure	[J/kgK]
c_v	Specific heat at constant volume	[J/kgK]
D	Diameter/ diffusion coefficient	[m] or [m^2/s]
DNI	Direct normal irradiation	[W/m^2]
EOT	Equation of time	[min]
F	Force	[N/m]
f	Friction factor	
G	Mass flux	[kg/m^{2}s]
g	Gravitational acceleration	[m/s^2]
GHI	Global horizontal irradiation	[W/m^2]
H	Height	[m]
h_c	Convective heat transfer coefficient	[W/m^{2}K]
h_d	Mass transfer coefficient	[kg/m^{2}s]
I	Irradiation	[W/m^2]
i	Enthalpy	[J/kg]
i_{fg}	Latent heat	[J/kg]
k	Thermal conductivity	[W/mK]
L	Length	[m]
LCT	Local clock time	[min]
LC	Longitude correction	[min]
m	Mass flow rate, mass	[kg/s] or [kg]

n	Quantity	
P	Power, position	[W]
p	Pressure	[N/m^2] or [Pa]
PCM	Phase change material	
Q	Heat transfer rate/ volumetric flow rate	[W] or [m^3/s]
R	Ratio	
r	Co–ordinate or distance	[m]
T	Temperature	[K] or [°C]
t	Time	[s] or [min]
u	Velocity	[m/s]
V	Voltage or volume	[V] or [m^3]
W	Width	[m]
w	Humidity ratio	[kg H_2O/kg dry air]
x	Co-ordinate or distance/ angle	[m]
y	Co-ordinate or distance	[m]
z	Co-ordinate or distance	[m]

Greek symbols

α	Altitude angle/ absorptivity	[°]
β	Slope angle	[°]
γ	Azimuth angle	[°]
Δ	Differential	
ε	Emissivity/ void fraction	
η	Efficiency	
θ	Angle	[°]
μ	Dynamic viscosity	[kg/ms]

xii

ρ	Density	[kg/m^3]
σ	Boltzmann constant	[W/m^{2}K^4]
ϕ	Latitude angle	[°]
ω	Hour angle	[°]

Dimensionless groups

Bi	Biot number, $h_c d/2k_p$
Le_f	Lewis factor, $h_c/c_{pma}h_d$
NTU	Number of transfer units
Nu	Nusselt number, $h_c d/k$
Pr	Prandtl number, $\mu c_p/k$
Re	Reynolds number, $\rho u d/\mu$
Sc	Schmidt number, $\mu/\rho D$
Sh	Sherwood number, $h_D d/D$

Subscripts

a	Dry air, above
av	Mixture of dry air and water vapour
aRm	Position
b	Body, beam, below
c	Convective, cross sectional, cover, characteristic
co	Co-current
col	Collector
cp	Cover plate
$cross$	Cross-current
cv	Control volume

xiii

d	Diffusion
dp	Dew point
eff	Effective
f	Frictional
fr	Frontal
g	Gravity
I	Inner
i	Interfacial, incident, in
l	Left
L	Length
m	Mean
n	Normal
O	Outer
o	Out, object
p	Particle, plate, pumping, point
R	Rock
r	Radial, reflection, right
s	Solid, saturation, surface, solar
sky	Sky
surr	Surrounding
surf	Surface
tot	Total
u	Useful
v	Vapour, volume, volume equivalent
w	Water, wind
z	Zenith

1 Introduction

1.1 Background and motivation

The HYDROSOL (HYdro ROck SOLar) system, developed and patented at Stellenbosch University, is a cost effective and low maintenance renewable energy system for regulating air temperature in enclosed environments. This system requires no fuel and has minimal power and no or reduced water consumption compared to other conventional systems currently used. Conventional systems used in e.g. broiler houses, warehouses, offices, malls etc., have high fuel and/ or electricity and water consumption, which, due to the continuous rise in water, electricity and fossil fuel prices, drive up costs for space heating and cooling. When used as an air heater, the HYDROSOL system harnesses solar heat during the day time and stores it in a rock bed. When required, air can be heated as it passes through the rock bed. Similarly for cooling, cool ambient air is generally used at night time to cold charge the rock bed and is extracted from the bed when needed. To enhance the cooling, water can also be sprayed onto the rock bed to further cool the rocks and enhance the cooling capacity. An interesting application of the system, which is the focus of this research, is for chicken broiler houses in South Africa. The required air temperature in chicken broiler houses varies during the chick-to-chicken growth cycle and must be carefully monitored and controlled. This requires air heating during the winter, especially during the first two weeks, and cooling during summer which is generally achieved by means of fossil fuel fired air heaters and evaporative swamp cooler systems respectively. The HYDROSOL system is a single system that can replace these conventional heating and cooling systems.

South Africa has some of the highest direct solar irradiation levels in the world making it one of the most favourable countries for developing solar applications (Meyer and van Niekerk, 2012). The Northern Cape, some areas of the Free- State and North- West have been identified for best practical implementation of concentrating solar power plants because of these favourable conditions. Solar water heaters (SWHs) also spiked in popularity in 2009 after the South African government funded a program for installing one million SWHs in households and commercial buildings (Department of Energy, 2009)

Solar air heaters collect solar heat and transfer it to air passing over a heated absorber plate. Depending on the application, the heated air can be used directly in a space to be heated, passed through a heat exchanger or be stored as sensible heat in a storage medium. These storage mediums can either be solids, such as rocks or steel, liquids, such as oil and water or phase change material (PCM).

Ample work has been done in the field of energy storage in rock beds. Rocks are generally the cheapest storage medium and fairly easy obtainable in most places in South Africa, when compared to water and PCM, with the main concern only being the transport cost to site. The main deciding factor is however the initial and

1

operating cost of the system, and storage material should be selected accordingly. Another advantage of rocks is that it acts both as storage medium and heat transfer surface, eliminating the use of heat exchangers and associated efficiency losses. Rock beds have good heat transfer characteristics with air at low flow velocities and minimal maintenance once installed. While charging a rock bed from one end using the solar heat, a thermocline forms and can easily be controlled by adjusting air mass flow rate through a rock bed. Alkilani et al. (2011) cite a disadvantage of rock beds, that it cannot be charged and discharged simultaneously. This is based only on the reversed discharge of the rock bed and is not the case when the discharge occurs in the same direction as the charge operation.

According to Kalogirou (2009), the main requirements for rock bed storage are good thermal insulation, the apparatus should be sealed air tight and a low pressure drop over the packed bed is needed. Eckhof and Okos (1978) cite that water has heat storage to volume ratio five times greater than rock, but at much higher cost and maintenance such as corrosion and leakages.

Cold storage with rocks is also possible when temperatures cooler than ambient temperature are stored in the rock bed. Cold charge systems have been used in buildings where it is negatively charged during cheaper off peak electricity rates and extracts from it during peak times in order to save on operating costs.

Water coolers or evaporative coolers have been used especially in broiler houses to reduce the cost of cooling. This method proved to be effective even in areas that are quite humid. According to Ross (2010) a general rule of thumb is that an evaporative cooler is very practical in broiler houses if there is a difference of 20 °C between daytime highs and night-time lows.

As for the broilers, young chicks are poikilothermic and their internal temperature is controlled and usually matched by the environmental temperature. As they become older, they grow into homoeothermic birds, that can regulate their own body temperature and maintain a relatively constant body temperature regardless of their environment (Bioenergetics and growth, 2003). Broiler chickens in specific are reared for their meat, taking approximately 5-7 weeks in ideal in-house environmental conditions before reaching slaughter weight. It is thus important to effectively manage in-house environmental conditions to optimize flock performance and reduce cost of production.

According to guidelines from Kentucky Poultry Federation (1995) for broiler management, feed intake divided by chicken mass is a good indication of flock performance. Ross (2010) cites that the most important factor influencing feed conversion of chickens is the in-house conditions, where the main factors are ambient temperature, relative humidity and air velocity inside the broiler house.

When the temperature is too high, chickens reduce feed intake in order to limit heat production. Similarly when the temperature is too low, chickens increase their feed intake and use more of the feed energy to keep their bodies warm. Thus,

broiler chickens have an optimum growth rate when the in-house environmental conditions are maintained at a target temperature or in a range close to the target temperature, defined as the thermal comfort zone (TCZ). The TCZ is where chickens do not have to regulate their body temperature and can optimally convert feed to meat/ weight. Since chickens have no sweat glands, they use a panting technique to get rid of excess heat requiring more of their energy intake and thus reducing optimum growth rate. The target temperature typically changes during the growth cycle of the chickens and the TCZ widens as the chickens become older. Table 1 shows a typical guide for in-house temperature and humidity adapted from Cobb (2012) ranging from 34 °C on the first day to 18 °C at harvest time.

Not all of the energy that chickens take in is converted into meat. Some excess heat and moisture are produced by older chickens. During cooler periods, chickens can keep the house warm enough without adding supplemental heat. Ventilation becomes essential when temperature become slightly warmer and the excess heat produced by the broilers must be removed. Even during colder days, minimum ventilation is required to remove the carbon dioxide and prevent excessive ammonia levels in the house. According to Cobb (2012), the ammonia levels must be maintained below 10 ppm at all times.

More information regarding broiler houses and ideal in-house conditions as well as the economic impact for deviations from the ideal temperature range is given in Cobb (2012) and Ross (2010).

Table 1: Temperature and humidity guide for broilers

Age days	Relative humidity %	Temperature °C
{1}-7	30-50	34-31
8-14	40-60	31-27
15-21	40-60	27-24
22-28	40-60	24-21
29-35	50-70	21-19
36-42	50-70	19-18
42-…	50-70	18

1.2 Existing heating and cooling methods and concepts in broiler houses

Two types of heaters are typically used in poultry facilities: the forced air space heaters and radiant brooders. Figure 1.1 shows two types of forced air and radiation heaters. Figure 1.1 (a) is a gas, fuel or oil fired combustion heater that heats up air and distributes it effectively through the broiler house. It operates in a closed combustion cycle so that the air remains free of harmful gasses. The combustion gas is directed to the outside via chimneys. These heaters are usually combined with additional circulation fans installed in various positions in the broiler house to improve the distribution of warm air. These units are located inside the broiler house to reduce heat loss to the outside. Biomass- fuelled heaters operate in a similar way but typically burns wood pellets to generate heat. Air from the inside is heated and returned to the house through ducts.

Figure 1.1 (b) shows the unit and installation of a hot water convection heater. Water is typically heated by oil or gas powered boilers located on the outside of the broiler house. A fan circulates in-house air through the heat exchanger and heats up the air. The system is typically installed 1 m above the ground and distributes air through guided vanes. These types of units are usually located along the centre of the broiler house to distribute air more evenly.

(a) Combustion air heater

(b) Hot water convection heater

(c) Gas brooder

(d) Radiant tube heater

Figure 1.1: Conventional heating systems in broiler houses

4

Figure 1.1 (c) is a typical gas brooder used especially for young birds when a definite amount of heat is specified. The heater uses propane, natural gas or electric resistance elements and radiates the heat onto the broilers. This type of heater's height from the ground is adjusted as birds grow older and require less heat. Cobb (2012) recommends a visual management by observing the broilers. Proper conditions are found to be when the broilers are relaxed and evenly spaced whereas noisy or drowsy broilers indicate that temperatures are too cold or hot.

A radiant tube heater is shown in Figure 1.1 (d). This infrared heating system can use electricity, natural gas or propane. These types of heaters do not heat the entire house, but rather the surfaces the rays strike. Again, visual observations for proper brooding are necessary.

Cooling in broiler houses is usually achieved by a minimum ventilation, tunnel ventilation or evaporative cooling. South Africa typically has a moderate (24 °C – 30 °C) to hot (>30 °C) climate during the summer months. In order to cool the broiler house, tunnel cooling is probably the cheapest way of cooling since at the right wind velocity a "wind chill" effect is created. Wind chill is the effect of ventilation over the birds where the actual air temperature of the air remains the same but the temperature experienced by the birds is much lower. Ross (2010) recommends making use of the wind chill effect with ventilation when temperatures rise above 24 °C but extra cooling will be needed when temperatures exceed 30 °C. They give an example of air at 32 °C moving with a velocity of 2.54 m/s results in an effective temperature of 27 °C experienced by the broilers. The wind chill effect begins to disappear when temperatures rise above 35 °C and additional cooling, such as evaporative cooling, should be used since the wind chill effect would be heating the birds instead of cooling (Ross, 2010). Cobb (2012) presents a maximum air speed over the chicks based on their age as can be seen in Table 2.

Table 2: Maximum wind speed across broiler chickens (Cobb, 2012)

Age of chicks [days]	Maximum wind speed [m/s]
{1}-14	0.3
15-21	0.5
22-28	0.875
28+	1.75-3.0

Evaporative cooling is probably the most cost effective way to lower ambient air temperature especially in very hot weather. This type of cooling is achieved by two methods i.e. direct and indirect. An indirect evaporative cooler sprays water directly into a secondary air stream where the cool humid air is then passed over a heat exchanger carrying the primary air stream to be cooled. The primary air

stream leaves the heat exchanger at a lower temperature without added moisture while the air from the secondary stream is dumped. Direct evaporative cooling is achieved by bringing the primary air stream directly into contact with water. This can be achieved by spraying water as mist into the airstream or by wetting a porous material and forcing air through it. However, the effect of high temperature and humidity levels in the broiler house reduce the ability of the chicks to get rid of excess body heat since the heat is expelled by mainly removing moisture from their lungs through breathing into the air stream. Thus, the higher the relative humidity levels in the house, the lower the ability for the chicks to cool themselves.

Figure 1.2 (TradeKorea, 2014) shows an implementation of a direct evaporative cooler using porous pads for a typical broiler house. Ambient air is extracted through the wetted pads leaving at near saturated conditions. The air moves through the broiler house similar to the tunnel ventilation. Heat from the inside is transferred to the air having higher moisture content and leaves through the fans on the opposite side. The water quality in this application is vital since a bacterium tends to grow on the pads and thus lowers air quality. This can lead to serious health risks for the broilers and drastically lower flock performance. However, by combining evaporative cooling with a wind chill effect, the temperature experienced by chicks can even be further reduced.
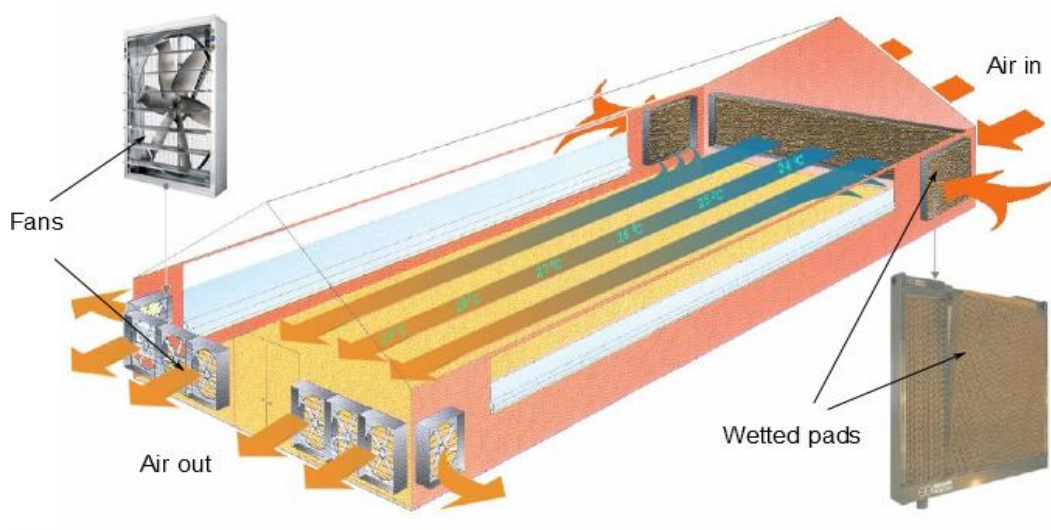
Figure 1.2: Evaporative cooler in a tunnel ventilation broiler house (TradeKorea, 2014)

For example, an evaporative cooling system with 75 % efficiency and outside relative humidity of 50 % can lower the ambient temperature from 35 °C to approximately 28 °C. This evaporative cooling combined with a wind chill tunnel ventilation effect can lower the temperature experienced by the broilers to approximately 23 °C (Ross, 2010) as shown in Figure 1.3.
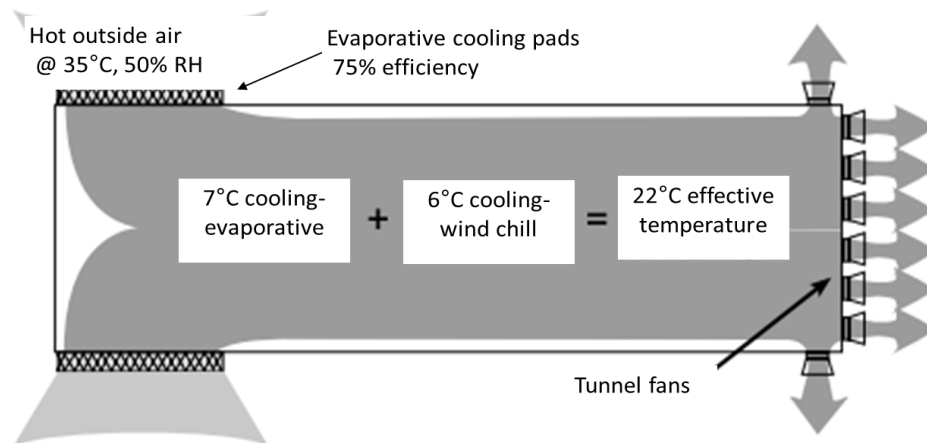
Figure 1.3: Evaporative cooling combined with wind chill effect

According to Cobb (2012), evaporative cooling should only be considered when temperatures rise to more than 28 °C and that evaporative cooling should be avoided before the chicks reach 28 days of age. Flushing of pads on a weekly basis is recommended. Fogging systems are installed inside the broiler house in two straight lines for broiler houses less than 14 m in width, otherwise 3 lines, equally spaced between the side walls. Common problems associated with this system is dripping of water and wetting the chicks.

Desired temperatures and ideal conditions can be more easily maintained in smaller areas. Half house brooding or division brooding are commonly used in broiler houses. This is when only half of the house is used, especially when chicks are in their early age stages, in order to reduce heating or cooling cost. Typically a heat retaining curtain is used to split the house and as the chicks grow older the size of the brooding area is increased to full house at approximately day 14 (Cobb, 2012). The effective temperature experienced by the birds can thus be described to a combined effect of; ambient temperature, relative humidity levels, wind speed across chicks, feather density and radiant heat.

Solar applications for heating purposes have been successfully implemented in some poultry applications. Some of the most common is designing the broiler house with one length wall directed towards the noon sun. Solar walls are fitted against the side wall acting as a solar air heater where an absorber plate heats up and transfer heat to the passing air. A typical wall mounted solar air heater is depicted in Figure 1.4 where a glass cover or other transparent materials are fitted on an insulated case with an absorber plate on the inside. Air from the enclosed environment is circulated (not necessarily) over the absorber plate and heats up. This setup is also commonly used in commercial and residential buildings. Different designs and configurations are possible operating on the same principle.
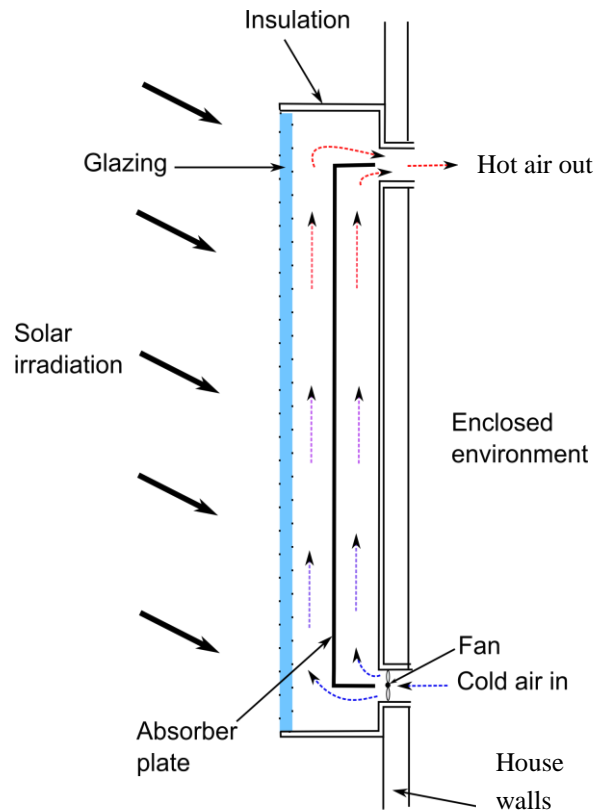
Figure 1.4: Typical wall mounted solar air heater

Other solar heat collecting devices such as parabolic troughs and solar air heaters in other configurations have been considered. These collecting devices are usually connected with a storage medium, such as rocks or water to extract heat during the time of when no solar radiation is available. Figure 1.5 adapted from Fawaz et al. (2014) shows a schematic of an existing hot water convective solar heating system used in poultry farms. The system collects solar heat with the parabolic trough with an antifreeze fluid as the heat transfer medium. The antifreeze moves through a heat exchanger inside a thermal storage tank. The thermal storage tank transfers heat to a water system connected to an auxiliary heat source where the hot water is then used to heat air as described earlier in the hot water-convection heater. It should be noticed that two pumps are required to operate this system which adds to operating cost.

Other configurations for space heating have been considered by eliminating the need for secondary heat exchangers. By using rocks with air as the heat transfer fluid, the heat exchanger is eliminated since the rocks act as heat exchanger and storage medium. The air charging the rocks is heated with a solar air heater and transfers the excess heat to the rock bed while using the heated air directly as needed during the day. This configuration also eliminates the use of the second pump as was discussed for Figure 1.5.
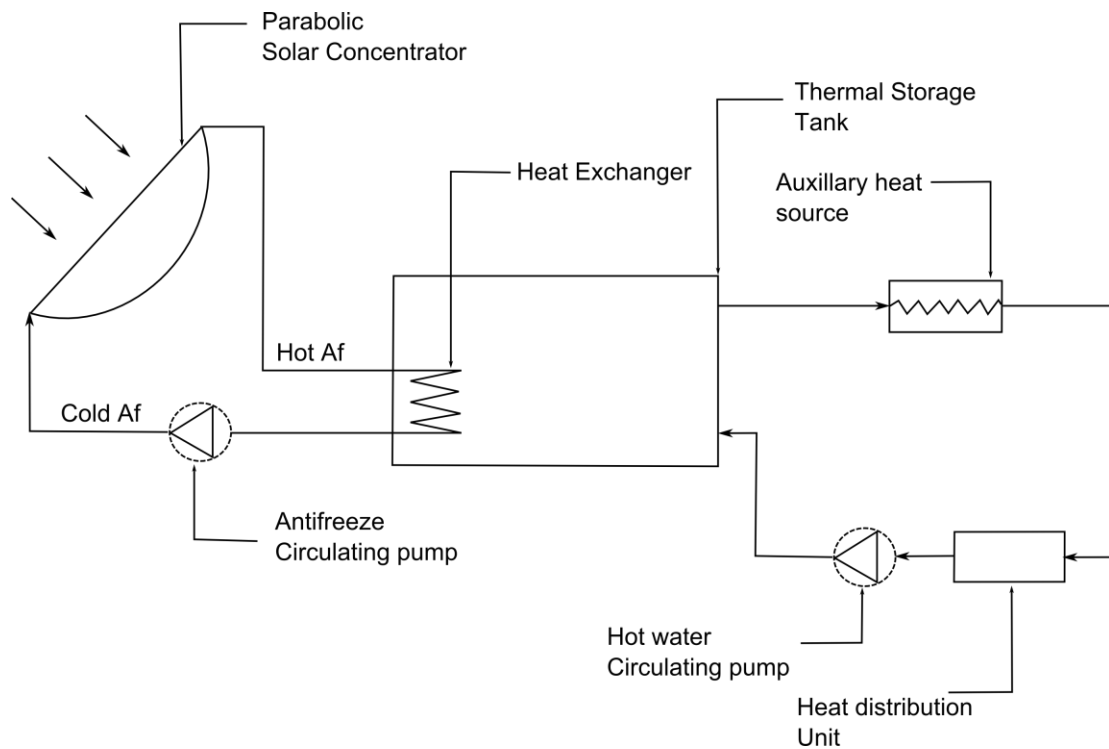
Figure 1.5: Schematic of a hot water convective solar heater (adapted from Fawaz et al. 2014)

1.3 HYDROSOL concept and operation

In this section, the proposed concept of the HYDROSOL is introduced and the basic operation modes that the system can be configured to are discussed.

1.3.1 Basic concept description

A typical HYDROSOL system is schematically shown in Figure 1.6. The proposed air temperature regulating assembly is an integrated process of energy collection and storage. It is also a multipurpose and sustainable renewable energy system, designed for space heating and/or cooling. Depending on the operating and control requirements, it consists of a bed filled with crushed rock of any desired length and width, a rear thermally insulated supporting wall and steel grating (optional), some axial fans able to reverse the direction of the air mass flow connected to a variable speed drive, a transparent roof at the top, a water spray system, just beneath the transparent roof or located in the rock bed, and a retractable heat retaining mechanism. System control is achieved by means of a bypass duct, flow regulating dampers (A to F) connected to a controller as well as air mass flow control by adjusting fan(s) speed. The air space between the back wall and HYDROSOL wall are conceptual and should be designed according to the requirements of the application. This can include using dry-walls, ducts or insulated pipes.
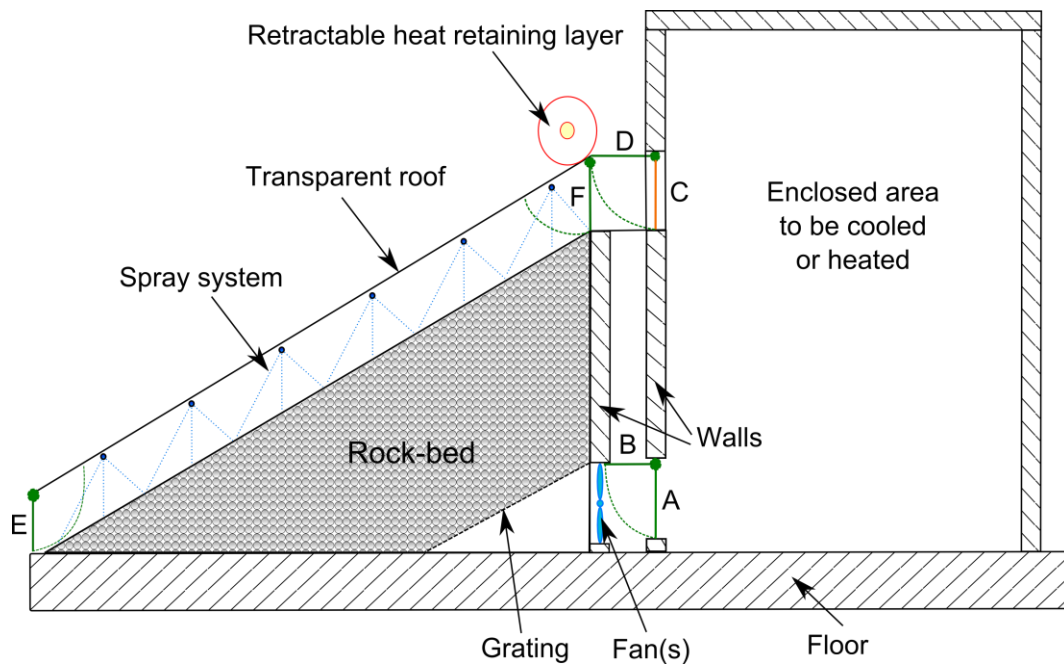
Figure 1.6: A typical HYDROSOL system

It is required that the crushed rocks are piled against the thermally insulated walls from the top and allowed to form at their natural angle of repose. The angle of the transparent roof and side walls of the system are the same as the known natural angle of repose of the selected crushed rocks. Typical rock diameters may range from 10 mm to 60 mm and should be fairly uniform for a specific bed. This system is installed so that the transparent roof at the top is facing the sun at noon, provided that sufficient space is available, and there are no obstructions to the incoming solar irradiation. At different positions in the rock bed, thermocouples must be installed, connected to a controller, to determine the amount of energy stored in the bed. The system can be configured to three basic modes of operation achieved by the air dampers and the retractable heat retaining cover i.e. solar heating, convective dry cooling and evaporative wet cooling.

In the embodiment of the proposed system as illustrated in Figure 1.6, the system comprises of an outer space found between the transparent roof and the top surface of the rocks. The optional inner space is formed when a grating is in position as shown between the lower extremity of the rocks and the fans. These two spaces are separated by the naturally formed rock bed in a manner that air can pass through the interstitial spaces between the rocks and allow heat to be transferred to or from the rocks. The enclosed area can be a warehouse, office suites, shopping centre, poultry farm broilers, residential house, green house and even a kiln for the drying of foods, wood or fuel.

The retractable heat retaining mechanism on top of the transparent roof is typically lowered during the night and on cloudy or rainy days, when operating as a heater, in order to minimize heat losses to the sky and atmosphere. During the

summer, when cooling is required the heat retaining mechanism is open during the night to allow night sky radiation from the rocks and in daytime this mechanism is closed so that no solar heat can enter the rock bed.

The system is integrated with a controller that may be programmed to control the entire assembly according to the inputs received either manually or from measurements and algorithms or schedules that reflect the possible setting of the assembly as shown in Figure 1.7. The variable speed drive (VSD); temperature measurements at various positions in the rock bed; ambient temperatures; outlet temperature available for the load; the retractable heat retaining mechanism; a water pump for supplying water to sprinklers; a water level measurement in a tank; pressure drop measurements to determine air mass flow rate; air regulating dampers A to F and a pyranometer are connected to the controller in order to control the system.
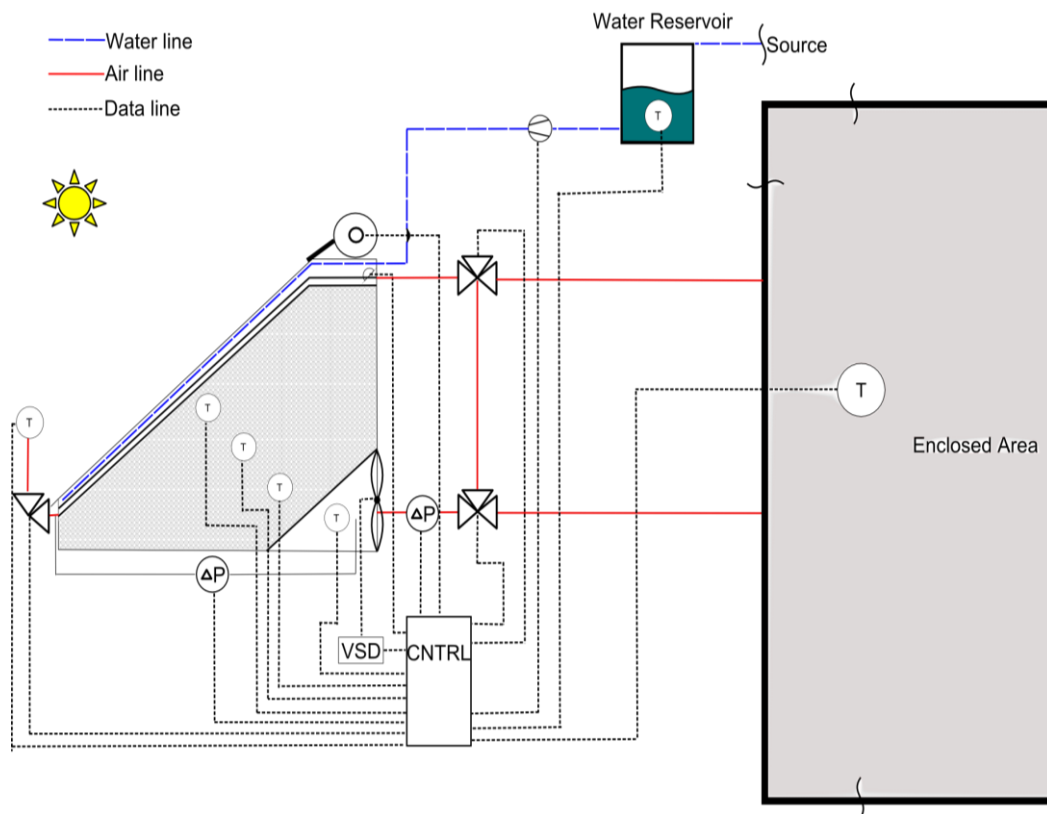
Figure 1.7: Control network diagram

During extreme summer temperatures, when convective cooling and storage are not sufficient, water can be sprayed into the air stream and on to the rocks to enhance further heat transfer and lower the temperatures even further for storage. The system as a heater and cooler will be discussed in the following sections and referred to as follows: positive/negative forward/backward charge/discharge mode

of operation. The positive indicates the system is operated as a heater with the negative indicating cooling mode of operation. Forward operation indicates induced draft where air is forced from the outer space through the packed bed to the inner space whereas negative indicates forced draft where air is forced from the inner space to the outer space through the rock bed. The heat storage can be used to rectify the mismatch between supply and demand of heat. Further improvements to the system, such as combining the system with a secondary solar air heater, may be implemented to meet the heating demands directly during the day while storing energy for the night, however these improvements are not in the scope of this thesis and focus will rather fall on the basic system as described above.

1.3.2 Heater

When the system operates as a heater e.g. in winter, solar heat is harnessed during the day and stored in the rock bed. Depending on the demand in the space to be heated the system will be prepared in a positive forward charge mode of operation (PFC) that can be used in five different ways as shown in Figure 1.8.

The retractable heat retaining layer (RHRL) at the top is open during the day and solar irradiation strikes the top layers of rock beneath the transparent roof. As the top layers heat up, either ambient air, re-circulated air or a mixture of the two passes through over the rocks in the heated layer and heats up. This warm air transfers the heat to the rest of the rocks deeper down in the bed. To get more useful energy from the system it should be charged at the maximum mass flow rate to keep top layer rocks at a lower temperature in order to minimize heat losses to the environment.

Figure 1.8 (a) shows a positive forward charge and discharge mode of operation during the day where dampers E, B and D are shut with C, F and A in the open position (mode 1). This allows air to be circulated from the outer space through the rock bed to the inner space into the enclosed area and back to the outer space where it is heated again. This closed loop mode is used to raise the air temperature in the system when no need for fresh air is required. If the enclosed space requires the system to provide it with fresh air, air damper E can be partially opened to mix ambient air with the re-circulated air. During the night, the retractable heat retaining layer (RHRL) is lowered to discharge the stored energy in the bed in a positive forward discharge (PFD) mode of operation. Thus, a PFC and PFD can be used simultaneously to meet the demand while preparing for the next day or night.

(a) PFC, used circulate

(b) PFC, unused circulate

(c) PFC, unused dump

(d) PFC, used dump

(e) PBD, used circulate
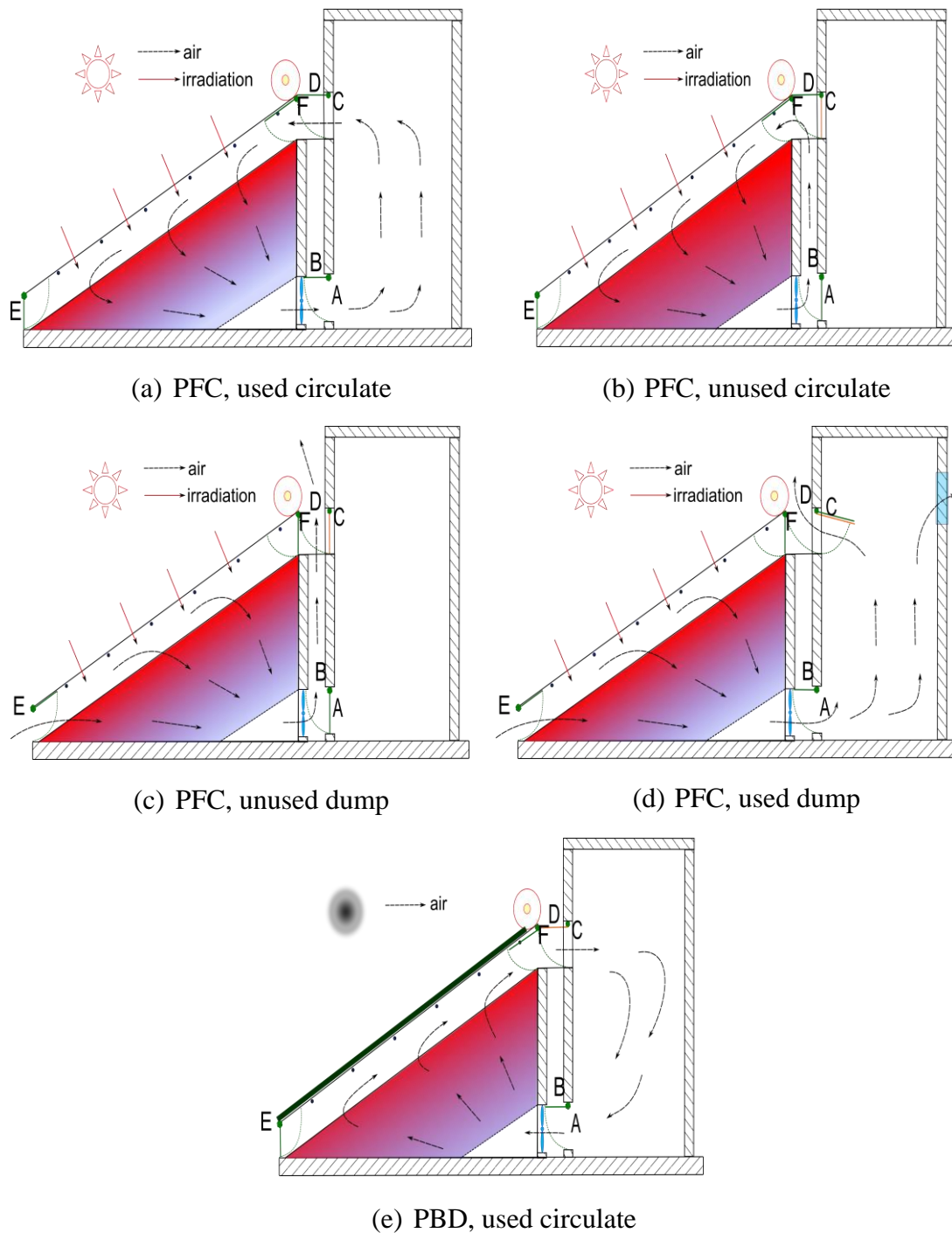
Figure 1.8: Positive forward charge/discharge modes of operation

The outlet air in the inner space during a PFC mode is not necessarily at a desired temperature to meet the requirements and would not always be ideal to circulate through the enclosed space, since undesired temperatures are rectified with the storage and would have to be dumped while preparing for a new cycle by moving the newly formed thermocline through the bed. This problem is easily overcome during the charging cycle by shutting dampers A and C and by doing so damper B

13

will automatically open while damper F remains open and all the others shut (mode 2). Figure 1.8 (b) shows this mode of operation where the outlet air is unwanted in the enclosed space or needs to reach higher temperatures before the heat can be harnessed from it. Air no longer moves through the enclosed space and is circulated through the thermally insulated walls at the back to the outer space where it can again heat up further as it moves over the top layer of rocks. This mode is known as a 100 % PFC and is usually done to increase the amount of energy stored in the rocks for a few days to extract even warmer air from it. Once the desired temperature profile in the bed is reached the heat can be extracted from it similarly to Figure 1.8 (a) in PFD mode of operation. This mode can also be used to shift the thermocline in the rock bed to the outlet of the system before dispatching it into the enclosed space. The thermocline can be moved to the middle of the bed to reduce radiation losses at the top and bottom, and switched off during the night when no heat is required. This heat can be dispatched the next day while charging the bed from the top again.

Depending on the thermocline and state of heat stored in the bed, the outlet air in the inner space for a forward operation can be slightly cooler than the ambient air temperature. Should this be the case, the outlet air is dumped to the atmosphere rather than circulating it back to the outer space. Slightly warmer ambient air is rather used as the inlet air to charge the rock bed to higher temperatures. This operation mode can be seen in Figure 1.8 (c) with dampers E, B and D open and the rest closed (mode 3). This mode is also used when the outlet temperature of the system is unwanted in the enclosed space while the system is being positively charged and the outlet air is rather dumped to the atmosphere.

The fourth PFC mode is shown in Figure 1.8 (d) with dampers E and A (C and D optionally) open and the rest remain closed (mode 4). This mode is used when the outlet air temperature (hot or cold) is desired during the charge cycle. Thus, a PFC and PFD mode is combined by charging the rock bed while discharging it. Outlet air is pumped into the space and leaves it typically through windows of a house or through duct systems with dampers C and D while ambient air is used at the inlet. An example for this mode of operation would be when constant outlet temperature is to be achieved during day and night when during the day cooling is required and during the night heating. This would result in an offset operation where the stored heat during the day is dispatched into the space at night time while negative charging, with cool ambient air, is happening at the top and vice versa during the day. Depending on the need of the space, a combination of the charge modes can be used to prepare the system in order to meet the demand of the space for the specified time.

Similarly for PFD modes of operation, modes 1, 3 and 4 can be configured by lowering or opening the RHRL as needed. Typically, during a PFD mode the RHRL would be open during times that solar heat can be harnessed and closed during the night as shown in Figure 1.8 (e). As mentioned earlier, during a PFC and PFD mode, a thermocline is formed at the inlet and moves through the bed

14

until the heat can be used in the enclosed area. This is usually not ideal since the system cannot always immediately meet the demand as the thermocline first has to be shifted through the rock bed. Instead, another mode of operation is the positive backward discharge mode (PBD) as shown in Figure 1.8 (e). This requires the fans to switch air flow direction and force the air from the inner space, through the rock bed to the outer space. As the sun goes under the thermocline would still be close to the outer space and heat can be immediately dispatched from the system. By configuring the air regulating dampers to mode 1, the heat can be used directly in the enclosed area while circulating the air from this space through the fan to the inner space. This mode is used during the night with the RHRL lowered since the configuration of this mode during day time with the RHRL open would result in an inefficient solar air heater while discharging the rock bed.

1.3.3 Convective dry-cooler

Consider Figure 1.8 again for convective dry- cooling operation. Cold ambient air is used to cool the rock bed during the night for cold storage. This cold storage is then extracted from the rock bed mainly during the day or as needed. This operation is similar to the heater operation that can be charged in a negative forward charge mode (NFC) using the damper configurations of modes 1- 4 as described in the heater operation. In a mode 3 configuration, the RHRL is open during the night to allow sky from the rocks through the transparent roof to the sky. During the day, the RHRL is lowered to block solar irradiation and the dampers can be configured to modes 1 or 4 to initiate a negative forward discharge (NFD) mode. During the day the cooler of the enclosed air space and ambient air temperature can be used as the system inlet. Similar to the positive charge and discharge operations, the outlet air can be dumped to the atmosphere, used before being dumped or re-circulated back to the bed.

Again, it is not always ideal to move the thermocline through the bed, and it requires more fan power, a negative backward discharge (NBD) mode might be more appropriate in some applications and thus by configuring system to mode 1, cool air can be dispatched from the outer space to the enclosed area. During the day the RHRL is lowered while opened for the night when enough energy is rejected from the rocks to make up the demand that cannot be met by ambient air itself. Rarely the case, but might be appropriate for some applications is the negative backward charge (NBC) where cool air from the space is used to cold-charge the rock bed while dumping outlet air in the outer space to the atmosphere. A combination of the negative charge and discharge modes is possible to prepare the system to meet the demand.

As the case might be that ambient air is not sufficient to cold charge the system to meet the demand for the day time, an auxiliary system can be fitted to the outlet to supply the required energy or to charge the system during off peak times.

However, the HYDROSOL can still be configured to evaporative or wet cooling mode of operation.

1.3.4 Wet-cooler

Wet and/or evaporative cooling operations, typically during hot summer days and nights when dry- convective cooling is insufficient, is achieved similar to the dry cooling except that water is sprayed into the airstream and onto the rock bed to enhance the cooling by means of evaporative cooling. The water system sprays just enough water to allow air to become saturated as it moves through the rock bed. The cold saturated air is used in a NFC mode configured modes 1-4 of operation to remove energy in the rocks. Depending on the application and requirements of the space, the cool humid air can be used directly which might be the case for some agricultural industries.

The wet cooling operation, usually for thermal comfort or applications where high humidity ratios are not ideal, is initiated by dumping the humid air at the outlet to the atmosphere in a mode 3 configuration. Once sufficient energy is stored, no more water is sprayed onto the rocks and ambient air is forced over the wetted rocks allowing it to dry while still dumping the humid air. As the rocks become dry, a normal convective NFD or NBD mode of operation can be initiated.

1.4 Objectives and scope

The performance evaluation of a sustainable renewable air temperature regulating assembly, the HYDROSOL, is proposed in this thesis. Different control strategies and applications are discussed and numerical results compared to experimental data.

Performance evaluation of the system is based on pressure drop over the packed bed and its thermal behaviour. The Schumann (1922) model is the basis for deriving governing equations describing temperature profiles through the bed. The model is improved by the assumptions made by Hughes et al. (1976) to improve simulation time. The heat transfer correlation of Wakao et al. (1978) is used in the models while making use of the analogy between heat and mass transfer to find the mass transfer coefficients.

The power required by the fan is determined by the correlations for pressure drop of the specific rock type used in the experiments proposed by Allen et al. (2013) for different orientations. The objectives of this research are therefore to:

    a. Design and manufacture a HYDROSOL system to conduct solar heating and convective dry cooling experiments.
    b. Perform wind tunnel experiments to validate heat transfer and pressure drop correlations used.
    c. Develop numerical models to predict pressure drop and thermal behaviour of the system.

    d. Perform solar heating and rock bed storage experiments on the HYDROSOL to validate numerical model.

    e. Perform convective dry cooling and rock bed storage experiments on the HYDROSOL to validate numerical model.

    f. Specify a control philosophy for the system to meet required heating or cooling loads.

    g. Propose a suitable system design for implementation into broiler houses.

1.5   Thesis outline

Chapter 1: Introduction

An introduction to the proposed concept and a brief background regarding conventional heating and cooling systems, specifically focusing on broiler houses, as well as basic operation configurations of the proposed system are presented.

Chapter 2: Literature study

Literature regarding pressure drop and thermal behaviour of packed rock beds is presented. This includes assumptions and considerations of previous work building up to the numerical models developed.

Chapter 3: Theoretical considerations

Governing equations for predicting pressure drop and thermal performance are derived from first principles and presented in its simplest form for numerical implementation.

Chapter 4: Experimental evaluation of a HYDROSOL performance

This briefly discusses the experimental apparatus designed and built for performance evaluation. It considers the procedure and steps followed to obtain experimental data as well as the measurement techniques used.

Chapter 5: Results and discussion of results

In this chapter all the results from measurements and numerical simulations are compared and discussed. The effect that different parameters have on the pressure drop and thermal performance are considered and compared. A control algorithm can be found based on mass flow rate parametric studies. Also, a suitable design for implementation in broiler houses is proposed.

Chapter 6: Conclusions and recommendations

The main findings of this research are summarized and possible further work or modifications are presented.

2 Literature study

The HYDROSOL, as mentioned earlier, uses no fuel and less or no water in order to regulate and control air temperature in an enclosed environment. The main operating cost of the system is the power required by the fan(s) and spray water pumps, if required, to achieve the energy load specified by the user or some control algorithm. In order to calculate the fan power, it is essential to predict the pressure drop over the entire system. The storage of heat in packed beds of rocks, using air as the heat transfer medium, for charging and discharging, leads to a thermocline forming in the length of the air flow path through the bed. In order to regulate air temperature in the enclosed environment, the thermocline needs to be known, either from measurements or predictions, and can then be controlled by air regulating dampers or a variation in mass flow rate. This section, presents a review of pressure drop correlations for packed beds of irregularly shaped particles such as rocks along with analytical models, as well as heat transfer correlations found in literature. Further considerations for designing the system, site selection and availability of materials are discussed.

2.1 Pressure drop in packed rock beds

Probably one of the most used equations for predicting pressure drop over packed beds of particles is the well-known Ergun (1952) equation, as cited by Du Plessis and Woudberg (2008). This semi-empirical equation was formulated to predict pressure drop through packed beds and is based on an extensive set of experimental data that included particles of different sizes, shapes and orientations. Correlations discussed in this section can be found in Appendix A.

The original Ergun equation (Eq. A.1) is formulated as the sum of the Blake-Kozeny equation (left hand side) which is based on the assumption that the packed bed can be considered to be a bundle of straight capillary tubes placed in parallel with the direction of the flowing fluid (Carman, 1937) and the Burke-Plummer equation (right hand side) for the turbulent region. The full derivation of the Ergun equation can be found in Du Plessis and Woudberg (2008). It can be seen from the equation that at high flow speeds, the right hand side of the equation dominates and at low speeds it becomes negligible.

Singh et al. (2006) obtained experimental results for pressure drop over packed beds and introduced an empirical correlation taking into account the shape of the particle. For the experiments an air duct heated by an electric heater was used and the size of the duct was 3 m x 0.5 m x 0.0254 m. The duct was insulated leading into a storage tank of 0.6 m diameter and 1.25 m in length in which the particles were packed. Material elements such as T-joint masonry bricks, standard masonry bricks, concrete cubes and concrete spheres were tested. The measurements were compared to the predictions of the Ergun equation and it was found that the Ergun equation under predicts the pressure drop, especially in the low flow speed region.

18

The correlation proposed by Singh et al.(2006) predicted within 13 % accuracy of measured data for non-spherical particles.

Chandra and Willits (1981) also performed experiments to determine the pressure drop over rock beds and presented a correlation to predict it. They found that pressure drop is dependent on rock size, air flow rate and void fraction of the bed. The apparatus was a 0.31 m x 0.31 m x 1 m wooden chamber with polystyrene insulation. The rockbed samples were washed river gravel and crushed granite with the rock bed in the wooden chamber being 0.6 m long and the air flow rates were varied between 0.003-0.05 m^3/s. It is further concluded that leaving out the effect of porosity may lead to significant errors.

Shitzer and Levy (1983) investigated the transient thermal behaviour of a rock bed. The experiments were performed in a mild steel cylinder 1 m in diameter and 2.45 m high. The experiment was insulated with 50 mm polystyrene and filled with crushed quarry rocks (ranging from 18-45 mm). Results for pressure drop were compared to correlations proposed by Chandra and Willits (1981) and Ergun (1952) and were found that these correlations underpredict the measured data by factors of up to 4.

Nemec and Levec (2005) performed their pressure drop experiments using uniformily sized spherical and non spherical particles. The setup was a 0.041 m diameter stainless steel comlumn, 0.7 m high. They concluded that the Ergun constants should be determined empirically for each bed since the original constants in the Ergun equation systematically under predicts the pressure drop even for spherical particles and states that the improved Ergun constants as proposed by Macdonald et al. (1979) should be approximately 15 % higher for non spherical particles.

Allen et al. (2013) performed experiments to obtain pressure drop correlations for rock beds and compared the results to the Ergun equation and the model of Singh et al. (2006). These experiments included varying particle sizes, shapes, orientation and packing configurations relative to air flow. The test section was 0.17 m x 0.37 m x 0.5 m with polystyrene insulation on the inside of the walls. They presented the best fit method and found that the Ergun equation under-predicts up to 40 %. They further found that the method of Singh et al. (2006) under predicts the pressure drop by up to 8 % and that there are no general correlations for non-spherical particles that include all parameters and predict the pressure drop to any degree of accuracy. Also, the friction factor for crushed rock is strongly depended on packing direction relative to the air flow as it was found that crushed rock packed in co-current orientation relative to the air flow resulted in up to 80 % higher apparent friction factors than the same rock packed in a cross-flow orientation.

2.2   Thermal models in rock beds

This section presents the most relevant literature on thermal models in packed beds of rock obtained experimentally and numerically for low temperature operation. All the models and correlations can be found in Appendix A.

As mentioned by numerous researchers such as Pascal Coutier and Farber (1982), Furnas (1929) and Abdel-Salam et al. (1991), Schumann (1929) was the first to successfully present an analytical solution to a fluid flowing through porous mediums such as rock beds to describe temperature distribution in the bed. It considers air flowing through a packed bed of rocks having a constant cross sectional area. In the derivation of the governing equations, Schumann (1929) makes some simplifying assumptions in his cylindrical model such as; no thermal conductivity in axial direction, thermal and physical properties of solid is constant, no mass transfer occurs, no heat loss to the environment and infinite conductivity in the radial direction.

A further simplification to the Schumann (1929) model was introduced by Hughes et al. (1976) when solar air heating systems are considered. They found that the Schumann model becomes too time consuming and simplified the governing equations of Schumann (1929) by neglecting thermal capacitance of the fluid. They rearranged the equations into a number of transfer units (*NTU*) model which, as cited by Duffie and Beckmann (1991), to be "best suited for solar system simulation."

Jefferson (1972) proposes a modified *NTU* method, (*NTU$_c$*), that includes the effects of temperature gradients within particles which becomes significant, especially at large Biot numbers. They concluded that when comparing predictions to measured values, the *NTU* and *NTU$_c$* adequately describe the temperature profile of the solid particles at Biot numbers less than $Bi \leq 0.1$.

Some pioneering work on determining the heat transfer coefficients for air-blown rock bed systems have been done by Löff and Hawley (1948). They performed their experiments with rounded river gravel of uniform sizes ranging from 4.826 mm to 28.1 mm to experimentally determine heat transfer coefficients from Schumann's model. The inlet air was maintained at constant temperatures ranging from 37.8 °C to 121.5 °C and the volumetric flow rates between 0.00566 m^3/s and 0.0311 m^3/s. Heating elements were placed on the walls of the test section to reduce heat transfer to the walls and environment. They concluded that inlet air temperatures did not affect the volumetric heat transfer coefficient.

Chandra and Willits (1981) noted some problems when using the method of Löff and Hawley (1948) for cooling tests, since the electric elements were only used for the heating experiments. They performed similar tests with rounded river gravel and accounted for the wall capacity as mentioned by Furnas (1929) by performing the tests twice in succession and only consider the measurements of the second test and concluded that this method could be used for heating and

cooling unlike the method proposed by Löff and Hawley (1981). The test setup was as described in Section 2.1. They concluded that the heat transfer coefficient between the rock and the air is strongly dependent on particle size and the mass flow rate of the air, and that the effect of porosity was negligible while heat transfer was not sensitive to inlet air humidity variation. The mean deviation between experimental data and predicted values was found to be 3.4 %.

Pascal Coutier and Farber (1982) performed thermal experiments of air- rock bed systems. Different types of rocks with variable sizes were tested in an apparatus with storage unit of 0.57 m diameter and 0.84 m height. Flow rate ranged between $0.379 \text{ m}^3/\text{s}$ and $1.98 \text{ m}^3/\text{s}$. The Biot number was found to be less than $Bi < 0.1$ which means that temperature gradient within the rock particle is negligible. A least square method was used to obtain a curve fit. They mentioned that when dealing with solar heat storage, in solid particles, the Schumann model should not be used since the actual conditions are too restrictive for the model. Pascal Coutier and Farber (1982) obtained numerical solutions for their governing equations and present empirical correlations for the heat transfer coefficient (Barton, 2013).

Wakao et al. (1978) propose a correlation for the heat transfer coefficient that is corrected for axial fluid thermal dispersion. They based their correlation on measurements found in literature for solid particles (spheres, cubes and cylinders).

Jalalzadeh-Azar et al. (1996) investigated heat transfer in high temperature energy storage in packed beds. They used zirconium oxide pellets having diameters of 18 mm with air as the heat transfer medium heated by a 350 kW gas-fired burner. The inlet air was varied from ambient temperature to 1100 °C. They concluded that thermal radiation between particles and air do not play an important role and is insignificant for temperatures below 900 °C and further concluded that the heat transfer correlation proposed by Wakao et al. (1978) is adequate for temperatures up to 960 °C.

Waked (1986) investigated solar energy storage and discusses the advantages of sensible heat storage in rocks. They heated rocks with different sizes (0.025 m-0.05 m) and varying air volumetric flow rates ($0.047 \text{ m}^3/\text{s}$, $0.07 \text{ m}^3/\text{s}$, 0.094 m^3/s and $0.142 \text{ m}^3/\text{s}$) in a well-insulated wooden box (0.61 m x 0.61 m x 0.61 m). They noted that more than 60 % of the energy stored in the rock bed can be extracted at temperatures very close to the maximum stored temperature.

Martin (2005) proposes a correlation based on the Generalized Lévèque Equation for heat and mass transfer coefficients that are linked to frictional pressure drop over the bed. It makes use of the Hagen number that is determined from the Ergun equation and based their correlations on measurements from spheres and cubes. It was found that cubes resulted in much lower Nusselt numbers than spheres.

Allen et al. (2013) performed low temperature air-rock heat transfer experiments with crushed rocks ranging from 13 mm to 26 mm in diameter in a 0.26 m x 0.26 m x 0.3 m plywood foam insulation test apparatus. He employed the

effectiveness-*NTU* method proposed by Hughes et al. (1976) and used the correlations of Wakao et al. (1978) and Martin (2005). The tests ranged from Biot numbers of $Bi = 0.01$ to $Bi = 0.2$ and were concluded that it is reasonable to use rock beds of Biot number up to 0.2 without taking the thermal conductivity of rocks into account. Also, the correlations of Wakao et al. (1978) and Martin (2005) predicted the measured temperatures very closely for all rocks tested regardless of the packing configuration.

2.3   Rock selection and rock bed considerations

Selecting rock type for the system is primarily based on initial cost including transportation to the site of implementation. According to Kalogirou (2009), typical rock sizes for pebble bed range from 35 mm to 100 mm in diameter, depending on the pressure drop over the bed, the geometry of the system and the air mass flow rate.

Eckhof and Okos (1978) state that larger rocks are better for storage purposes and that it requires less fan power than smaller rocks since they have lower pressure drops but at the cost of less heat transfer surface. They recommend selecting rocks between 25.4 mm and 76.2 mm in diameter since smaller rocks would increase pressure drop too much and larger rocks would have insufficient heat transfer surfaces. The rock should be uniform in size and rocks that tend to flake, such as limestone, should not be considered.

Abdel-Wahed et al. (1979) suggest that permeability vs bed height to be chosen so that the fan energy does not exceed two percent of the energy stored. Pascal Coutier and Farber (1982) present methods to select rock sizes, mass flow rate, bed length and bed face area. They found the fan power to be acceptable between 1 to 10 % of total energy stored in the bed.

King and Burns (1981) recommend velocities over the bed for low temperature storage systems between 0.08 m/s to 0.13 m/s and that the rocks should be washed before being used as storage for air-rock systems to avoid dust in the airstream. They further recommend using rock particle sizes between 20 mm and 30 mm in diameter that is fairly uniform in size and that a short distance from inlet to outlet is required with a large cross-sectional area.

Much work has been done on rock types, properties, availability and their suitability in South Africa by Allen et al. (2013). The main conclusions were that the most suitable rock for thermal storage at high temperatures (500 °C – 600 °C) is most likely to be igneous or metamorphic rock and some sedimentary rock that survived thermal cycling tests. Furthermore, foliated metamorphic rock such as gneiss and sedimentary rocks such as shale and limestone should not be used since they were found to fracture more easily and break into smaller particles, filling the voids in the bed, leading to an increase in pressure drop. However, for low temperature storage, some sedimentary rocks such as hornfels that do not

fracture as easily (because of its formation) as limestone and shale can be used as heat storage medium.

Since the main contributor to cost is the transport cost of rocks, site selection should be based on rock availability and levels of GHI specifically when the system is considered for mainly heating applications, such as the drying of goods. If the systems main application is considered to be cooling e.g. the inlet system to a gas turbine, selection should be based on rock- and water availability. When the system is intended for multipurpose use such as for buildings or broiler houses, a compromise of the above mentioned should be considered to select favourable positions for implementation of the system.

Figure 2.1 shows a map of South Africa with average GHI levels from 2004 to 2010. The active aggregate mines, obtained from the Council of Geoscience in South Africa, are listed in and shown on the GHI map. It should be noted that the mines shown are continuous production (CPR) aggregate mines and the intermediate product (IPR) mines, or mines that produce aggregate as a secondary commodity are not shown on the map but are also listed in Appendix K. An average cost as calculated for October 2014 was found to be R1.45/ton/km (only in the Western Cape).
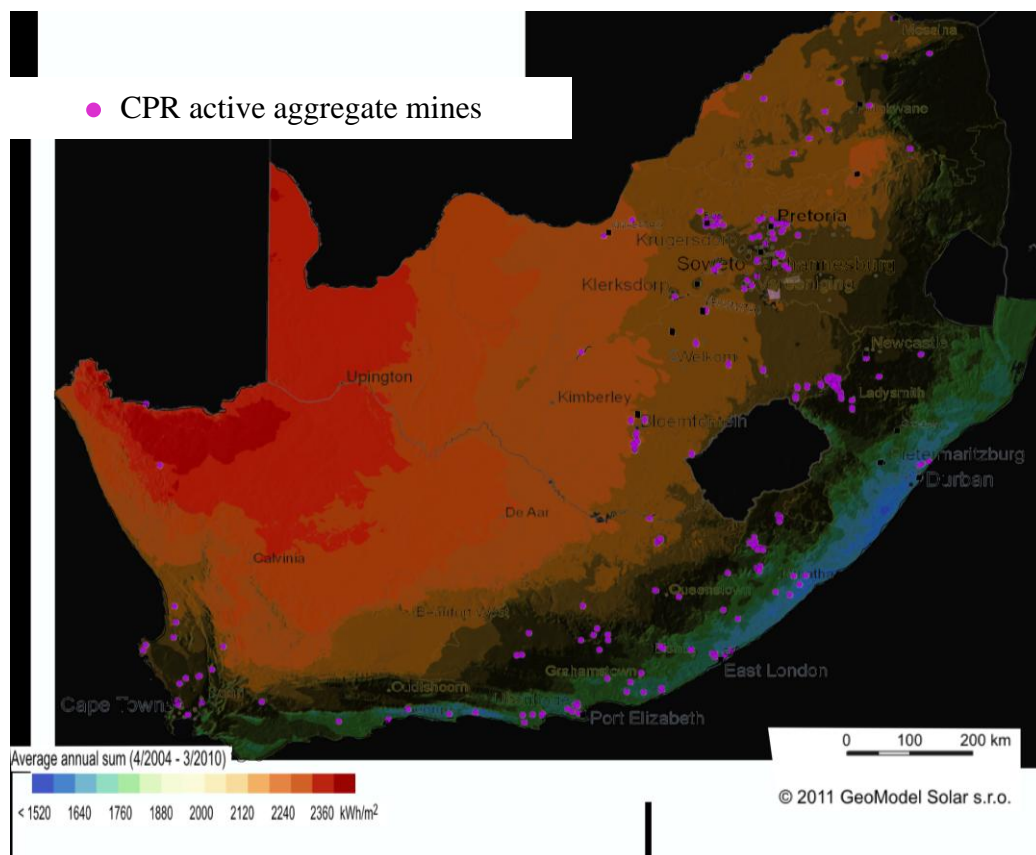
Figure 2.1:GHI and continuous production aggregate mines (modified from Council of Geoscience in South Africa, 2014)

23

As mentioned above, water- and rock availability along with diurnal temperature variation, determines site selection when cooling is the main application. Figure 2.3 shows an overlay map of South Africa with precipitation levels and active CPR mines. Areas with lower precipitation usually add cost to water usage and should not be considered for long term operation. However, if only air convective cooling is considered, selection should only be based on availability of aggregate mines and the distance from the identified site.

Best suited wet cooling sites that utilize water would be in parts of the Western Cape as well as areas south east of South Africa where precipitation levels are high. However, the system is intended to provide sufficient cooling with minimal (or no) water usage and can thus be installed where rocks are easy obtainable.

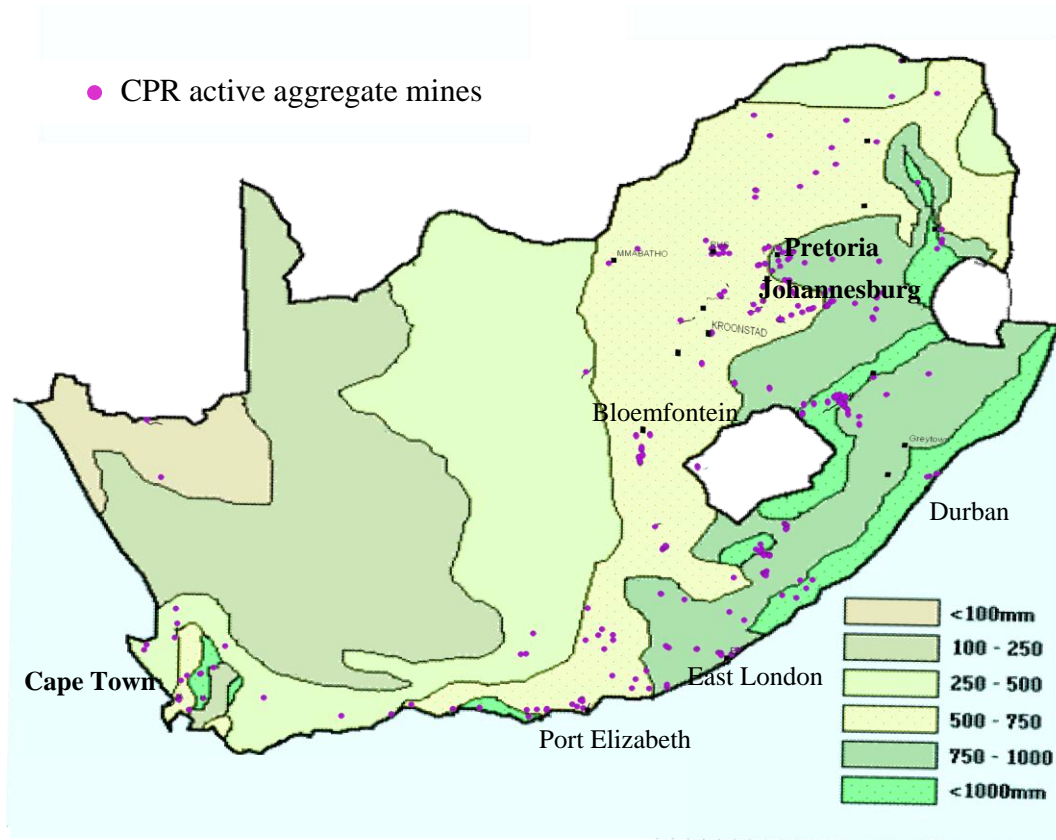**Figure 2.2:Precipitation and continuous production aggregate mines (modified from Council of Geoscience in South Africa, 2014)**

2.4 Design parameters considered

When considering a basic HYDROSOL setup it should be noted that the system is modelled as a solar air heater with the top layer of rocks being the absorber plate and a transparent cover plate at the top. As air moves over the absorber (top layer), in the outer space it heats up before penetrating into the rock bed. It is assumed that the walls are fully insulated and the only heat loss occurs at the top through the cover plate. Figure 2.3 is a depiction of a basic cross sectional area of the top rock layer of a HYDROSOL system during a heating cycle along with its appropriate thermal resistance diagram, when operating as an air heater. The surrounding temperature is considered to be ambient and the temperature of the cover plate varies only in its length.

According to Duffie and Beckmann (1991), the sky can be considered as a blackbody and that the temperature of the sky is at some equivalent sky temperature, T_s. According to Berdahl and Martin (1984) as cited by Duffie and Beckmann (1991), the effective sky temperature for clear skies can be obtained from;

$$T_{sky} = T_{surr}[0.711 + 0.0056T_{dp} + 0.000073T_{dp}^3 + 0.013\cos(15t)]^{1/4} \tag{2.1}$$

where the effective sky temperature, T_{sky}, and the surrounding outside temperature, T_{surr}, are in degrees Kelvin, time, t, is the hour from midnight and the dew-point temperature, T_{dp}, is in degrees Celsius. Garg and Prakash (1984) as cited by Duffie and Beckman (1991) make use of the following correlation in terms of outside temperature to calculate the effective sky radiation.

$$T_{sky} = 0.0552T_{surr}^{1.5} \tag{2.2}$$

Duffie and Beckman (1991) state that clouds will increase the effective sky temperature during the day and further concluded that sky temperature has little effect on collector performance but becomes critical when passive cooling is considered.

Incident solar irradiation, I_i, strikes the transparent cover at the top. Some of this heat, ρ_c, is reflected back to the atmosphere whereas another fraction, α_c, is absorbed by the cover and the remainder is transmitted, τ, to the surface of the rocks, heating them up. It is further assumed that the portion of the transmitted energy reflected from the rock surface is small that it can be neglected, thus assuming all of the energy to be absorbed by the rocks.

At the rock surface, heat is transferred to or from the air stream in the open channel by convection, $\dot{Q}_{c,R-am}$. Similarly at the surface of the cover plate exposed to the flowing air in the channel, heat is transferred by means of convection, $\dot{Q}_{c,cp-am}$, to or from the cover plate. Heat is also transferred between

the rocks and the cover plate by means of radiation, $\dot{Q}_{r,R-cp}$. Some of this heat is recovered by the convection heat transfer from the cover plate to the air stream.
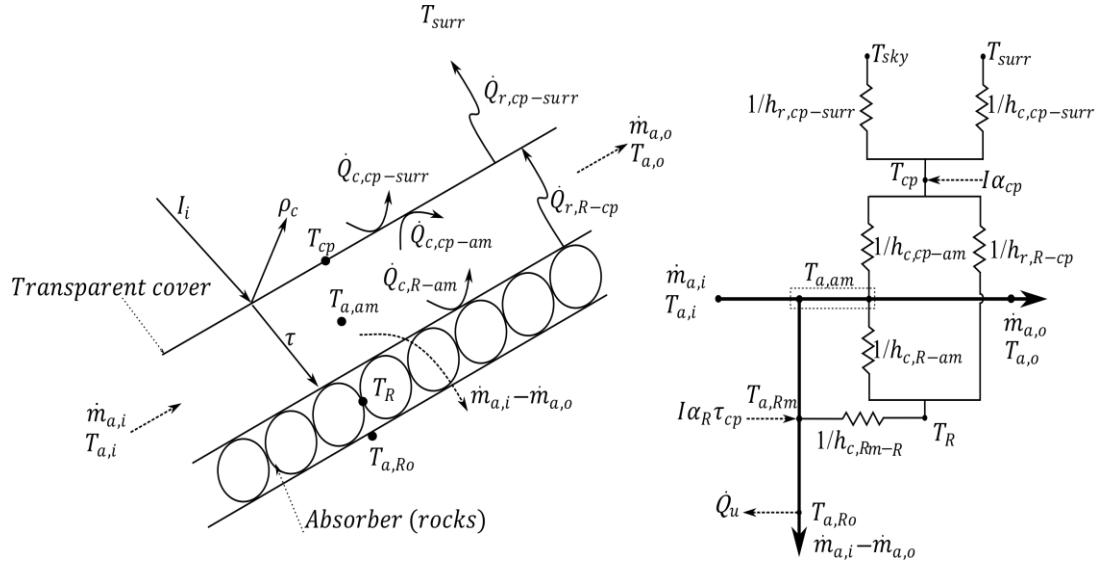
Figure 2.3: Schematic of HYDROSOL as solar air heater with thermal resistance diagram

At the top of the cover plate, heat is transferred to or from the surroundings by radiation, $\dot{Q}_{r,cp-surr}$, and convection, $\dot{Q}_{c,cp-surr}$. As air, in the open channel, moves through the rocks, heat is transferred between the rocks and air by convection, $\dot{Q}_{c,R-aRm}$, only. The useful energy, $\dot{Q}_u$, available for the system is the energy transferred to the air as it leaves the heated top layer(s) of rocks.

The convective heat transfer coefficient for the upper surface of the cover plate can be found by the correlation proposed by Mc. Adams, (1954);

$$h_{c,cp-surr} = 5.7 + 3.8u_w \tag{2.3}$$

where u_w is the velocity of wind flowing over the plate. The radiation heat transfer coefficient between two surfaces can be obtained from the definition as found in Duffie and Beckman (1991);

$$h_{r,R-cp} = \frac{\sigma(T_R^2 - T_{cp}^2)(T_R - T_{cp})}{\dfrac{1}{\varepsilon_R} + \dfrac{1}{\varepsilon_{cp}} - 1} \tag{2.4}$$

where ε_R and ε_{cp} are the emissivity of the rocks and cover plate respectively. Since the system is modelled as a solar air heater with the absorber storing energy, it is necessary to define a heat transfer coefficient for fluid flowing between two surfaces. Heaton et al. (1964) present a correlation for the convection heat transfer coefficient of forced convection between parallel plates as;

26

$$h_{c,cp-am} = h_{c,R-am} = \frac{k_a}{L}\left[5.4 + \frac{0.00190(Re_L Pr_L D_e/L)^{1.71}}{1 + 0.00563(Re_L Pr_L D_e/L)^{1.17}}\right] \quad (2.5)$$

where L is the length of the heat transfer surface and D_e the effective diameter (hydraulic diameter) of the channel. The Reynolds number for the flow can be obtained from;

$$Re_L = \frac{\rho_a u_a D_e}{\mu_a} \qquad (2.6)$$

where the velocity, u_a, is the superficial velocity at the inlet of a segment considered and $Pr_L = \mu_a c_{p,a}/k_a$. An important parameter for heat transfer in packed beds is the Nusselt number that is effectively a ratio of the convective heat transfer to the molecular thermal conductance. The Nusselt number for flow through rock bed voids can be written as;

$$Nu = \frac{h_c D_v}{k_a} \qquad (2.7)$$

with D_v being the volume equivalent rock particle diameter. Since it is time consuming and by no means practical to measure rock particle surface areas, a volume-equivalent particle diameter can be found by measuring the displacement of water with the addition of rocks. Assuming the rock particles to be modelled as spheres, the definition can be expressed as;

$$D_v = \left[\frac{6}{\pi}\left(\frac{1}{n}\sum_{i=1}^{n} V_{pi}\right)\right]^{1/3} \qquad (2.8)$$

where n denotes the number of added rocks and V_{pi} the displacement volume of water. A lumped capacitance model (applicable if $Bi \leq 0.1$) can be used so that the temperature gradient within the rock particles is negligible. Allen et al. (2013) however found acceptable values up to a Biot number of $Bi \leq 0.2$. The definition of the Biot number can be expressed in terms of a particle size and convective heat transfer coefficient as;

$$Bi = \frac{h_c D_v}{2k_R} \leq 0.2 \qquad (2.9)$$

The convective heat transfer coefficient for flow through rock beds can be obtained from the correlation of Wakao et al. (1978) which is based on measurements from spheres, cubes and cylinders and found in literature to describe packed rocks in thermal analysis fairly accurate;

$$h_{c,R-aRm} = \frac{k_a}{D_v}\left(2 + 1.1 Re_{pv}^{0.6} Pr^{\frac{1}{3}}\right) \qquad (2.10)$$

which is valid for $15 < Re_{pv} < 8500$. The volume equivalent particle Reynolds number Re_{pv} can thus be expressed in terms of the volume-equivalent diameter as;

$$Re_{pv} = \frac{\rho_a u_a D_v}{\mu_a} \qquad (2.11)$$

With ρ_a and μ_a being the density and viscosity of air respectively. The superficial velocity, u_a, is the hypothetical velocity of air as if it is the only thing present in a cross sectional area and not the increased velocity between the pores of the rock. The total rock surface available for heat transfer, a_{Ri}, can be found, as a surface area per unit volume, by the following equation from Nield and Bejan (2006);

$$a_{Ri} = \frac{6(1 - \varepsilon)}{D_v} \qquad (2.12)$$

where ε is the void fraction of the rock bed. Thus, by fixing the Biot number to $Bi = 0.2$ at the position in the bed with highest air velocity ensures the lumped capacitance model to be applicable at any position in the rock bed. Since the area reduces moving through the rock bed to the inner space in HYDROSOL, the air velocity through the rock bed would be at its highest at the inner effective radius. By substituting Eq. (2.9) into Eq. (2.10) and setting this equal to Eq. (2.11), the maximum velocity for applicability of lumped capacitance model can be calculated as;

$$Re_{pv} = \frac{\rho_a u_{max} D_v}{\mu_a} = \left(\frac{2Bi\, k_R/k_a - 2}{1.1 Pr^{1/3}} \right)^{1/0.6} \qquad (2.13)$$

The maximum mass flow rate of air through the bed can be found from;

$$\dot{m}_{max} = \rho_a A_{R,i} u_{max} \qquad (2.14)$$

where $A_{R,i}$ is the frontal area at the inner radius. An initial velocity profile can be found for any position in the bed for the maximum mass flow rate. The useful energy into the rock bed can thus be found for each time step by using the mass flow rate resulting from the choice of the Biot number as;

$$\delta Q_u = \dot{m}_{max} c_{p,a}(T_{am} - T_{a,Ro}) \qquad (2.15)$$

An energy collecting efficiency for heating can now be defined as the ratio of the amount of useful energy available to the system to the amount of radiation incident on the system;

$$\eta_{col} = \frac{\int Q_u\, dt}{\int I_i A\, dt} \qquad (2.16)$$

The length and effective outer radius is determined so that the maximum fixed Biot number on the inner radius does not exceed the maximum of 0.2.

The pressure drop over a rock bed, for the specific rocks in the HYDROSOL experiment, is predicted by correlations proposed by Allen et al. (2013) for a counter- current packing and a cross current packing respectively as a frictional force experienced by the flowing air;

$$f_v = \frac{\Delta p}{L(\rho u_s^2/2)} \frac{\varepsilon^3}{(1-\varepsilon)} D_v \approx 76.47 \left(\frac{1-\varepsilon}{Re_{pv}}\right)^{0.343} \tag{2.17}$$

valid for $0.38 < \varepsilon < 0.45$ and $0.009\ \text{m} < D_v < 0.045\ \text{m}$ and $50 < Re_{pv} < 400$ where D_v is determined from Eq. (2.10) and Re_{pv} from Eq.(2.16). L is the distance air has to move through the rock bed.

$$f_v = \frac{\Delta p}{L(\rho u_s^2/2)} \frac{\varepsilon^3}{(1-\varepsilon)} D_v \approx 80.94 \left(\frac{1-\varepsilon}{Re_{pv}}\right)^{0.41} \tag{2.18}$$

valid for $0.38 < \varepsilon < 0.45$ and $0.009\ \text{m} < D_v < 0.029\ \text{m}$ and $50 < Re_{pv} < 400$.

The operating cost of the system is mainly contributed to fan power required. By using obtained pressure drop correlations for the specific rock bed, the fan power for a known pressure drop can be determined from the fan hydraulic power equation as presented by Ramadan et al. (2007);

$$P_p = \frac{\Delta p \dot{m}_a}{\rho_a} \tag{2.19}$$

In order to find the pressure drop of the entire system, all the bends, elbows dampers, etc., should be included in the calculations. By further including the efficiencies of the motor and fan, the total fan power may be determined from,

$$P_{p,tot} = P_p / \eta_{motor} \eta_{fan} \tag{2.20}$$

For cooling, when water is sprayed onto the rock bed to enhance the cooling capacity of the system, it is assumed that the water film is infinitely small on the rock surface so that it can be modelled as a large stationary water drop having rock properties. By making this assumption, the water present in the system will not affect the pressure drop over the packed bed. As water is sprayed from the top of the transparent cover, some of the mass is transferred to the air stream before moving through the wetted rocks. Only enough water is sprayed on the rocks so that no circulation of water is required and evaporates before leaving the bed.

An analogy between mass and heat transfer is used in order to find the mass transfer coefficients by replacing the Nusselt ,Nu, and Prandtl, Pr, numbers with Sherwood, Sh, and Schmidt, Sc, numbers respectively. The correlation of Wakao et al. (1978) can then be written as;

$$h_{d,R-aRm} = \frac{D_{Fuller}}{D_v}\left(2 + 1.1Re_{pv}^{0.6}Sc^{\frac{1}{3}}\right) \qquad (2.21)$$

where D_{Fuller} is the semi-empirical correlation presented by Fuller et al. (1966) for mass diffusivity;

$$D_{Fuller} = \frac{(1/M_a + 1/M_v)^{0.5}T_a^{1.75}}{\sqrt{2}(\sum\Delta_{va}^{0.333} + \sum\Delta_{vb}^{0.333})^2\, p_{atm}} \qquad (2.22)$$

where $M_a = 28.958$, $M_v = 18.013$, $\sum\Delta_{va} = 19.7$ and $\sum\Delta_{vb} = 13.1$ for air.

Similarly for the mass transfer from the top surface to the air passing the mass transfer coefficient can be found from;

$$h_{d,cp\leftrightarrow am} = \frac{D_{Fuller}}{L}\left[5.4 + \frac{0.00190(Re_L Sc_L D_e/L)^{1.71}}{1 + 0.00563(Re_L Sc_L D_e/L)^{1.17}}\right] \qquad (2.23)$$

The Schmidt number, Sc, can be found from;

$$Sc = \frac{\mu_{av}}{\rho_{av}D_{Fuller}} \qquad (2.24)$$

The Sherwood number, Sh, is found from;

$$Sh = \frac{h_d D_v}{D_{Fuller}} \qquad (2.25)$$

The Lewis factor, $Le_f = Sc/Pr$, is defined as a direct relationship between the convective heat transfer coefficient and the mass transfer coefficient and is equal to $Le_f \approx 1$ as assumed by Merkel (1925) for this analysis.

All properties of air, air-vapour and water is found using correlations given in Kröger (2004).

2.5 Exploiting solar energy

Solar energy is our largest free source of energy available. To harvest this energy to a maximum during the winter, it is crucial to know the angles of the sun to orientate the system for maximum collecting efficiency. The orientation and tilt angle are fixed at the natural angle of repose for a typical HYDROSOL system so it is important to know the exact position of the earth relative to the sun for different seasons and how the angle affects the amount of solar heat that can be harvested during the day. Since the natural geometries, such as mountains or building surrounding a system, block solar radiation, the angles can be used to determine the exact time the system can fully harvest solar energy. Duffie and Beckmann (1991) describe the relationships between orientation of any plane relative to the earth and the incoming solar radiation with the definitions of the following angles:

ϕ	Latitude, the angle between the equator and position on the earth's surface, south negative $-90° \leq \phi \leq 90°$
θ_i	Incidence angle, the angle between the beam radiation on a surface to the normal of that surface
θ_z	Zenith angle, the angle between a vertical line from the horizontal and a line to the sun
δ	Declination angle, the angular position of the sun at solar noon with respect to the plane of the equator, south negative $-23.45° \leq \delta \leq 23.45°$
β	Slope angle, the angle between the surface and the horizontal, $0° \leq \beta \leq 180°$
γ	Surface azimuth angle, the deviation of projection on a horizontal plane of the normal to the surface from the local meridian, zero due south, east negative, $-180° \leq \gamma \leq 180°$
ω	Hour angle, east or west angular displacement of the sun to the local meridian due to rotation
α_s	Solar altitude angle, the angle between the line to the sun and the horizontal
γ_s	Solar azimuth angle, the angle of the projected beam radiation to the horizontal to the south axis, east of south projection is negative
Ψ	Longitude, the angle between the prime meridian and position on the earth's surface, west negative $-90° \leq \phi \leq 90°$
Ψ_{std}	Longitude of standard time zone meridian, west negative $-90° \leq \phi \leq 90°$

Figure 2.4 illustrates the angles as defined above with the point, *P*, shown as a tilted surface facing exactly north on a horizontal surface.

It should be noted that the South Pole at the top is to illustrate a position on the surface of the earth in the southern hemisphere. By calculating these angles as follows, the time of day that an obstruction causes shade on a system can be determined.

The incidence angle can be found in terms of the hour angle, azimuth angle, declination angle and latitude angle as found from Power from the Sun (s.a) given by;

$$\theta_i = \cos^{-1}(\sin\delta \ \sin\phi \ \cos\beta - \sin\delta \ \cos\phi \ \sin\beta \ \cos\gamma$$
$$+ \cos\delta \ \cos\phi \ \cos\beta \ \cos\omega$$
$$+ \cos\delta \ \sin\phi \ \sin\beta \ \cos\gamma \ \cos\omega$$
$$+ \cos\delta \ \sin\beta \ \sin\gamma \ \sin\omega) \tag{2.26}$$
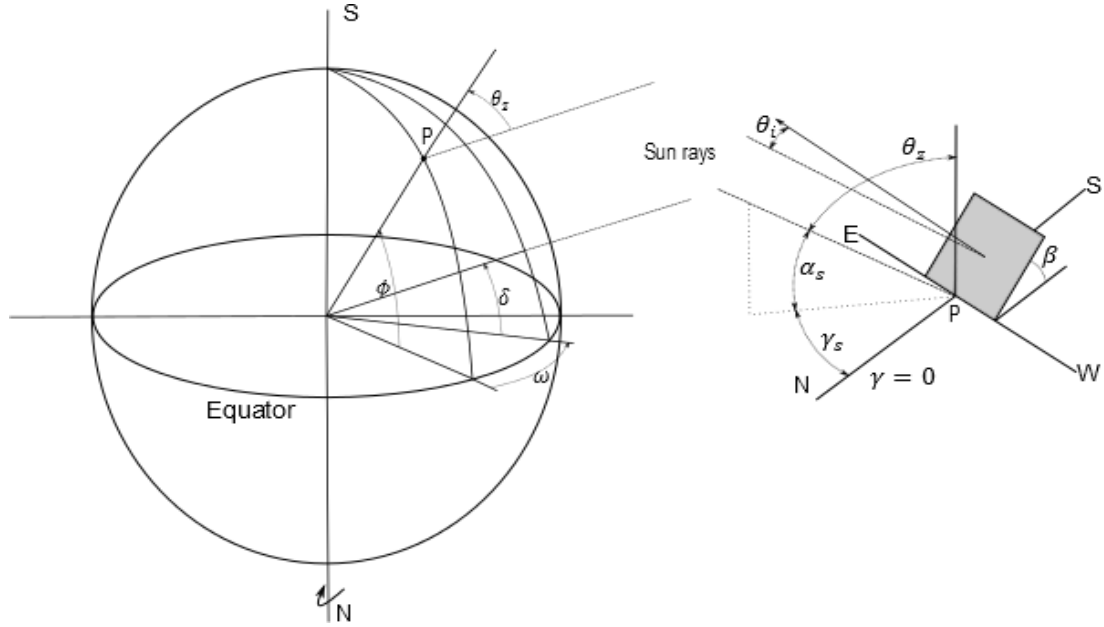
(a) Position of point on Earth's surface   (b) Solar angles tilted surface

Figure 2.4: Solar angles on a point of the earth's surface

The declination angle can be obtained from Eq.(2.27) and is accurate to within 1 degree which is sufficient for non-tracking systems (Power from the Sun, s.a);

$$\delta = \sin^{-1}(0.39795 \cos[0.98563(n - 173)]) \tag{2.27}$$

where n is the number of the day in the year with 1$^{\text{st}}$ of January being day 1. The solar azimuth angle can be calculated with;

$$\gamma_s = sign(\omega) \left| \cos^{-1}\left(\frac{\cos\theta_z \ \sin\phi - \sin\delta}{\sin\theta_z \ \cos\phi}\right) \right| \tag{2.28}$$

The $sign(\omega)$ indicates that only a positive or negative multiplication from the result of the hour angle is used. The hour angle requires a correction to be made between the local time and the solar time for the specific location and a correction for places where daylight savings are considered;

$$\omega = 15 \left(LCT - \Psi_{cor} - D + \frac{EOT}{60} - 12 \right) \tag{2.29}$$

32

with *LCT* being the Local Clock Time. *D* is a correction of 1 hour, included for places where daylight savings time is currently in effect (otherwise *D* = 0). The hour angle is 0° at solar noon for any location and the longitude correction can be found by;

$$\Psi_{cor} = \frac{\Psi - \Psi_{std}}{15} \tag{2.30}$$

and the Equation of time, *EOT*, can be obtained in minutes as;

$$EOT = 0.258\,cosx - 7.416\,sinx - 3.648\,cos2x \\ - 9.228sin\,2x \tag{2.31}$$

where the angle *x* is found by;

$$x = \frac{360(n-1)}{365.242} \tag{2.32}$$

The zenith angle can be obtained from;

$$\theta_z = \cos^{-1}(sin\delta sin\phi + cos\delta cos\phi cos\omega) \tag{2.33}$$

For illustrative purposes of solar angles consider a system, *HS*, harvesting solar irradiation during a year with a building 20 m high and 30 m in length having an east-west orientation as shown in Figure 2.5 causing a shade on *HS*. The system is located 20 m from the right hand corner of the building that is exactly due north.
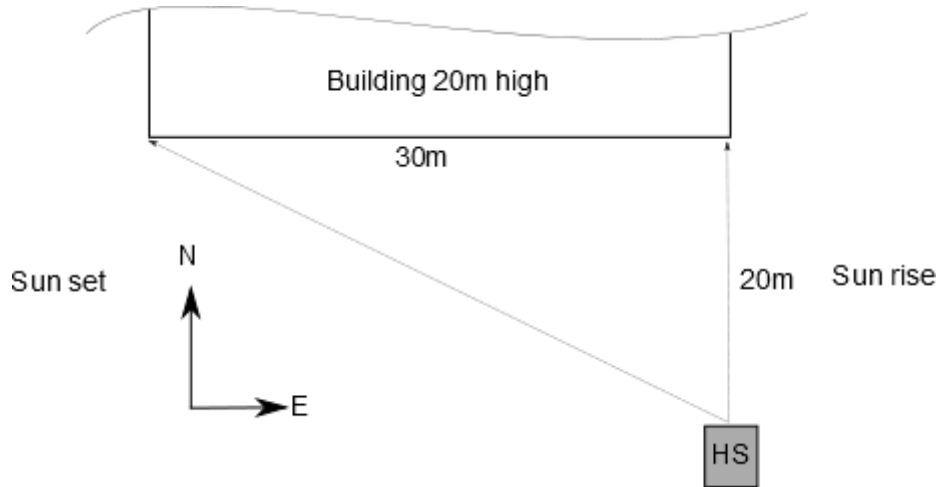
Figure 2.5: Building causing shade on the system

The right and left corners are considered to be the limit for blocking the sun and it is assumed that no other geometries have an effect in obstructing solar insolation. The latitude -, declination - and hour angle are fixed for a typical HYDROSOL system. The latitude for this example considered is $\phi = -33.92$ and the length of the system is not accounted for in this illustration and is considered as a point. The

shade that the building causes during a day for the whole year can be seen in Figure 2.6 as a solar plot of the solar azimuth angle and the solar altitude angle.
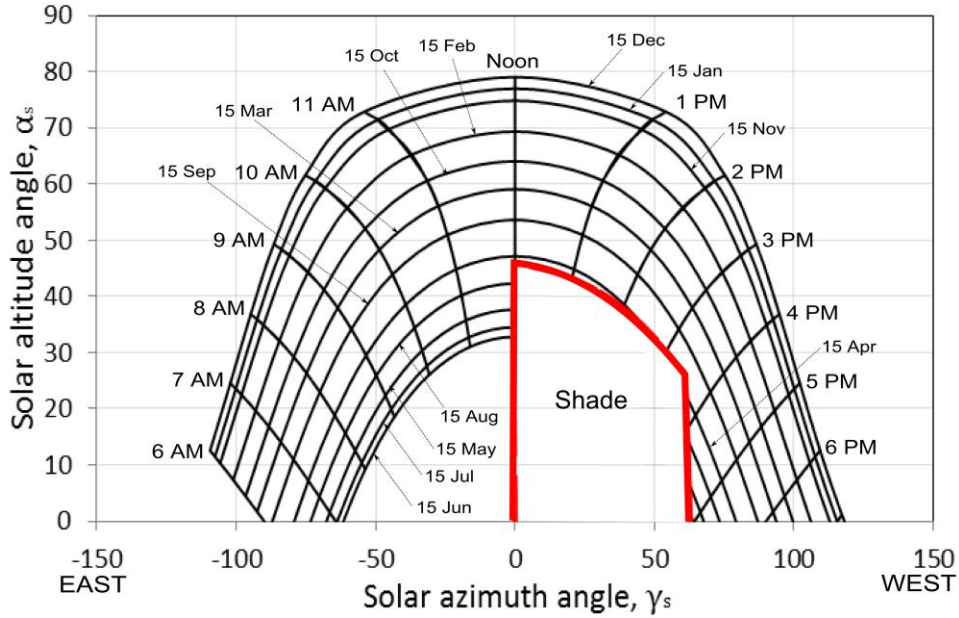
Figure 2.6: Shade caused by building

By calculating the zenith angle (or solar altitude angle) fromEq.(2.33), the declination angle from Eq.(2.27) and the hour angle from Eq.(2.29), the solar azimuth angle from Eq.(2.28) can be determined. Similarly if the dimensions of the obstruction(s) are known, an object azimuth and object altitude angle can determined for limiting geometries and presented on the same graph as shown above. The object altitude angle can be found by considering the height of the object above the collecting device, H_o, and distance from the collector, L_{p-o}, for each point considered on the building as;

$$\tan \alpha_{o,p} = \frac{H_o}{L_{p-o}} \tag{2.34}$$

where subscript *p* refers to the specific point considered. The object azimuth angle can found by considering the length of the building for the specific point at a distance from the position on the building that is in line with the solar noon and the *HS*, L_{12-p}, and the same inline distance to the collector, L_{12-c}.

$$\tan \gamma_{o,p} = \frac{L_{12-p}}{L_{12-c}} \tag{2.35}$$

34

It is clear from the result that during April to August a shadow will be present on the system from solar noon to about 5 PM during June. Thus, for harvesting solar energy during the winter, this site would not be ideal if maximum solar energy is required. However during the warmer months, no shade will be projected onto the system and should be selected based on the application requirements.

Solar radiation striking the earth can be described by beam and diffuse radiation. A pyranometer placed at the tilted angle of the system measures the global tilt irradiation, *GTI,* that penetrates the system. The *GTI* includes measurements of direct normal irradiation, *DNI*, and diffuse irradiation (scattered from clouds and/or reflected from other surfaces). This measurement is based on the sum of the *DNI* and the diffuse components adjusted for a tilted surface.

According to Duffie and Beckmann (1991) the amount of beam radiation on a tilted surface can be found by the ratio of tilted beam radiation normal to a horizontal surface;

$$R = \frac{I_{b,col}}{I_{b,n}} = \frac{I_b \cos(\theta_i)}{I_b \cos(\theta_z)} = \frac{\cos(\theta_i)}{\cos(\theta_z)} \tag{2.36}$$

The diffuse component on the tilted surface can be determined by the correlation proposed by Liu and Jordan (1963) where the total measured diffuse horizontal irradiation, *DHI*, is multiplied by the tilt angle (angle of repose) factor;

$$I_{d,col} = I_d \frac{1 + \cos(\beta)}{2} \tag{2.37}$$

The reflection component from different surfaces can be in found by;

$$I_{r,col} = \rho_{surf}(I_b + I_d) \frac{1 - \cos(\beta)}{2} \tag{2.38}$$

where ρ_{surf} is the reflectivity ratio of the surface. The total amount of insolation on the tilted surface can be found by summing $I_{b,col}$, $I_{d,col}$ and $I_{r,col}$.

2.6 Summary

The original Ergun equation as cited by Singh et al. (2006), Shitzer and Levy (1983) and Nemec and Levec (2005) systematically under-predicts pressure drop of air flow over irregularly shaped particles, especially rocks. Despite improved values proposed by numerous researchers i.e. Macdonald et al. (1979) and Nemec and Levec (2005), it is concluded by Nemec and Levec, (2005) that Ergun constants should be determined empirically for each bed.

Chandra and Willits (1981), Singh et al. (2006) and Allen et al. (2013) concluded that pressure drop is influenced by particle size, bed porosity and air mass flow rate while Allen et al. (2013) stated the importance of packing orientation. Thus, it is necessary to obtain empirical correlations for a particular set of rocks and

clearly state the packing method used. It is concluded that no general correlation exists for predicting pressure drop to any degree of accuracy without obtaining constants of existing correlations empirically.

As cited by researchers such as Pascal Coutier and Farber (1982), Furnas (1929) and Abdel-Salam et al. (1991), Schumann (1922) was the first to present a successful analytical model in describing heat transfer rate through packed bed with air as the heat transfer fluid. Hughes et al. (1976) took the Schumann model further by assuming that air thermal capacitance is negligible in the analysis and simplified it into a NTU model. Jefferson (1972) included thermal conductivity into the Schumann model and simplified it to the NTU_c model. It was found that the NTU_c and NTU model describes the temperature profile accurately when the Biot number is less than $Bi \leq 0.1$.

Pioneering work has been done by Löff and Hawley (1981), Chandra and Willits (1981) and Pascal Coutier and Farber (1982) in obtaining correlations for heat transfer coefficients from experiments conducted. Wakao et al. (1978) and Martin (2005) investigated data presented by other authors found in literature and proposed correlations for heat transfer from it. It is concluded that Wakao et al. (1978) and Martin (2005) correlations can be used with confidence to describe heat transfer rate for a packed bed.

A trade-off between thermal performance and fan power comes forth when selecting rock size for the system. Most agreement between rock sizes proposed for heat storage is between 30 mm and 60 mm in diameter. Larger rocks would result in lower fan power whereas smaller rocks would result in better thermal performance. Abdel-Wahed et al. (1979) and Pascal Coutier and Farber (1982) recommend selecting bed size so that fan energy is less than 10 % of the total energy stored.

Choosing the right type of rock is mainly decided on the basis of cost (mainly transportation cost) and the availability of it. As suggested by Allen et al. (2013), rocks that fracture easily such as limestone and shale should not be considered for thermal storage. Kings and Burns (1981) mentions that rocks should be washed when possible (when water availability and cost allows it) before being used as storage since it affects thermal performance of the bed.

Site selection for a system should primarily be based on rock availability, favourable solar irradiation levels, and, if required, water availability in the region as well as space availability, shade considerations and diurnal temperatures.

3 Theoretical considerations

This chapter describes the numerical model developed for calculating the performance of the HYDROSOL system and the design considerations in order to fully describe the system. The first part considers the governing equations derived from first principles in order to describe and predict performance. The governing equations are derived using a finite volume method for a position in the middle of the rock bed for 2-D flow of air and water in cylindrical coordinates. The equations are discretized and presented in its simplest form for numerical implementation. Numerical simulations are performed using Scilab open source software.

3.1 Derivation of the governing equations

Figure 3.1 is an illustration of finite volume consisting of rock and air inside the HYDROSOL system. The system is modelled as a quarter annulus with governing equations derived for cylindrical coordinates due to its simplicity (derivation of the system in Cartesian coordinates can be found in Appendix F). The derivation of the governing equations for thermal performance is similar to the equations derived by Schumann (1922) for axial flow through a cylinder packed with particles. The analogy between mass and convective heat transfer is used to find the mass transfer coefficients. For dry convective operation, a general node inside the annulus is considered and governing equations derived, as well as a top node harvesting solar heat and emitting heat to the transparent roof. Derivation for wet operation can be found in Appendix F.2. Some simplifying assumptions made in the derivation of the model are:

- Air flows only in the radial direction.
- Water flows vertically downward due to gravity.
- Rocks are modelled as spheres with a measured volume equivalent diameter.
- Biot number is small enough so that infinite resistance exists in a particle.
- Thermal capacitance of air can be neglected when compared to that of rock.
- No heat or mass transfer occurs in the theta direction.
- No inter particle conduction or radiation.
- Outlet air is saturated for wet-operating conditions.
- No losses to environment with transparent roof covered.
- Wall channelling effects of air is negligible.
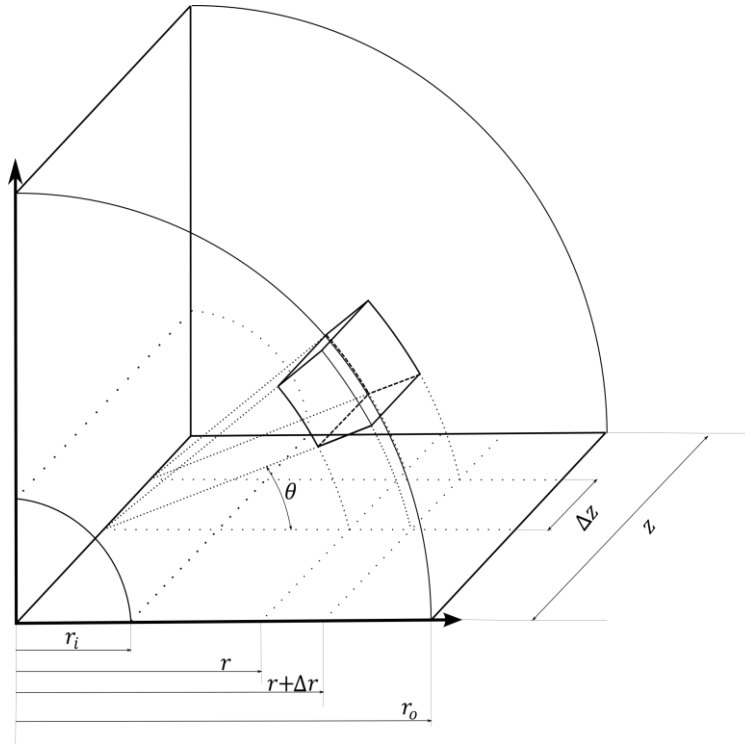
Figure 3.1: Quarter annulus with control volume

Air enters a control volume in the radial direction and transfers heat to the rocks inside the control volume. The θ angle is measured from the horizontal and the control volumes are divided into the annulus section between the inner and outer radius.

Performing a dry air mass balance over a selected control volume as depicted in Figure 3.2, consisting of rocks and air, in terms of a mass flux, $G = \rho u$, the following can be obtained;

$$-G_{a,r+\Delta r}\,(r + \Delta r)\Delta\theta\Delta z - \left(-G_{a,r}\,r\Delta\theta\Delta z\right) = 0 \tag{3.1}$$

Dividing this equation with the approximate volume, $-r\Delta\theta\Delta r\Delta z$, yields;

$$\frac{G_{a,r+\Delta r}}{\Delta r} + \frac{G_{a,r+\Delta r}}{r} - \frac{G_{a,r}}{\Delta r} = 0 \tag{3.2}$$

It can be shown that dividing with the exact volume a Δr^2 term is present and by assuming that this term is negligibly small the volume simplifies to the approximate volume.

Take the $\lim_{\Delta r,\Delta\theta\to 0}$ of Eq. (3.2) to find the differential equation for the mass flux of air;

38

$$\frac{dG_{a,r}}{dr} + \frac{G_{a,r}}{r} = 0 \tag{3.3}$$
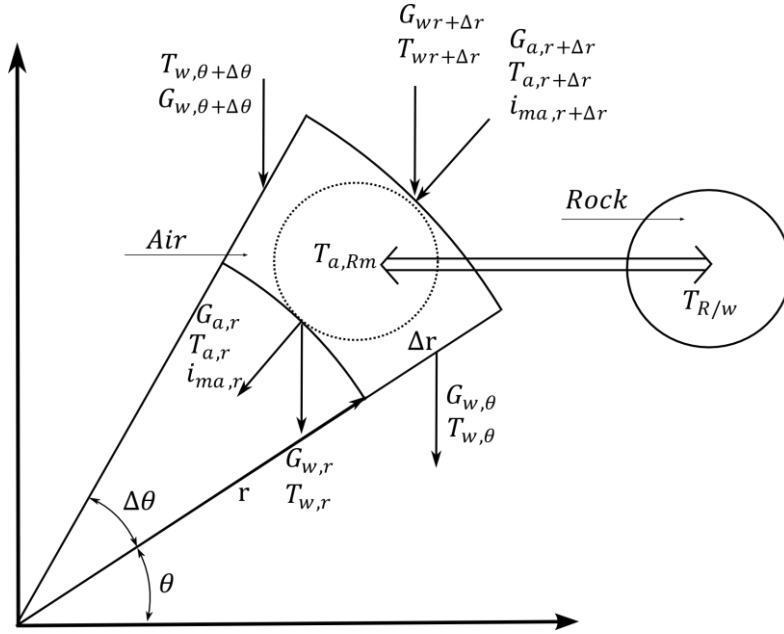
Figure 3.2: 2D Control volume of rock bed consisting of rock, air and water

As mentioned earlier, the governing equations describing the wet operation are presented in Appendix F.2.

3.1.1 Dry air operation

Again consider the control volume as shown in Figure 3.2 consisting of rock and air for a positive or negative charging or discharging cycle for dry air. It is assumed that radiation and conduction between particles are negligible and as air moves through the voids of the packed rocks, heat is transferred between the rocks and air only by means of convection. Also as explained earlier, no temperature gradient will exist within a rock particle so that the lumped capacitance approach can be used for modelling the rocks. The assumption made by Hughes et al. (1976) of negligble fluid capacitance is used. The convective heat transfer to rocks at the air-rock interface inside the control volume can be expressed as;

$$dQ_c = -h_c\big(T_R - T_{a,Rm}\big)dA_c = (1 - \varepsilon)\rho_R c_{v,R} r\Delta r\Delta\theta\Delta z \frac{dT_R}{dt} \tag{3.4}$$

The convection heat transfer area, dA_c, can be expressed as;

$$\mathrm{d}A_c = a_{Ri}A_{fr}\Delta r \tag{3.5}$$

where A_{fr} is the average frontal area between the inlet and outlet of the control volume, $A_{fr} = (r + 1/2\,\Delta r)\,\Delta\theta\Delta z\Delta r)$, and a_{Ri} is found from Eq.(2.12).

39

Substituting Eq. (3.5) into Eq. (3.4) the following can be obtained;

$$
\begin{aligned}
-h_c\big(T_R - T_{a,Rm}\big)a_{Ri}r\Delta\theta\Delta z\Delta r & \\
- \frac{1}{2}\, h_c\big(T_R - T_{a,Rm}\big)\, a_{Ri}r\Delta\theta\Delta z\Delta r^2 & \\
= (1-\varepsilon)\rho_R c_{v,R}\mathrm{r}\Delta\mathrm{r}\Delta\theta\Delta z\frac{dT_R}{dt} &
\end{aligned}
\tag{3.6}
$$

The Δr^2 term is assumed to be very small that the term including it can be neglected in the analysis. Dividing Eq.(3.6) with $-r\Delta r\Delta\theta\Delta z$, it can be written as;

$$
h_c a_{Ri}\big(T_R - T_{a,Rm}\big) = -(1-\varepsilon)\rho_R c_{v,R}\frac{dT_R}{dt}
\tag{3.7}
$$

Eq.(3.7) can be rearranged to find an expression describing the solid particle temperature at any time during operation of air heating or dry cooling as;

$$
\frac{dT_R}{dt} = -\frac{h_c a_{Ri}}{(1-\varepsilon)\rho_R c_{v,R}}\big(T_R - T_{a,Rm}\big)
\tag{3.8}
$$

Air is assumed to flow only in the radial direction. The heat transfer to air at the rock – air interface can thus be expressed as;

$$
\begin{aligned}
-G_{a,r+\Delta r}\,(r+\Delta r)\Delta\theta\Delta z\, c_{p,a}T_{a,r+\Delta r} - \big(-G_{a,r}\, r\Delta\theta\Delta z\, c_{p,a}\, T_{a,r}\big) & \\
- h_c\big(T_{a,Rm} - T_R\big)dA_c = 0 &
\end{aligned}
\tag{3.9}
$$

Again, divide Eq.(3.9) by $-r\Delta\theta\Delta r\Delta z$, to obtain the following;

$$
\begin{aligned}
\frac{G_{a,r+\Delta r}\, c_{p,a}T_{a,r+\Delta r} - G_{a,r}\, c_{p,a}\, T_{a,r}}{\Delta r} + \frac{G_{a,r+\Delta r}\, c_{p,a}T_{a,r+\Delta r}}{r} & \\
+ h_c a_{Ri}\big(T_{a,Rm} - T_R\big) = 0 &
\end{aligned}
\tag{3.10}
$$

Let $\Delta r \to 0$, and apply chain rule of differentiation assuming specific heat of air to be constant;

$$
\begin{aligned}
\frac{d\big(G_{a,r}\, c_{p,a}\, T_{a,r}\big)}{\mathrm{dr}} + \frac{G_{a,r}\, c_{p,a}T_{a,r}}{r} + h_c a_{Ri}\big(T_{a,Rm} - T_R\big) & \\
= c_{p,a}G_{a,r}\frac{\partial T_{a,r}}{\partial r} + c_{p,a}T_{a,r}\frac{dG_{a,r}}{dr} + \frac{G_{a,r}\, c_{p,a}T_{a,r}}{r} & \\
+ h_c a_{Ri}\big(T_{a,Rm} - T_R\big) = 0 &
\end{aligned}
\tag{3.11}
$$

Substitute Eq. (3.3) into above equation and rearrange to obtain an expression describing air temperature through the bed for all time steps;

$$
\frac{dT_{a,r}}{dr} = -\frac{\big[h_{c,aRm-R}a_{Ri}\big(T_{a,Rm} - T_R\big)\big]}{c_{p,a}G_{a,r}}
\tag{3.12}
$$

A complete energy balance over the control volume yields;

$$-G_{a,r+\Delta r}\,(r+\Delta r)\Delta\theta\Delta z\,c_{p,a}T_{a,r+\Delta r}-\left(-G_{a,r}\,r\Delta\theta\Delta z\,c_{p,a}\,T_{a,r}\right)$$
$$=(1-\varepsilon)\rho_R c_{v,R}\mathrm{r}\Delta\mathrm{r}\Delta\theta\Delta z\frac{dT_R}{dt} \tag{3.13}$$

Again, divide by $-r\Delta\theta\Delta r\Delta z$;

$$\frac{G_{a,r+\Delta r}\,c_{p,a}T_{a,r+\Delta r}-G_{a,r}\,c_{p,a}\,T_{a,r}}{\Delta r}+\frac{G_{a,r+\Delta r}\,c_{p,a}T_{a,r+\Delta r}}{r}$$
$$=(1-\varepsilon)\rho_R c_{v,R}\frac{dT_R}{dt} \tag{3.14}$$

Let $\Delta r\to 0$, apply chain rule of differentiation and substitute (3.3) to find;

$$c_{p,a}G_{a,r}\frac{\partial T_{a,r}}{\partial r}=(1-\varepsilon)\rho_R c_{v,R}\frac{\partial T_R}{\partial t} \tag{3.15}$$

By iteratively solving the rock and air temperatures using Eq.(3.8) and Eq.(3.12) respectively, while ensuring Eq.(3.16) is balanced, a converged solution can be found.

For the top of the system as discussed in 2.4, solar irradiation strikes the top layer during a positive charge cycle, heats up the top layers of rock and transfers heat to the rest of the system. Consider heat transfer of the transparent cover roof at the top and by using a lumped capacitance approach the following can be obtained;

$$I_i\alpha_{cp}A_{Ro}-h_{c,cp-am}\big(T_{cp}-T_{am}\big)A_{c,cp}-h_{r,cp-R}\big(T_{cp}-T_R\big)A_{c,cp}$$
$$-h_{r,cp-surr}\big(T_{cp}-T_{surr}\big)A_{c,cp}$$
$$-h_{c,cp-surr}\big(T_{cp}-T_{surr}\big)A_{c,cp}=0 \tag{3.16}$$

where A_{cp} is the exposed area of the cover plate and I_i is the incidence solar radiation on the system. It is further assumed that the sections considered at the top can be described using theory for flow between parallel plates.

As air enters the channel in the outer space, a portion of it is forced into the rock bed whilst the other portion heats up as it moves further up in the channel. Performing an energy balance the following can be obtained;

$$G_{a,\theta}\Delta r_\theta\Delta z c_{p,a}T_{a,\theta}-G_{a,\theta+\Delta\theta}\Delta r_\theta\Delta z c_{p,a}T_{a,\theta+\Delta\theta}$$
$$-\big(G_{a,\theta}-G_{a,\theta+\Delta\theta}\big)\Delta r_\theta\Delta z c_{p,a}\big(T_{a,m}\big)$$
$$=h_{c,am-cp}\big(T_{am}-T_{cp}\big)A_{c,cp}$$
$$+h_{c,am-R}(T_{am}-T_R)dA_{Ro} \tag{3.17}$$

Δr_θ is the thickness of the outer space air channel, thus the hydraulic diameter, $\Delta r_\theta=D_e$. Divide Eq.(3.17) by $-r_{Ro}\Delta\theta\Delta z D_e$, to find;

$$\frac{G_{a,\theta+\Delta\theta}c_{p,a}T_{a,\theta+\Delta\theta} - G_{a,\theta}c_{p,a}T_{a,\theta}}{r_{Ro}\Delta\theta} + \frac{(G_{a,\theta} - G_{a,\theta+\Delta\theta})c_{p,a}(T_{a,m})}{r_{Ro}\Delta\theta}$$

$$= -\frac{h_{c,am-cp}(T_{am} - T_{cp})}{D_e}$$

$$- h_{c,am-R}a_{Ri}(T_{am} - T_R)$$

(3.18)

Let $\Delta\theta \to 0$ to find the differential equation;

$$c_{p,a}\frac{\partial(G_{a,\theta}T_{a,\theta})}{r_{Ro}\ \partial\theta} - T_{a,m}c_{p,a}\frac{\partial G_{a,\theta}}{r_{Ro}\ \partial\theta}$$

$$= -\frac{h_{c,am-cp}(T_{am} - T_{cp})}{D_e}$$

$$- h_{c,am-R}a_{Ri}(T_{am} - T_R)$$

(3.19)

Consider the top layer of rocks that act as the absorber plate;

$$I_i\tau_{cp}dA_{Ro} - h_{r,R-cp}(T_R - T_{cp})dA_{Ro} - h_{c,R-am}(T_R - T_{am})dA_{Ro}$$

$$- h_{c,R-Rm}(T_R - T_{a,Rm})dA_{c,R}$$

$$= (1 - \varepsilon)\rho_R c_{v,R}r_{Ro}\Delta r\Delta\theta\Delta z\frac{dT_R}{dt}$$

(3.20)

Divide by $r\Delta r\Delta\theta\Delta z$ to obtain;

$$I_i\tau_{cp} - h_{r,R-cp}(T_R - T_{cp}) - h_{c,R-am}(T_R - T_{am})$$

$$- h_{c,R-Rm}a_{Ri}\Delta r(T_R - T_{a,Rm}) = (1 - \varepsilon)\rho_R c_{v,R}\Delta r\frac{dT_R}{dt}$$

(3.21)

By initially guessing a temperature for the cover plate and taking the mean air temperature to be the average between the cover plate and the top layer of rocks, the system can be solved by an energy balancing iterative approach.

3.1.2 Pressure drop

From Newton's law for conservation of momentum, stating that the rate of momentum accumulation is equal to the net transport rate of momentum and the sum of all the forces acting in on the element. The momentum accumulation is zero and the only forces considered acting in on the element are body and surface forces;

$$\sum\delta\vec{F} = \sum\delta\vec{F}_b + \sum\delta\vec{F}_s + \sum_{in}\dot{m}\,u_{r+\Delta r} - \sum_{out}\dot{m}u_r = 0$$

(3.22)

The body forces that are considered for fluid flowing through a porous medium are gravity- and frictional forces resulting from flow over solid particles. Consider the control volume as depicted in Figure 3.3.

The gravity force, acting throughout the entire control body of the fluid element, represented as a net force acting in on the middle of the control volume can be obtained for the radial- and theta direction respectively as;

$$\delta F_{g,r} = -\varepsilon \rho_a g \sin\left(\theta + \frac{\Delta\theta}{2}\right) r\Delta\theta\Delta r\Delta z \tag{3.23}$$

$$\delta F_{g,\theta} = -\varepsilon \rho_a g \cos\left(\theta + \frac{\Delta\theta}{2}\right) r\Delta\theta\Delta r\Delta z \tag{3.24}$$
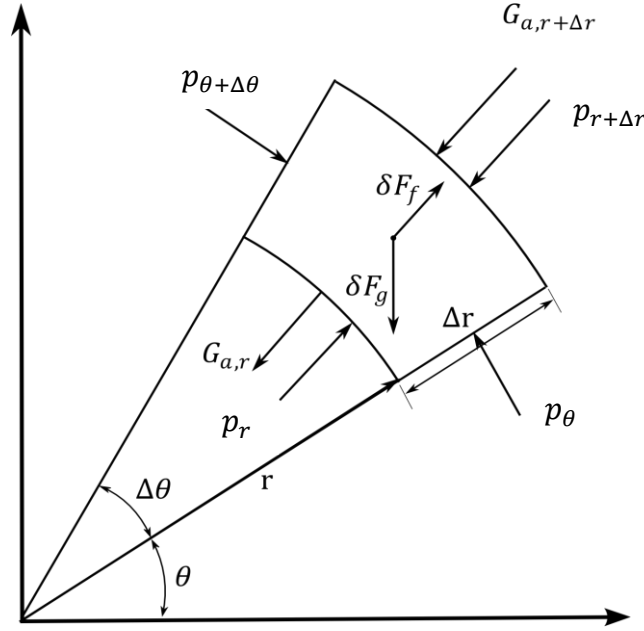
Figure 3.3: 2D Control volume for momentum conservation

In fluid flow, power, *P*, can be found by a differential pressure times the volumetric flow rate of air. It can also be obtained by multiplying the differential force that the flow needs to overcome with the flow velocity of air. An expression for power can be written as;

$$\delta P = \delta F_f u_a = \delta p Q \tag{3.25}$$

where Q is the volumetric flow rate of air. The pressure drop correlations of Allen et al. (2013) from Eq.(2.17) and Eq. (2.18) are based on measurements for cross- and co-current flow respectively. It is assumed that the flow will be in cross-current configuration at the bottom inlet of the rocks and changes linearly to co-current configuration at the top inlet of the rock surface and can be expressed as;

$$f_{tot} = (f_{co} - f_{cross})\frac{\theta}{\pi/2} + f_{cross} \tag{3.26}$$

43

Substitute the correlations from Allen et al. (2013) for co-current- and cross-current from Eq. (2.17) and Eq.(2.18) into Eq. (3.26) to find;

$$f_{tot} = \left[76.47 \left(\frac{1-\varepsilon}{Re_{pv}} \right)^{0.343} - 80.94 \left(\frac{1-\varepsilon}{Re_{pv}} \right)^{0.41} \right] \frac{\theta}{\pi/2}$$
$$+ 80.94 \left(\frac{1-\varepsilon}{Re_{pv}} \right)^{0.41} = \frac{\Delta p}{\Delta r \left(\frac{\rho_a u_a^2}{2} \right)} \frac{\varepsilon^3}{(1-\varepsilon)} D_v \tag{3.27}$$

Where the particle Reynolds number can be found using Eq.(2.11) in terms of the volume equivalent diameter defined by Eq.(2.8). By substituting Eq.(3.25) into Eq.(3.27) the following can be obtained;

$$\delta F_f = \frac{\Delta p Q}{u} = f_{tot} \left(\frac{\rho_a u_a^2}{2} \right) \frac{(1-\varepsilon)}{\varepsilon^3} \frac{1}{D_v} \tag{3.28}$$

The hydrostatic surface forces acting in normal on the surfaces of the control volume in Figure 3.3 can be expressed for the radial and theta direction respectively as;

$$\sum \delta F_{s,r} = p_r r \Delta\theta \Delta z - p_{r+\Delta r}(r + \Delta r)\Delta\theta\Delta z + p_\theta \Delta r \Delta z \sin\left(\frac{\Delta\theta}{2} \right)$$
$$+ p_{\theta+\Delta\theta}\Delta r \Delta z \sin\left(\frac{\Delta\theta}{2} \right) \tag{3.29}$$

$$\sum \delta F_{s,\theta} = p_\theta \Delta r \Delta z \cos\left(\frac{\Delta\theta}{2} \right) - p_{\theta+\Delta\theta}\Delta r \Delta z \cos\left(\frac{\Delta\theta}{2} \right) \tag{3.30}$$

The convective transport momentum is the kinetic energy of the mass of the fluid flowing in and out of the faces of the element in Figure 3.3. Since for the air model, no flow is present in the theta direction, only radial direction will be affected by the net convective transport;

$$\sum_{in} \dot{m} u_{r+\Delta r} - \sum_{out} \dot{m} u_r$$
$$= -\rho_a u_{a,r+\Delta r}^2 (r + \Delta r)\Delta\theta\Delta z - \left(-\rho_a u_{a,r}^2 r \Delta\theta\Delta z \right) \tag{3.31}$$

Substituting Eq. (3.23) to Eq. (3.31) into Eq. (3.22), the following can be found for the radial direction;

$$p_r r \Delta\theta \Delta z - p_{r+\Delta r}(r + \Delta r)\Delta\theta\Delta z + p_\theta \Delta r \Delta z \sin(\Delta\theta/2)$$
$$+ p_{\theta+\Delta\theta}\Delta r \Delta z \sin(\Delta\theta/2)$$
$$- \rho_{a,r+\Delta r} u_{a,r+\Delta r}^2 (r + \Delta r)\Delta\theta\Delta z$$
$$- \left(-\rho_{a,r} u_{a,r}^2 r \Delta\theta\Delta z \right) + \delta F_f \tag{3.32}$$
$$- \varepsilon\rho_a g \sin(\theta + \Delta\theta/2)r\Delta\theta\Delta z\Delta r = 0$$

44

Divide Eq. (3.32) by $-r\Delta\theta\Delta r\Delta z$, substitute Eq.(3.3) and apply chain rule of differentiation to obtain;

$$
\begin{aligned}
p_r r\Delta\theta\Delta z &- p_{r+\Delta r}(r+\Delta r)\Delta\theta\Delta z + p_\theta\Delta r\Delta z sin(\Delta\theta/2) \\
&+ p_{\theta+\Delta\theta}\Delta r\Delta z sin(\Delta\theta/2) \\
&- \rho_{a,r+\Delta r}u_{a,r+\Delta r}^2(r+\Delta r)\Delta\theta\Delta z \\
&- \left(-\rho_{a,r}u_{a,r}^2 r\Delta\theta\Delta z\right) + \frac{\delta F_f}{r\Delta\theta\Delta z\Delta r} \\
&- \varepsilon\rho_a g sin(\theta+\Delta\theta/2)r\Delta\theta\Delta z\Delta r = 0
\end{aligned}
\tag{3.33}
$$

Let $\Delta r, \Delta\theta \to 0$, apply chain rule of differentiation and make use small angle approximations to find;

$$
\begin{aligned}
\frac{\partial p_r}{\partial r} &+ \frac{p_r}{r} + \frac{p_\theta}{r} + G_{a,r}\frac{\partial\left(u_{a_r}\right)}{\partial r} \\
&- \left[76.47\left(\frac{1-\varepsilon}{Re_{pv}}\right)^{0.343} - 80.94\left(\frac{1-\varepsilon}{Re_{pv}}\right)^{0.41}\right]\frac{\theta}{\frac{\pi}{2}} \\
&+ 80.94\left(\frac{1-\varepsilon}{Re_{pv}}\right)^{0.41}\left(\frac{\rho_a u_a^2}{2}\right)\frac{(1-\varepsilon)}{\varepsilon^3}\frac{1}{D_v} \\
&+ \varepsilon\rho_a g sin(\theta) = 0
\end{aligned}
\tag{3.34}
$$

Similarly, for the theta direction, the pressure drop can be written as,

$$
\frac{\partial p_\theta(1-\Delta\theta^2/8)}{r\partial\theta} = -\varepsilon\rho_a g cos(\theta)
\tag{3.35}
$$

where $\Delta\theta^2$ term is found by using small angle approximations and is assumed to be negligibly small resulting in:

$$
\frac{\partial p_\theta}{r\partial\theta} = -\varepsilon\rho_a g cos(\theta)
\tag{3.36}
$$

By solving the pressure drop iteratively, along with rock and air temperatures, the performance of the system can be predicted.

3.2 Numerical model

The finite volume approach is chosen for numerical solution. The governing equations are discretised over a finite number of control volumes in terms of nodal values. The principle of this method is that the fluxes either heat or mass, over the control volume faces, must be zero when summed. The cylindrical domain is discretized into finite volumes in the quarter annulus. The volumes share a common border i.e. the control volume faces as shown in Figure 3.4. The partial differential equations above are discretized using a first order upwind method to determine the variable at the grid points for each control volume. The bed is divided into segments with constant Δr but have different volumes. The

temperature of the rock in a control volume is uniform in its radial and theta direction and the boundary nodes are treated separately.

To illustrate the method, the variable property, Φ, at the central grid point of the control volume is considered. The interfaces of the neighbouring cells are denoted as $a\ (above), b\ (below), r\ (right)$ and $l\ (left)$ whereas the central nodes of the neighbouring cells are *A*, *B*, *L* and *R* respectively. The derivatives for central grid points with respect to r and θ can be written in terms of facial values as;

$$\frac{\partial \Phi^t}{\partial r}_{X(i,j)} = \frac{\Phi^t_{a(i,j)} - \Phi^t_{b(i,j)}}{\Delta r} \tag{3.37}$$

$$\frac{\partial \Phi^t}{r\partial \theta}_{X(i,j)} = \frac{\Phi^t_{r(i,j)} - \Phi^t_{l(i,j)}}{r\Delta \theta} \tag{3.38}$$

The first order Euler explicit approach is used for the time dependent properties and can be written as;

$$\frac{\partial \Phi^t}{\partial t}_{X(i,j)} = \frac{\Phi^{t+\Delta t}_{X(i,j)} - \Phi^t_{X(i,j)}}{\Delta t} \tag{3.39}$$

A linear interpolation of the cell centred values is used to determine the values at the cell faces of the neighbouring control volumes as;

$$\Phi_{b(i,j)} = \Phi_{X(i,j)} + \frac{\left(\Phi_{X(i,j)} - \Phi_{A(i,j)}\right)}{2} \tag{3.40}$$

$$\Phi_{a(i,j)} = \frac{\left(\Phi_{A(i,j)} + \Phi_{X(i,j)}\right)}{2} \tag{3.41}$$

$$\Phi_{r(i,j)} = \Phi_{X(i,j)} + \frac{\left(\Phi_{X(i,j)} - \Phi_{L(i,j)}\right)}{2} \tag{3.42}$$

$$\Phi_{l(i,j)} = \frac{\left(\Phi_{L(i,j)} + \Phi_{X(i,j)}\right)}{2} \tag{3.43}$$

This method is illustrated by considering the 2-D dry air convective model for temperature gradients. The discretized governing equations are written as;

$$T^t_{a(i,j)} = \left(T^t_{a(i-1,j)} - \frac{\Delta r h^t_{(i,j)} a_{Ri}}{c_{p,a} G^t_{a(i,j)}} T^{t+\frac{\Delta t}{2}}_{R(i,j)} \right) \left(1 + \frac{\Delta r h^t_{(i,j)} a_{Ri}}{c_{p,a} G^t_{a(i,j)}} \right)^{-1} \tag{3.44}$$

46

$$T_{R(i,j)}^{t+\Delta t} = \left(T_{R(i,j)}^t + \frac{\Delta t h_{(i,j)}^t a_{Ri}}{(1-\varepsilon)\rho_R c_{v,R}} T_{a(i,j)}^t \right.$$
$$\left. - \frac{\Delta t h_{(i,j)}^t a_{Ri} T_{R(i,j)}^t}{(1-\varepsilon)\rho_R c_{v,R}} \right) \left(1 + \frac{\Delta t h_{(i,j)}^t a_{Ri}}{2(1-\varepsilon)\rho_R c_{v,R}} \right)^{-1} \tag{3.45}$$

$$G_{a(i,j)}^t = \frac{G_{a(i-1,j)}^t}{1 + \frac{\Delta r}{r}} \tag{3.46}$$

where $\Delta r = (R_{inlet} - R_{outlet})/N_r$,with R denoting the inlet and outlet radii and N_r the number of control volumes in the radial direction.
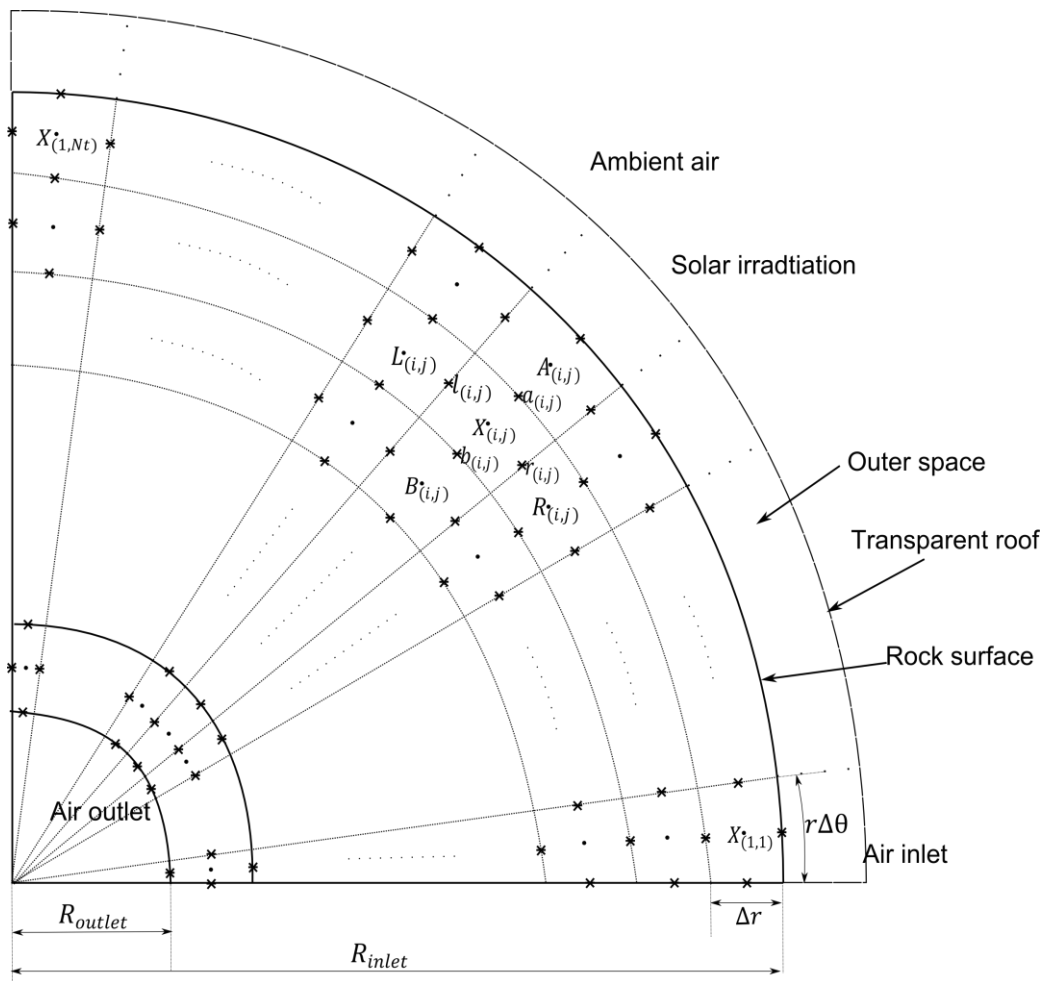

Figure 3.4: 2D Numerical grid selection

At the left hand side boundary for a position not at the inlet or outlet, the discretised equations would be the same for dry air. However, when water is considered, a new set of equations is necessary since no water passes through the left boundary face. The top and bottom nodes are treated separately with a new set of equations.

Time steps of less than 5 seconds and control volume radial lengths (Δr) smaller than 30 mm are found to be sufficient for grid independence of time and space for convergence of the governing equations. This is found by repeating simulations with different segment sizes and time steps to find the largest segment size and time step without variation compared to smaller increments.

3.3 Conclusion

In this section a governing equations describing the performance of the system is derived from first principles using conservation laws. A finite volume approach is used to divide the rock bed, into small elementary control volumes. In the model it is assumed that no inter particle radiation exists as stated by Jalalzadah-Azar et al. (1996). The thermal capacitance of the fluid is negligible from Hughes et al. (1976). The lumped capacitance model is applicable since the Biot number never exceeds 0.2 so no temperature gradients within particles will exist (Jefferson, 1972). Wall capacitance is not included in the analysis.

The convective heat transfer correlation of Wakao et al. (1978) is used to describe the temperature profile inside the rock bed. Correlations proposed by McAdams (1954), Duffie and Beckmann (1991) and Heaton et al. (1964) are used to determine convective heat transfer from the cover plate to air, radiation between surfaces and the sky and convective heat transfer in outer space channel respectively.

As for the pressure drop, it is assumed that the HYDROSOL is in a mixed cross and co-current packing orientation. Thus, at the bottom of the system the pressure drop is determined to be a cross current orientation changing linearly to co-current orientation at the top. The pressure drop correlations proposed by Allen et al. (2013) is used in the numerical model. By making use of the cylindrical co-ordinate model it is reasonable to assume that air only enters the rock bed in a radial direction.

The model is numerically discretized using a first order upwind scheme with an Euler approximation to predict values at next time step. The numerical model is implemented and solved with Scilab open source software.

4 Experimental evaluation of a HYDROSOL performance

In this section, the experimental apparatus is described that is used to measure the performance of HYDROSOL and to verify the numerical models presented in Section 3. The different measurement techniques used and appropriate material specifications are also presented and discussed. A test procedure is given in order to be able to repeat the experiments.

4.1 Experimental apparatus

The test facility is located next to the Mechanical and Mechatronic Engineering building at the University of Stellenbosch.

4.1.1 Description of test facility

Figure 4.1 is a basic depiction of the test facility used to measure the performance of the HYDROSOL system. It basically consists of a packed bed of crushed rocks, piled to form a natural angle of repose on one side. At the inner space, a steel grating is fitted to support the rocks and form an air channel at the bottom of the bed. A D_{pvc} = 110 mm PVC pipe with a rounded inlet is attached to the lower channel, leading to a centrifugal fan.
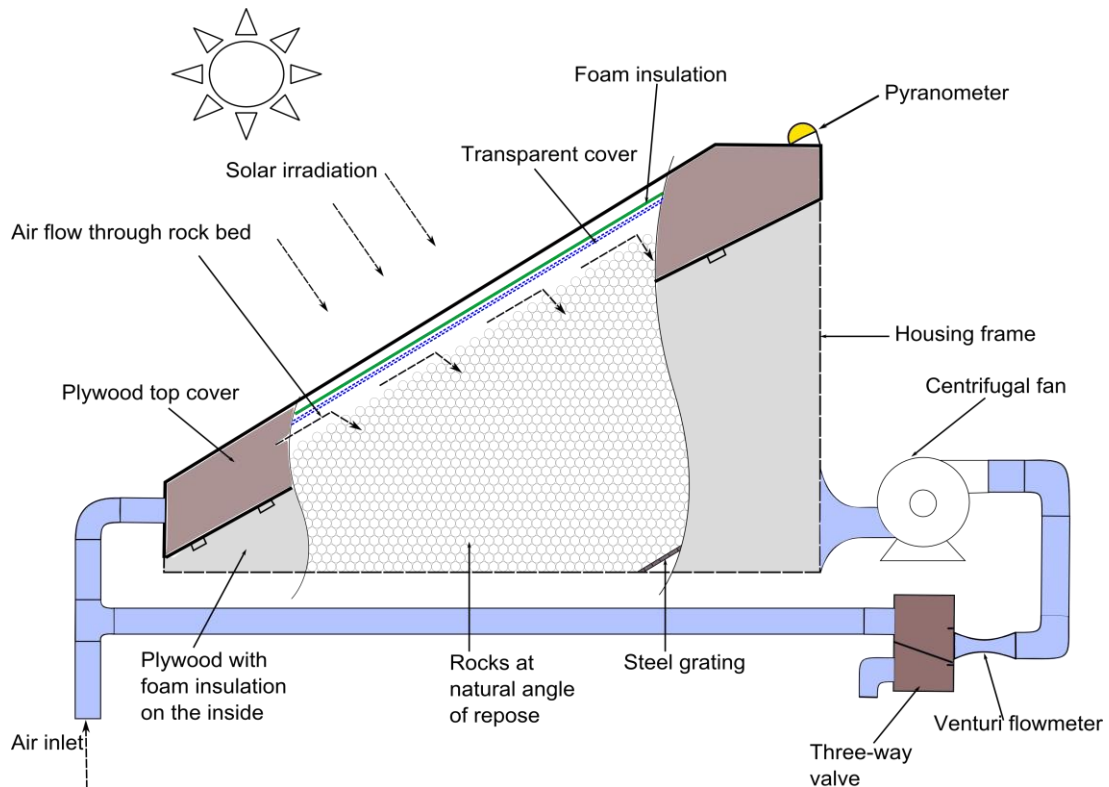

Figure 4.1:Schematic of test apparatus

49

Downstream of the fan, there is a three-way valve with one outlet pipe open to atmosphere and other connected to the HYDROSOL air inlet. A transparent roof made of polyethylene terephthalate glycol-modified (PETG), inclined at the same angle as the rocks, covers the rocks and has an air inlet opening at the bottom. A wooden box lid, which hinges on the sides, is used to cover the transparent roof, as shown in Figure 4.2 and Figure 4.3. When the system is covered with the box lid, polyurethane is placed between the cover and the transparent roof to minimise heat losses to the environment.

The apparatus is constructed with a galvanized steel outer frame to support the 21 mm thick plywood sheets that serve as the walls and floor to support the rock bed. The outer dimensions of the box are 2 m x 1.22 m x 2.5 m (L x W x H) with the side walls cut at the same angle as the rock pile's natural angle of repose. The inside of the bottom, back and side walls are insulated with 40 mm polyurethane foam, to reduce wall channelling effects and to minimise heat losses through the walls. Thermocouples are placed, equally spaced from each other, at various positions in the rock bed to measure rock and air temperatures.
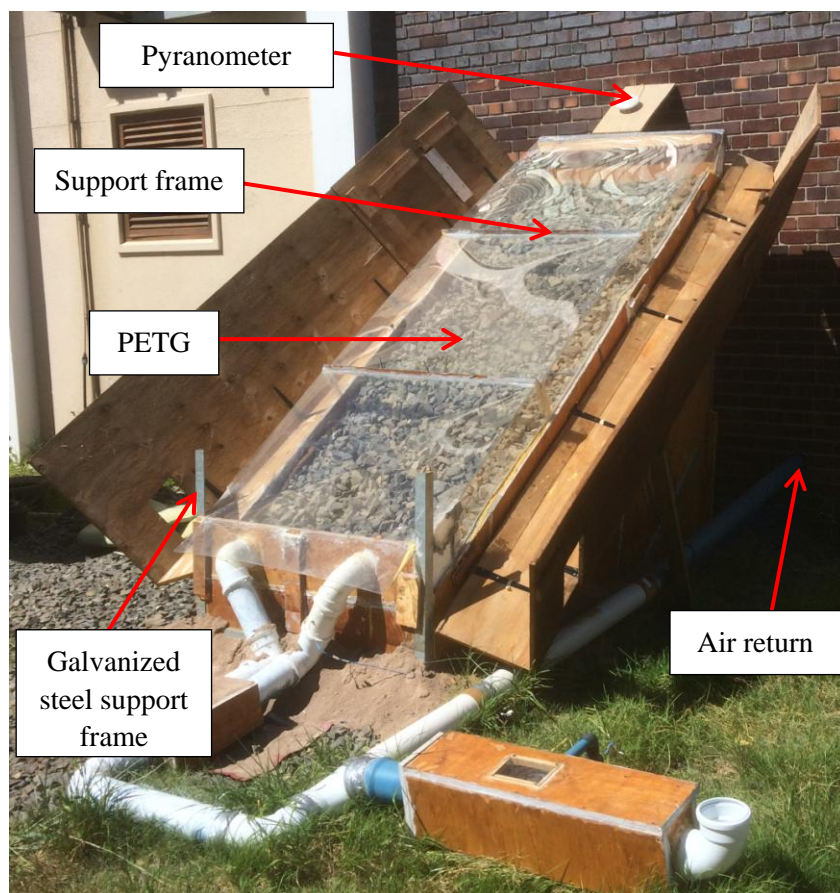

Figure 4.2: HYDROSOL test apparatus with RHRL open

50

The transparent cover is supported with 25 mm x 25 mm x 3 mm angle iron frames and sealed against the plywood walls. This cover forms a 200 mm air channel (outer space) in which air flows before penetrating the rock bed. At the inlet/outlet of the outer space, air is distributed over the frontal area by means of a manifold constructed from $D_{pvc} = 110$ mm PVC elbows. The system is completely sealed so that air enters or leaves the system through only the manifold.
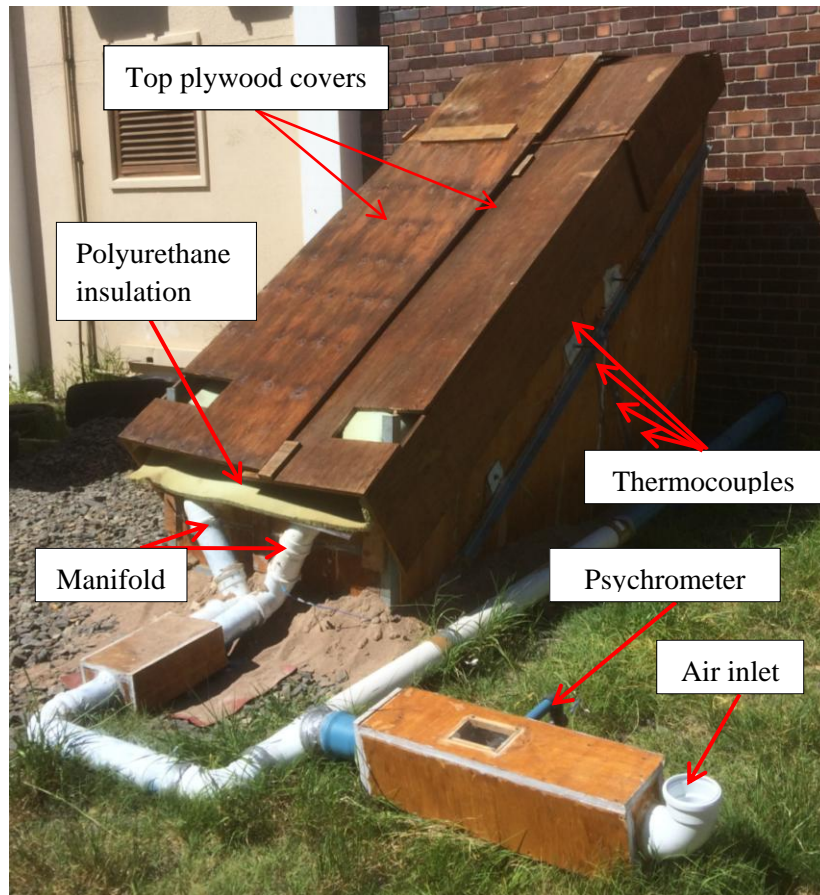
Figure 4.3: HYDROSOL test apparatus with RHRL closed

4.1.2   Basic operation

During forward flow, air enters at the air inlet, flows through the outer duct between the roof and the rocks before penetrating into the rock bed. It then passes between the rocks to the inner duct, where it flows into a pipe via a rounded inlet, through a centrifugal fan and then into a three-way valve. The flow leaving the three-way valve is either discharged to the atmosphere or is piped back to the air inlet for re-circulation. During reversed flow, the flow is in the opposite direction (by physically reversing the centrifugal fan flow direction).

When heating the rock bed during positive charging mode, the transparent roof is uncovered, allowing sun to heat the rocks on the surface of the pile. The heat is transferred to air moving over the rocks, and transfers the heat to the rest of the bed. A thermocline forms in the rock bed at the top and shifts through to the outlet. Once the desired temperature can be harnessed from storage, the three-way valve directs it to the room, or re-circulates it back to the inlet to heat up further.

Similarly when cooling the rock bed during a negative forward charge mode, the transparent roof is uncovered during the night and covered in daytime to block out solar heat. Cool night time ambient air is used to cold charge the bed and is extracted from it during the day as needed.

The air valve located at the positive forward outlet, depending on forward or backward operation, is configured to either dump (forward) the air in the room or be directed back to the inlet of the system. In the closed configuration, air is circulated back to the inlet (positive or negative) in a circulation configuration through the air return PVC pipes for configurations as shown in Figure 1.8 (b) and Figure 1.8 (c).

The system is checked for leaks on a weekly basis by measuring inlet and outlet mass flow rate with a digital handheld flow anemometer.

4.1.3 Material specifications used in experiment

The rock type used in the experiments is hornfels (also known as whetstones), which is a non-foliated metamorphic rock, found near Durbanville, in the Western Cape from the Portland quarry. The natural angle for this specific rock is found to be approximately $37°$. This angle is an approximation, found from pictures taken at the quarry where rocks are dropped from the top of the conveyor belt to a flat surface, relative to the ground. The rock is characterized by its fine grains, hardness and its toughness. This rock type is also extremely durable since it originates from sedimentary rock types that have undergone some textural changes because of temperature and pressure increases in the earth's crush (caused mainly by magma). The crushed hornfels with the measured volume equivalent diameter of $D_v =$35.2 mm, is locally known as Portland ECONOMIX.

The volume equivalent diameter of the rocks is found by measuring the volume displacement of water in a plastic measuring cylinder while adding randomly selected samples of rocks, dividing this volume by the number of rocks that are added to determine the mean volume of one rock and then determining the diameter of a sphere with the same volume as shown in Appendix B. Similarly, the density of the rocks is found to be approximately $\rho_R \approx$ 2600 kg/m^3 by weighing the rock samples and measuring the displacement of water when the rocks are added. The specific heat of the specific hornfels is found to be approximately $c_{v,R} \approx$ 820 J/kgK from experimental results obtained by Allen et al. (2013) which correlates well with the correlation proposed by Waples and Waples (2004).

The top transparent cover, as mentioned earlier, is a polyethylene terephthalate glycol-modified (PETG) cover, which is about half the weight of glass and has excellent impact resistance. The transmissivity of the plastic was measured by Rohwer (2013) to be $\tau_{cp} = 88.51$ % at a 100 mm height from the pyranometer which is slightly higher than the minimum of 86 % as indicated on the specification sheets (which do not indicate the distance from the PETG to the measurement equipment). Although it is slightly more expensive than glass it offers a high UV durability; it is easy to machine, has high impact resistance and is flexible, which makes the handling of it much easier. More specifications of the PETG can be found in Appendix H.

4.2   Measurements

Figure 4.4 shows the measurements that are recorded during heating and cooling experiments. A pyranometer is placed at the top of the bed above the transparent roof to measure solar irradiation present on the bed aperture. A total of 29 calibrated thermocouples are used to measure temperatures while pressure transducers are used to measure pressure drop over a venturi flowmeter, in order to calculate mass flow rate, as well as the pressure drop over the rock bed in order to estimate fan power.
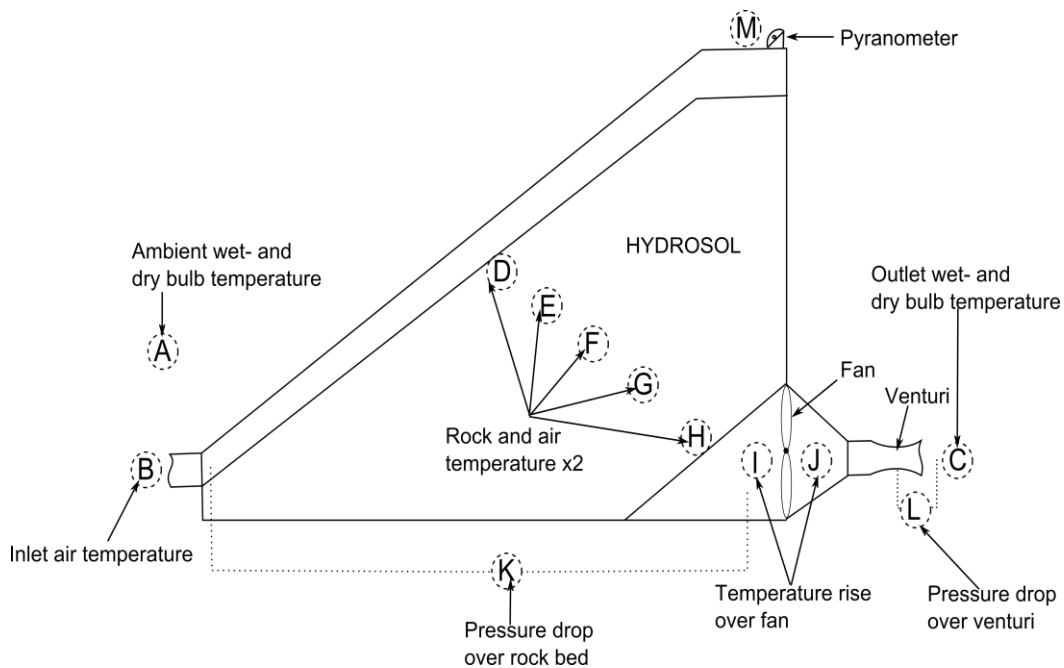

Figure 4.4: Measurement stations on the apparatus

Labelled 'A' on Figure 4.4 is where the inlet air dry- and wet bulb measurements are taken in a psychrometer. At 'B', air temperature is measured being either outlet air (backward operation) or inlet air that is not necessarily at ambient

temperature (circulation operation). Labelled 'C' is the outlet air temperature that again measures dry- and wet bulb temperatures in psychrometers. Two measurements of each are recorded at each location, to identify faulty thermocouples and to take an average reading of the data for the analysis. Inside the rock bed, air and rock temperatures are measured at 'D' to 'H', equally spaced from top to bottom, at the left and right hand side of the bed near the middle. At the outlet, the temperature rise caused by the fan is measured with thermocouples 'I' and 'J' since this needs to be taken into account in a circulation analysis. The available solar irradiation is measured by means of a pyranometer placed on top of the transparent PETG cover, 'M'. The pressure drop over the packed bed of rocks is measured at 'K' in order to determine fan power. A more detailed approach, taking into account all the bends and junctions as well as pipe friction factors need to be considered in practical design. The pressure drop over a venturi flowmeter is measured at 'L'.

4.2.1 Temperature

All thermocouples used in the experiments to measure air (wet-bulb and dry-bulb) and rock temperatures are calibrated T-type thermocouples. Thermocouples are calibrated with a FLUKE 9142 Field Metrology Well along with a reference Platinum Resistance Temperature Detector (PRTD) last calibrated in 2013. The reference PRTD is measured along with four thermocouples at a time at different temperatures. The temperatures are achieved by setting the FLUKE equipment to 0 °C and allowed sufficient time for it to stabilize. The FLUKE equipment, with built in temperature reading, is increased in increments of 10 °C until 60 °C is reached. The temperatures for each thermocouple are logged at a reference point and the average of the readings is used to calibrate a thermocouple with regards to the PRTD. By making use of a linear regression between the measured values from the individual thermocouples and the PRTD, the coefficients for the linear equation can be obtained as;

$$T_{calibrated} = mT_{measured} + c \qquad\qquad (4.1)$$

The readings and calibrated values can be found in Appendix C.

The rock temperatures in the bed are measured by drilling a hole to approximately the centre of the rock. The sheath of the thermocouple are stuck in the hole, sealed with rubber O-rings and glued at the top as shown in Figure 4.5.
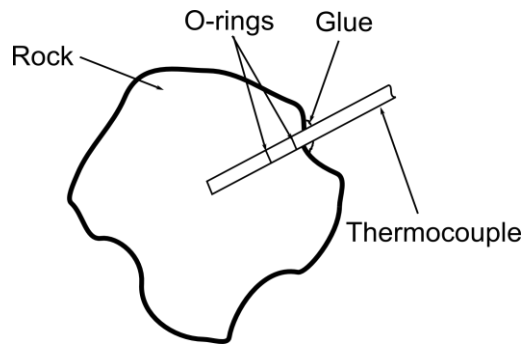
Figure 4.5: Rock temperature measurement technique

Air temperatures in the rock bed at the same positions as the rocks are measured by sticking the tip of the thermocouple in a PVC housing, as shown in Figure 4.6, aligned with the direction of the air flow. This is to ensure the tip of the thermocouple measures only the air temperature and not the surface temperature of the rocks.
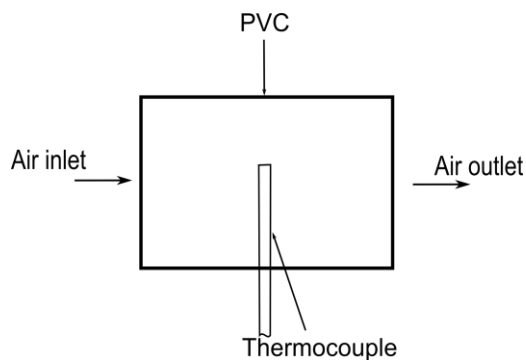

Figure 4.6: Air temperature probes in the rock bed

Figure 4.7 illustrates a psychrometer constructed from 20 mm PVC pipes, elbows and T-junctions in order measure dry- and wet bulb temperatures of air. At the inlet and outlet of the system, air temperature is measured by inserting the psychrometers so that the air flows through the pipes and then directed back into the main air stream. Inside the psychrometers, two thermocouples are positioned parallel with the flow direction. The one thermocouple is covered in a cotton wick and the tip of it is submerged in distilled water in the reservoir, measuring wet bulb temperature as air becomes saturated over the wet wick. The other thermocouple is positioned so that the tip of it is just further upstream than the wet bulb thermocouple. This thermocouple is uncovered and measures the dry bulb temperature. The psychrometer is constructed according to the standards as documented in ASHRAE 41.1.
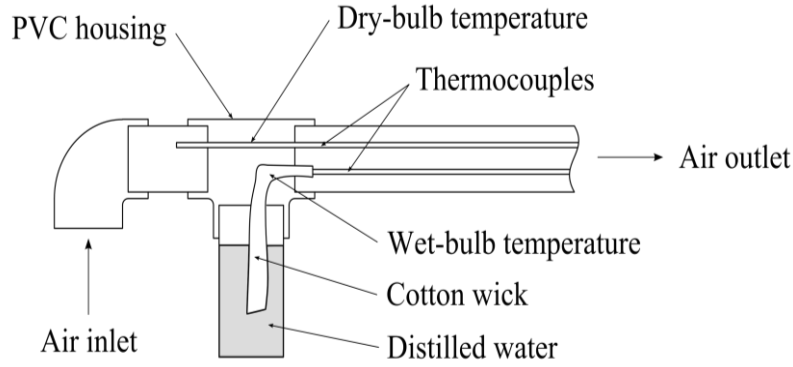
Figure 4.7: Psychrometer modified from Anderson (2014)

The psychrometers are fitted in ply wood rectangular ducts with a frontal area of $A_{fr} = 0.075 \ \mathrm{m}^2$. Operating the system with mass flow rates between $\dot{m}_a = 0.1 \ \mathrm{kg/s}$ and $\dot{m}_a = 0.2 \ \mathrm{kg/s}$, result in velocities between $u_{a,psy} = 1.1 \ \mathrm{m/s}$ and $u_{a,psy} = 2.2 \ \mathrm{m/s}$, over the thermocouples in the psychrometers, respectively.

4.2.2 Pressure

Figure 4.8 shows the Endress & Hauser (4-20 mA) pressure transducers that are used in the experiments. All of the transducers are calibrated using a Betz manometer. Calibration data for the transducers is found in Appendix C. The pressure transducer labelled 'A' measures the pressure drop over the rock bed. Pressure taps are fitted on the PETG cover at various positions along its length in order to find an average pressure drop reading. Transducer 'B' is connected to a calibrated venturi flowmeter where the output voltage is converted to a mass flow rate as discussed in Appendix C.3. Pressure transducer 'C' is used to measure the pressure drop over the entire system (including pipes, elbows, junctions and fan).
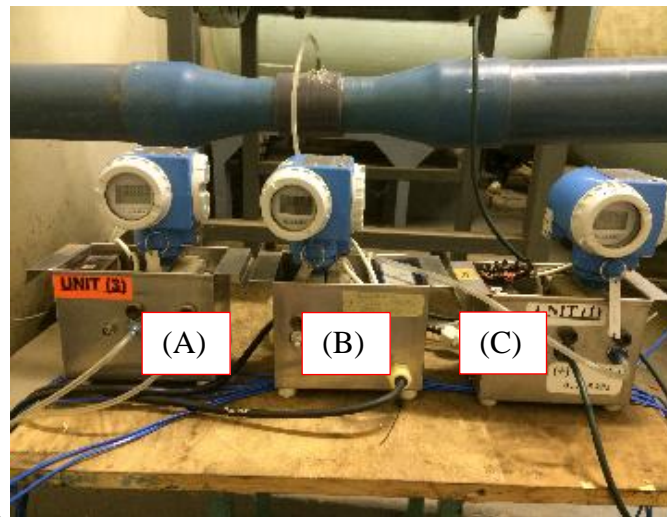

Figure 4.8: Pressure transducers

56

4.2.3   Air mass flow rate

A calibrated venturi flowmeter constructed from two PVC reductions is used to measure mass flow rate through the system. Two pressure taps, as shown in Figure 4.9, are used to connect tubes to the venturi flowmeter and the pressure transducer. The venturi flowmeter is calibrated by means of a pressure drop reading over standard nozzles converted to mass flow rate from experiments conducted in a wind tunnel setup as discussed in Appendix E. Measurements are confirmed with a digital handheld anemometer. Venturi flowmeter calibration data can be found in Appendix C.
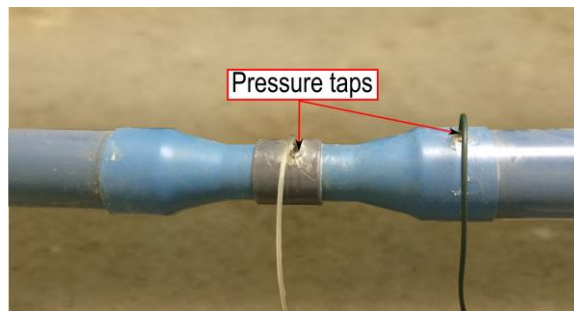

Figure 4.9: Installed venturi flow meter

4.3   Test procedure and experiment preparation

Before dumping rocks into the sealed container, they are thrown onto a sieve and washed to get rid of dust and any fractured particles. Thermocouples are placed in the test section on different radii while dumping the rocks from the top allowing it to form at its natural angle of repose.

The first check when conducting experiments is to ensure that the pressure transducers read a calibrated zero reading before the system is started. It is recommended to calibrate the transducers at least every second week since a zero reading of up to 1 Pa is found after not being used for 3 weeks which is quite significant over the low measured pressure drops. The reservoirs of the psychrometers are filled daily with distilled water, ensuring that the cotton wicks are thoroughly wet without touching the tip of the dry-bulb thermocouple. The atmospheric pressure is measured and logged with a manual reading from a mercury column barometer located near the test apparatus.

The centrifugal fan is then switched on, allowing air to flow through the psychrometers. The wet bulb readings are logged and compared to other thermocouples at the same position. The mass flow rate is adjusted with the variable speed drive setting it to the desirable flow rate from the pressure drop reading over the venturi flowmeter.

For a positive forward charge and discharge mode of operation, the pyranometer is placed on top of the system. The insulated plywood cover is hinged open once the full aperture of the bed receives solar irradiation. The PETG cover is wiped clean from any dust or other particles that can reduce transmissivity. Temperature and pressure are measured before and after the centrifugal fan to account for the temperature and pressure rise resulting from its operation that needs to be taken into account in the numerical model.

Once no more solar irradiation falls onto the rock bed, the PETG cover is hinged closed once again. Depending on the specific test, the centrifugal fan can be switched off, left running or manually reversed to perform backward discharge tests. The air dampers are controlled manually or by the programmed microcontroller to redirect flow. For the negative forward charge or discharge mode, the PETG covers are hinged open during the night while closing it before sun rise. Data acquisition is discussed in Appendix D.

4.4   Conclusion

This section discusses the experimental apparatus and the considerations in order to measure temperature profiles and pressure drop over the rock bed. Hornfel rocks from Portland quarry, with a measured volume equivalent diameter of $D_v = 35.2$ mm, is used in the system. The selection of rock type is based on transportation cost to test facility and regional availability.

The measurement techniques and setup is discussed with appropriate references to appendices for calibration data. Rock particles are washed and dumped into the wooden box, measuring the volume before throwing it in from the top. A test procedure in order to be able to repeat the experiments are presented.

5 Results and discussion of results

In this section, the 2-D thermal and pressure drop model is compared to measurements from the HYDROSOL apparatus and discussed. Parameters influencing the pressure drop and thermal behaviour of the rock bed are presented to augment optimum rock bed design for best performance.

5.1 Model verification

The modelled values for pressure drop as well as air and rock temperature distribution in the rock bed are compared to measured values obtained from the experimental apparatus. Deviations from measured values are presented in terms of a percentage deviation which can be calculated using the following;

$$\%Deviation = \left(\frac{\phi_{measured} - \phi_{predicted}}{\phi_{measured}}\right) \times 100\ \% \tag{5.1}$$

where ϕ is property considered. Markers on the graphs in the preceding sections do not necessarily indicate data points and will be clearly indicated when they do.

Experiments are conducted during different days in the winter and summer time. The values obtained for duct hydraulic diameter is $D_e = 0.48$ m, for equivalent rock diameter is $D_v = 0.035$ m, for rock specific heat is $c_{v,R} = 820$ J/kgK, for rock density is $\rho_R = 2600$ kg/m^{3}and, for single glazing, the Boltzmann constant is $\sigma = 5.67 \times 10^{-8}$ W/m^{2}K and emissivity of the rock and the cover plate are $\varepsilon_R = 0.9$, and $\varepsilon_{cp} = 0.9$ respectively. Effective outer radius of the bed, based on the same volume is found to be approximately $R_{eff} = 2$ m. Considering the plan view blockage factor of spheres packed in a square unstaggered pattern, it can be shown that 20% of solar irradiation penetrates through to the second layer of rocks.

5.1.1 Pressure drop over rock bed

Figure 5.1 illustrates the simulated pressure drop over the HYDROSOL apparatus when the rocks are considered to be in a cross and co- current packing orientation from Eq.(2.18) and Eq.(2.17) respectively as well as the measured pressure drop over the system. Markers in this figure represent data points. Mass flow rate is varied while measuring the pressure drop. It can clearly be seen that the assumption of the whole bed being co-current orientation will result in higher pressure drops over the rock bed at the same mass flow rates than the rock bed being in a cross-current orientation. However, since the rocks are allowed to form at its natural angle of repose, resulting in a mixture of the two orientations, it is expected that the measured pressure drop over the rock bed be somewhere between the two extreme limits.

From Figure 5.1 it can be seen that this is well the case especially at mass flow rates less than 0.2 kg/s. It is found that the actual pressure drop is in better correlation with cross–current orientation as mass flow rate increases. A slight over prediction occurs as mass flow rates go above 0.2 kg/s. This is not a major concern since the Biot number is the limiting factor for mass flow rate, and at $\dot{m}_a = 0.2$ kg/s the Biot number exceeds the limit of Bi ≤ 0.2.
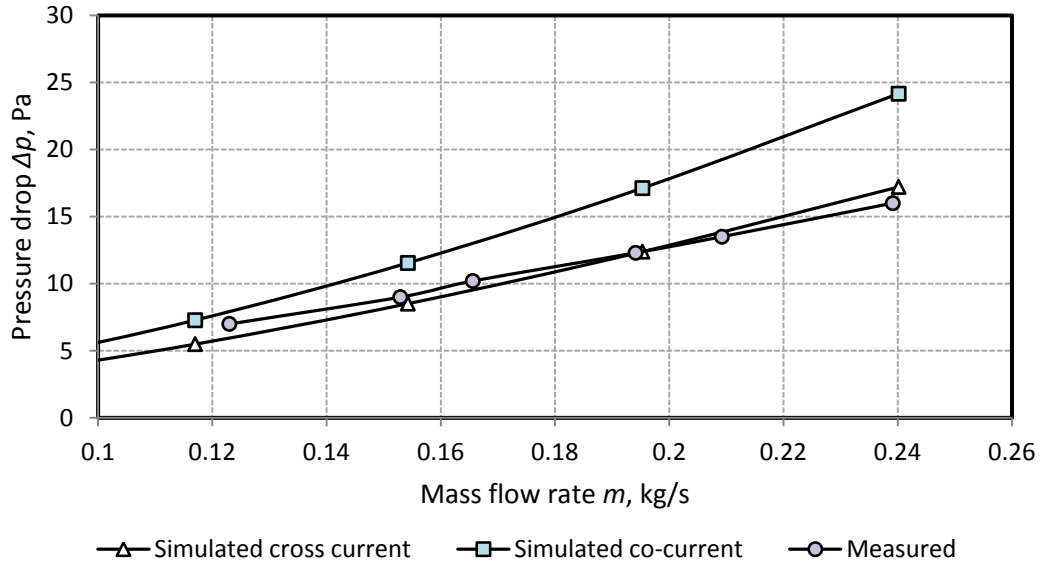

Figure 5.1: Pressure drop over the rock bed

For this specific rock bed, the pressure drop can be obtained with;

$$\Delta p = 95.239 \, \dot{m}_a^{1.2481} \tag{5.2}$$

5.1.2 Thermal model in rock bed

Figure 5.2 illustrates the temperature profile between outlet air temperature of the measured and predicted distributions from experimental setup as described in Appendix E. The predicted thermal performance is found by using the convective heat transfer correlation of Wakao et al. (1978) from Eq.(2.10).

The inlet air is heated with a water-air heat exchanger to approximately 72 °C until the whole bed is at this temperature. Ambient air, at approximately 18 °C (and fairly constant for the duration of the experiment) is used to discharge the bed at a Biot number of approximately 0.2. Good agreement between the predicted values and measured values are found with a maximum deviation of 4 % and it can be concluded that the correlation proposed by Wakao et al. (1978) can be used with confidence. No losses to the atmosphere are considered and although the experimental setup is fitted with polyurethane on the inside wall to reduce wall effects, it is found that temperatures close to the wall changed slightly faster than temperatures deeper in the bed indicating a faster air velocity at the

side. This effect is found for both cross- and co-current orientation. Despite this effect, an average temperature results in a fairly good agreement with the Wakao et al. (1978) convective heat transfer correlation.
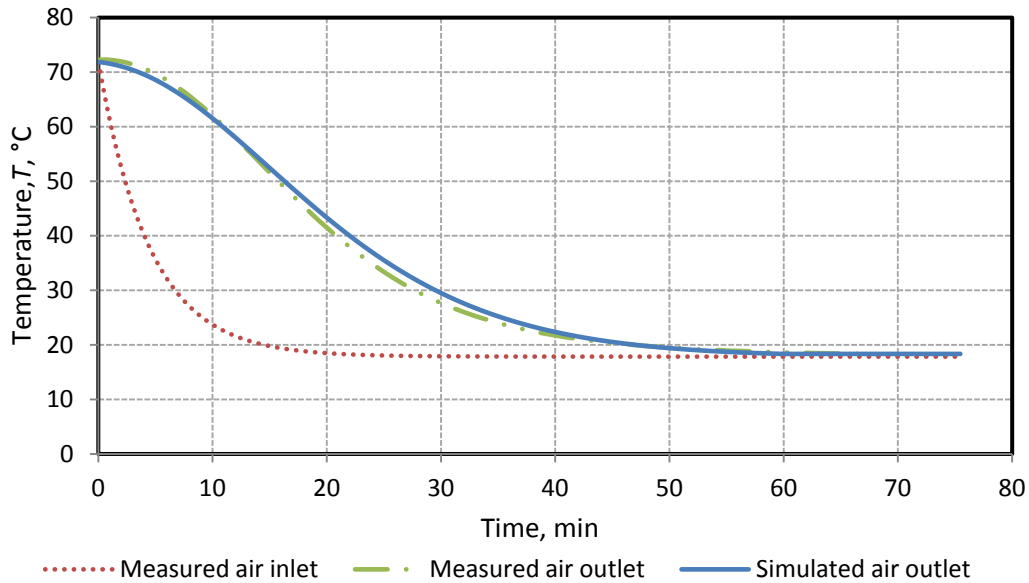

Figure 5.2: Validation of heat transfer coefficient (cross current orientation)

Figure 5.3 shows the top layer of rocks with the available solar irradiation for a positive forward charge mode of operation of the HYDROSOL apparatus for a day. The experiment is performed at a constant mass flow rate of $\dot{m}_a = 0.135 \, \text{kg/s}$ ($Bi \approx 0.13$), on a warm sunny day during October with ambient temperature rising above 30 °C during midday. The RHRL is opened at 8:00 when the full aperture received *DNI* and closed when no more visible *DNI* is present. A temperature rise of more than 25 °C is measured at the top for rocks compared to ambient air. It should be noted that the pyranometer is placed on top of the transparent roof at the tilted angle to measure maximum available solar irradiation in order to define efficiency of the system for a day.

Figure 5.4 shows the same data from the experiment explained in Figure 5.3 but only for the outlet in the inner space of the system during positive charge and discharge cycle. It can be seen that the predicted outlet values correlate very well with the measured outlet temperatures. A maximum deviation of less than 4 % is found when comparing the measured- to the predicted values. Again, the ambient temperature is shown on the plot to compare temperatures. It can be seen that a temperature of approximately 47 °C can be harvested at about 22:00 for the constant mass flow rate which is a temperature rise of almost 24 °C. The extraction of stored energy can be controlled by adjusting the mass flow rate. This type of operation, where heating is required during summer, would be ideal for drying of foods or goods such as wood pellets, fuel elements, etc. When heating is the primary concern, the hottest air of the outlet and ambient air would be used in

61
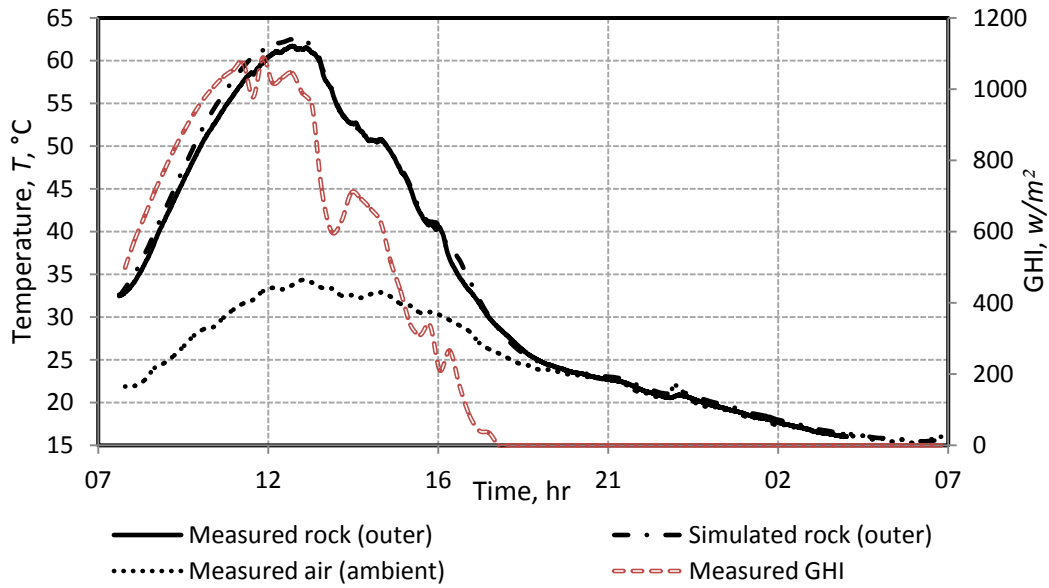
Figure 5.3: Positive forward charge-discharge of HYDROSOL – outer space, inlet
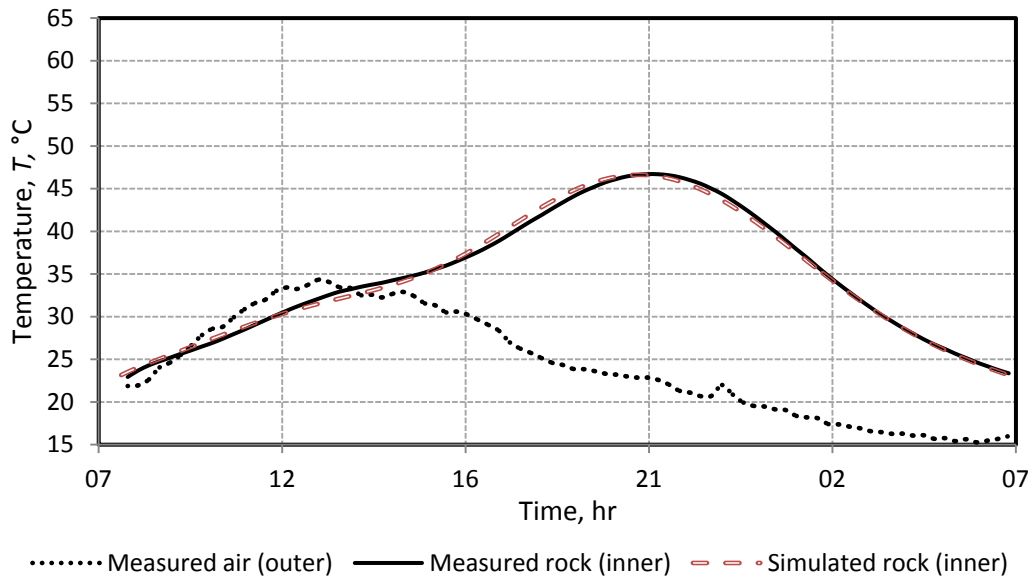
Figure 5.4: Positive forward charge-discharge of HYDROSOL – inner space, outlet

The case of positive forward charge and positive backward discharge is shown in Figure 5.5 and Figure 5.6. This experiment is performed during an average day in the winter at a constant charge and discharge mass flow rate of $\dot{m}_a = 0.16$ kg/s and $\dot{m}_a = 0.1$ kg/s respectively. Again it can be seen that the top layer predicts a general trend of the measured data during the day with a maximum deviation of 5.2 % based on temperature difference at specific times. The thermocline shifts

62

forward through the bed during the charge cycle and is then reversed during the discharge cycle. This can be seen from top rock temperature that starts to cool down and heats up again as the flow is reversed at approximately 17:00. It should be noted that ambient temperature is not used as the inlet air for the positive backward discharge but rather room temperature of the laboratory. A 12 °C temperature rise between ambient air and outlet for the outer space air is found.
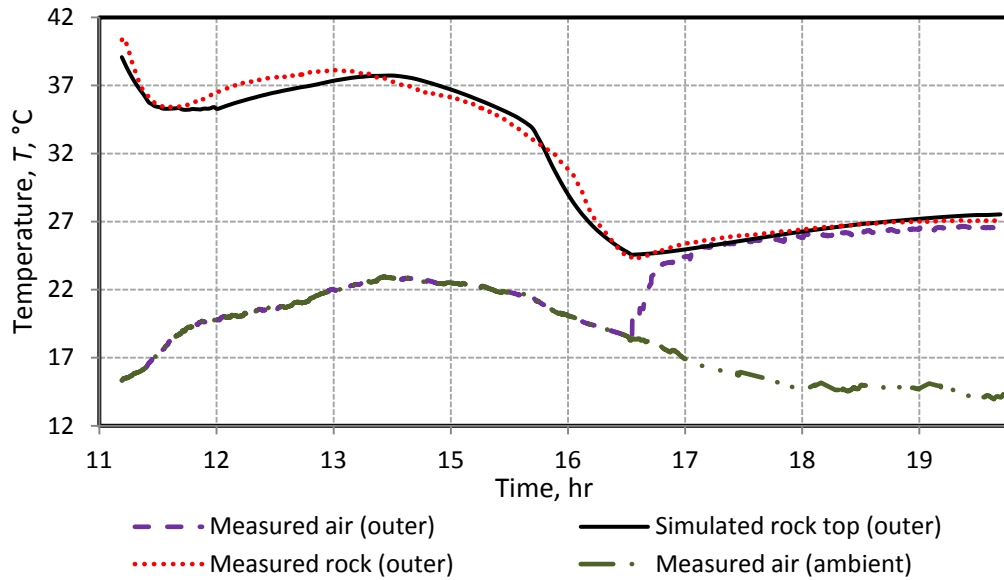

Figure 5.5: Positive forward charge- positive backward discharge of HYDROSOL-outer space, inlet-outlet
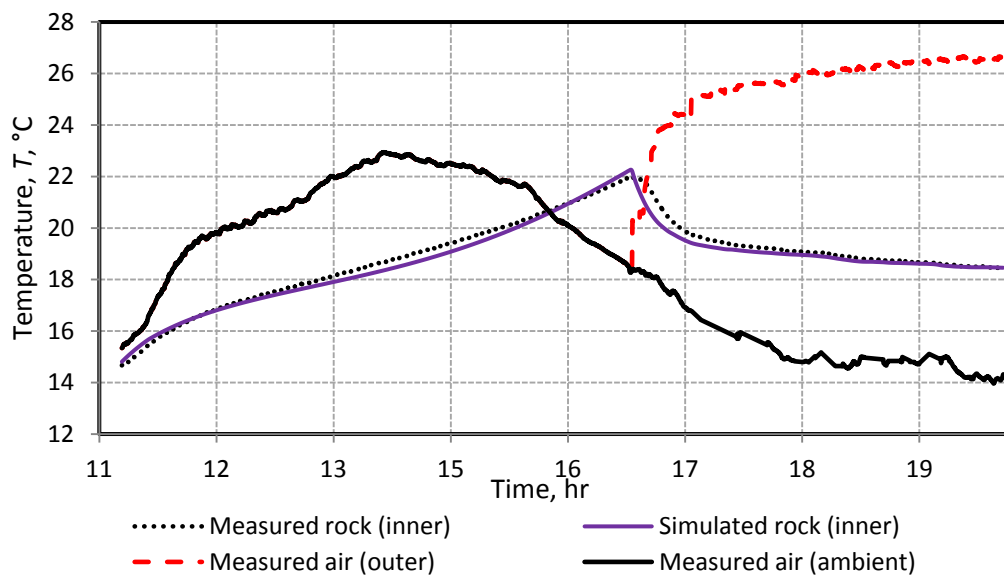

Figure 5.6: Positive forward charge- positive backward discharge of HYDROSOL – inner space, outlet- inlet

63

Figure 5.6 again shows the same experiment with rock temperature at the inner space on the steel grid. After the switch to backward discharge, the rocks quickly cool down to basically the same temperature as the room. The simulated model happens immediately while the experiment takes a few minutes to switch direction (manually reversing centrifugal fan). This effect is present on the results with a slight lag compared to the predicted temperatures. Despite this lag, a maximum deviation of less than 8 % is found.

Similarly for convective dry cooling, the measured and predicted rock temperatures, for the rock at the outer and inner space, are shown in Figure 5.7 and Figure 5.8 respectively for an average day during summer. The rock bed is initially cold charged with the outlet temperature at approximately 23 °C and still decreasing as the thermocline shifts through. The RHRL is closed for the full duration of the experiment. This experiment is performed at a constant mass flow rate of $\dot{m}_a$ =0.135 kg/s resulting in a maximum Biot number at the outlet of approximately $Bi \approx 0.13$. A maximum deviation of approximately 6 % is found at the top as shown in Figure 5.8. Ambient temperature is used in the numerical analysis since fresh air in broilers is one of the main concerns required for oxygen and ammonia removal. Storage is depleted when the thermocline moves through the bed and the outlet temperature becomes warmer than the ambient temperature.
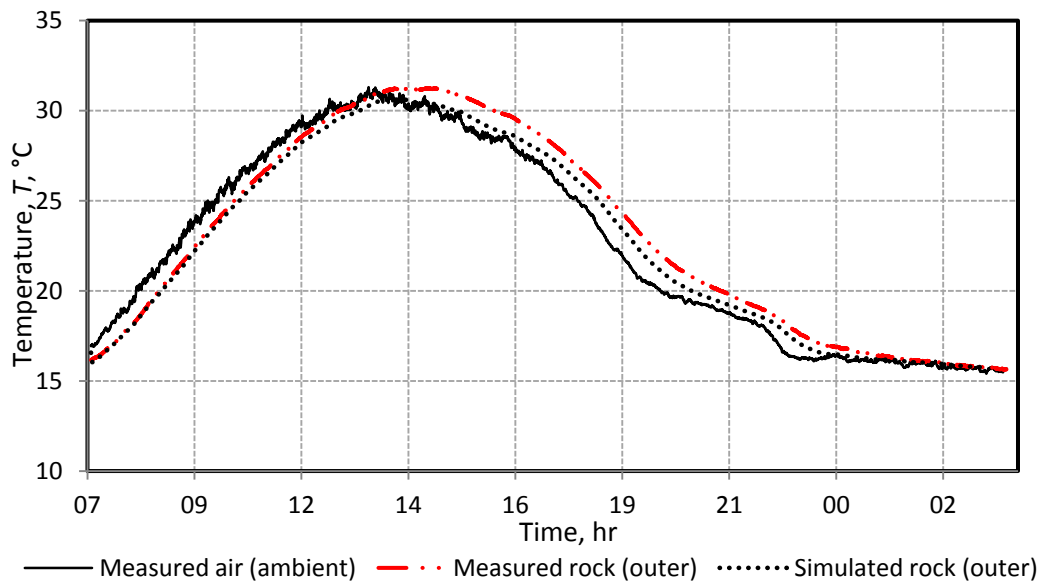
Figure 5.7: Negative forward discharge - negative forward charge of HYDROSOL – outer space, inlet

As the thermocline starts to move through the rock bed, it is being discharged at the inner space outlet as can be seen in Figure 5.8. At roughly 08:30 AM, the outlet air of the system becomes lower than the outside ambient temperature and can thus be effectively used for cooling in an enclosed environment. An outlet temperature of less than 21 °C can be achieved for more than 8 hours at this

constant mass flow rate. At approximately 18:30 the outlet air becomes hotter than the outside air and the bed starts a cold charge cycle for the next day. Depending on the application, the system can be switched off if no more cooling is needed during the night time, or switched to ambient air if further cooling is required. When a more constant temperature is necessary, the warmer outlet air and ambient air can be mixed during the night (or day) to achieve this. Predicted values at the outlet are in good agreement with measured data with a slight under prediction resulting in a maximum deviation of less than 3 %.
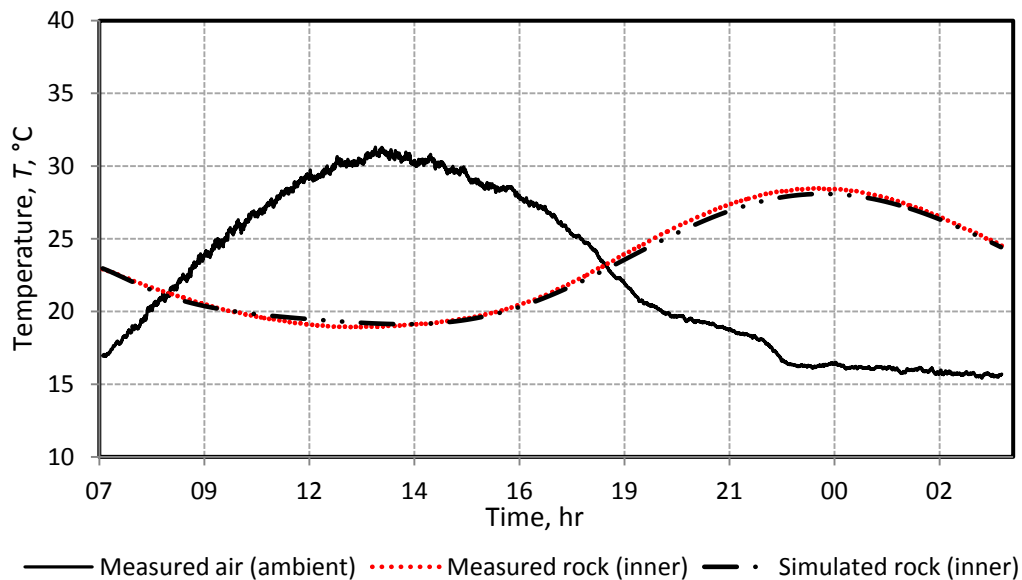
Figure 5.8: Negative forward discharge - negative forward charge of HYDROSOL – inner space, outlet

As expected, the ambient air temperature leads the rock temperature and thus causing the rock temperature to rise. As the ambient air reaches its maximum temperature just after local clock time noon it starts to decrease and drops below the rock temperature causing a delayed reaction on the rock temperature as it starts to cool down. Rock and air temperature becomes more or less the same when temperature becomes relatively constant as shown for the night time. It is interesting to note the 180° phase shift in temperature between the ambient temperature and outlet temperature. By changing mass flow rate or bed effective radius, this out of phase temperature profile can be shifted as desired. Other properties such as specific heat and density of rocks also have an effect on this.

5.2 Parametric study and system control

In order to accurately predict and control the system it is necessary to investigate the effect that different parameters have on the overall performance of the system. This includes varying particle sizes, bed void fractions, bed-lengths, packing orientations and mass flow rates through the bed. The first parameter considered

is the importance of the rock diameter and how it influences the pressure drop over the rock bed as well as thermal performance of the system. The default values considered in the parametric study are; rock density $2600\,\mathrm{kg/m^3}$, void fraction 0.4, particle size 35 mm and rock conductivity 2.1 W/mK. The study is performed assuming a forward mode of the operation with HYDROSOL apparatus dimensions as described in Section 4.1. Figure 5.9 (a) shows the average simulated pressure drop over the packed bed with linear change between cross-current and co-current orientation, for different particle sizes with markers representing data points. Constant inlet temperatures and properties are used during simulations. The velocity correction is performed by first assuming a constant air velocity over the frontal area of the rock bed at the inlet for each control volume considered. The position at the bed outlet (forward operation) resulting in the desired Biot number, is chosen and the inlet velocity of the rest of the bed corrected accordingly to result in lower Biot numbers at the rest of the outlet control volumes.

(a) $25\,\mathrm{mm} \le D_v \le 45\,\mathrm{mm}$ (b) $0.3 \le \varepsilon \le 0.4$
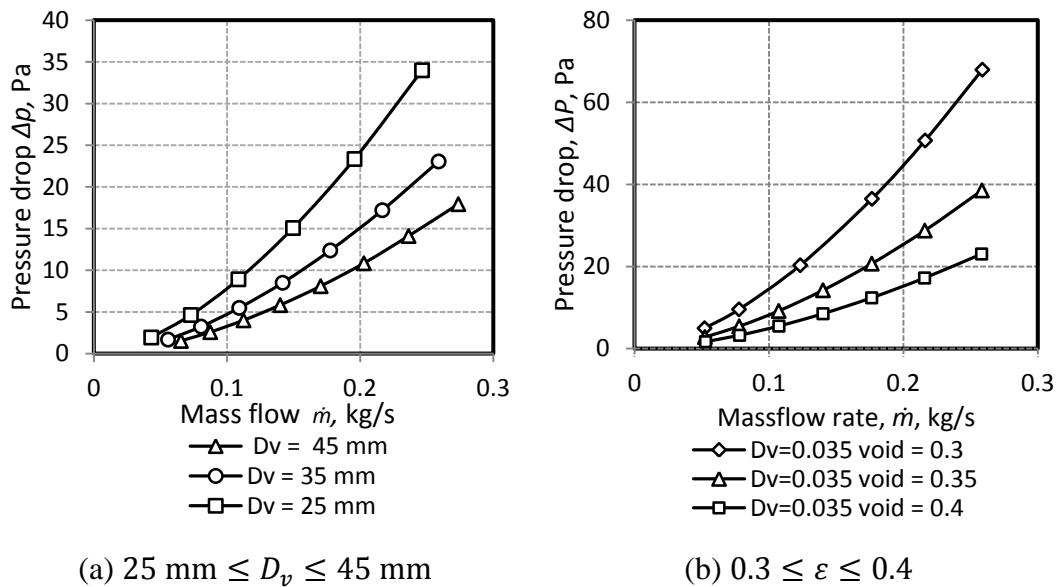
Figure 5.9: Parameter influence on pressure drop

The three particle sizes considered are 25 mm, 35 mm and 45 mm in volume equivalent diameter. It is found that the 25 mm rocks results in much higher pressure drop for different mass fluxes than the larger volume equivalent diameter rocks. This is not surprising since the smaller rocks have a larger contact surface area with air that will result in a higher frictional force as air moves over the rocks. Thus, for fan power requirements, larger rocks are more suitable since it would result in lower pressure drops.

Another important parameter influencing pressure drop is the void fraction of the rock bed. Figure 5.9 (b) shows the effect of different void fractions on the pressure drop. The void fractions considered are 0.3, 0.35 and 0.4 which is

sufficient to describe the trend on pressure drop. Typical void fractions for rock beds are in the vicinity of 0.38-0.4.

It is found that the voids between rocks influence pressure drop quite significantly and should thus be considered when selecting rocks for the system. A lower void fraction results in higher pressure drops at the same air mass flow rate through the bed. This is not surprising since the velocity have to increase through the voids as they become smaller.

Figure 5.10 considers the effect of varying parameters on the thermal performance after 3 hours of operation. Air at 20 °C enters the rock bed at the top with an effective diameter of 2 m and leaves the bed at the lower extremity of 0.5 m with the whole bed assumed to be initially at 15 °C. No losses to the environment are considered for the parametric study.

From Figure 5.10 (a) it is clear that particle size influences heat transfer capabilities of rocks at a constant mass flow rate. Smaller rocks result in lower Biot numbers at the same mass flow rate which means that higher mass flow rates can be achieved before the limiting Biot number is exceeded. A larger heat transfer surface is available leading to a steeper thermocline in the bed. A steeper thermocline means better heat exchanger efficiency and that more energy can be stored within the rock bed.

Figure 5.10 (b) illustrates the effect of fixing the Biot number to a maximum of 0.2 at the outlet for different particle sizes. The 25 mm rocks can be used at much higher mass flow rate of air before the maximum Biot number is exceeded. This means that heat can be extracted (or stored) at a much higher rate. Thus for the lumped capacitance model to be valid at higher mass flow rates, smaller rocks would be more suitable. By increasing the effective radius of the bed, the same temperature profile can be maintained at higher mass flow rates resulting in higher energy outputs.

Figure 5.10 (c) illustrates the effect of varying the mass flow rate through the rock bed having rocks of 35 mm in diameter. As expected, it can clearly be seen that an increase in mass flow rate results in faster depletion of storage. If the outlet air is required to be at 15 °C, a larger mass flow rate would result in a higher energy output for a shorter time whereas smaller mass flow rate would give a longer output temperature at 15 °C but at a lower energy rate. When designing the system, the heating and cooling requirements for worst case scenarios, should be provided from the storage at a maximum mass flow rate.

As mentioned earlier, typical rock bed void fractions are approximately 0.4 or close to it. Figure 5.10 (c) considers the effect of different void fractions on thermal behaviour. It is found that changing the void fraction does not influence the Biot number at fixed mass flow rates. This is because the Biot number is based on a superficial velocity over the face of the control volume. The velocity will however increase as it moves through smaller voids. Also smaller voids results in

bigger denser volumes with larger mass improving the heat transfer rate and forms a steeper thermocline. Thus, smaller voids would be more suitable for better thermal performance of the system but at the cost of higher pressure drops.

(a) $25\text{ mm} \leq D_v \leq 45\text{ mm}$, $\dot{m}_a = 0.15\text{ kg/s}$

(b) $25\text{ mm} \leq D_v \leq 45\text{ mm}$, $Bi = 0.2$

(c) $0.1\text{ kg/s} \leq \dot{m}_a \leq 0.15\text{ kg/s}$, $D_v = 35\text{ mm}$

(d) $0.35 \leq \varepsilon \leq 0.45$, $D_v = 35\text{ mm}$
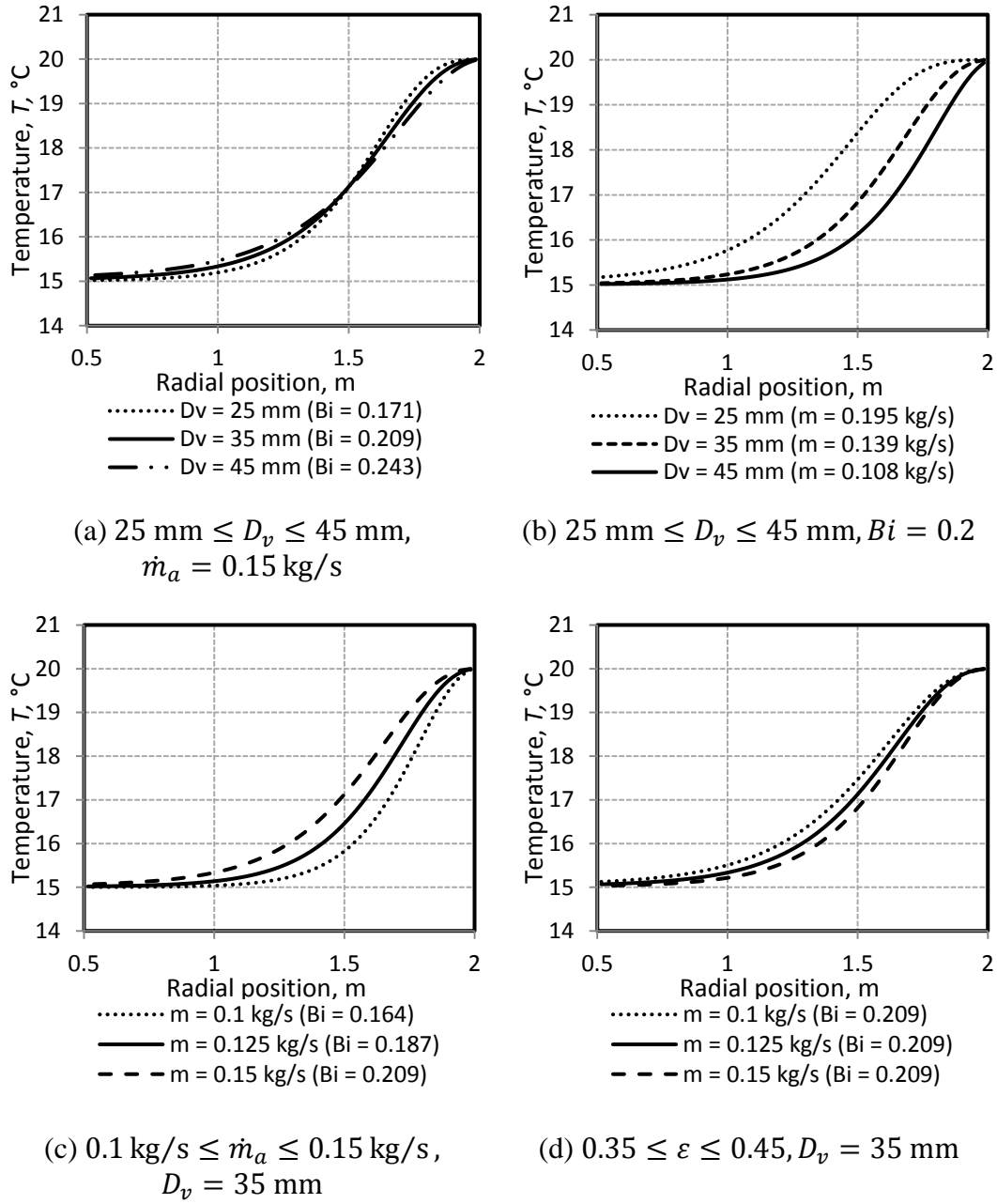
Figure 5.10: Parametric study on temperature (T_R-T_a) = 5 °C @ t = 3 hours

As mentioned earlier, a phase shift between outlet temperature and ambient temperature is found during constant operation. An ideal application where a 180° phase shift would be ideal is for the inlet air of a gas turbine. During the night cool ambient air can be used as the inlet whereas in the day, the cold outlet air from the system is to be used. In order to find the ideal out of phase temperature

profile a parametric case is presented in Figure 5.11. The simulation is performed at a fixed Biot number of $Bi = 0.2$ on a $R_{eff,i} = 0.5$ m inner radius per meter width.

Figure 5.11: Temperature profile shift

The volumetric heat capacity, $\rho_R c_{pR}$, plays an important role in shifting the temperature profile. Also by changing the physical dimensions, such as the effective outer ra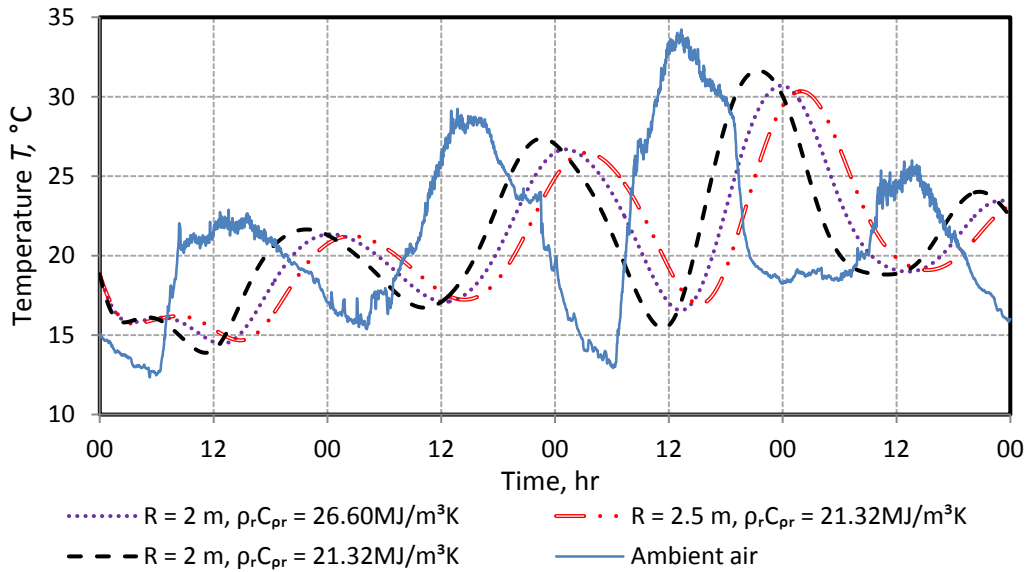dius at the same position fixed Biot number, a shift can be found. The first case is for an effective outer radius of 2 m with a volumetric heat capacity of 21.32 MJ/m^{3}K and compared to a different rock type with $\rho_R c_{pR} = 26.60$ MJ/m^{3}K at the same effective radius. It can clearly be seen that the higher capacity rocks resulted in a rightward shift in the temperature profile bringing it closer to a 180° out of phase profile.

However, rock availability and transport cost might not always be favourable for higher capacity rocks. By adjusting the effective outlet radius increasing the volume of the rock bed, the temperature profile can also be shifted to the right as shown in Figure 5.11 for an effective radius of 2.5 m and $\rho_R c_{pR} = 21.32$ MJ/m^{3}K. It is thus clear that by selecting rocks, the volumetric heat capacity need to be known in order to size the bed. Properties of various rock types can be found in Appendix B.

5.3 Control

Control of the HYDROSOL system can be achieved using two methods i.e. controlling of the air mass flow rate by changing fan speed with a variable speed drive, or by regulating and/or mixing the air with temperature controlled (or manually operated) air dampers. In order to illustrate the effect of mass flow rate

consider a bed initially at 18 °C. Air at 25 °C enters the rock bed in a forward discharge mode of operation. Figure 5.12 shows the effect that mass flow rate has on the outlet air temperature of the bed along with the energy extraction for the specific mass flow rate. Markers do not indicate data points. From Figure 5.12 (a) it can be seen that by increasing the mass flow rate, the outlet temperature would start to increase sooner. However, at higher mass flow rates the amount of heat can be extracted at a much higher rate as can be seen in Figure 5.12 (b). For lower mass flow rates, the same heat capacity is delivered over a longer period of time at a lower rate. This parametric study can be found for an actual day of cooling discharge in Appendix G. The stored energy is depleted once the whole bed is at 25 °C. The heat extracted from the bed is calculated as,

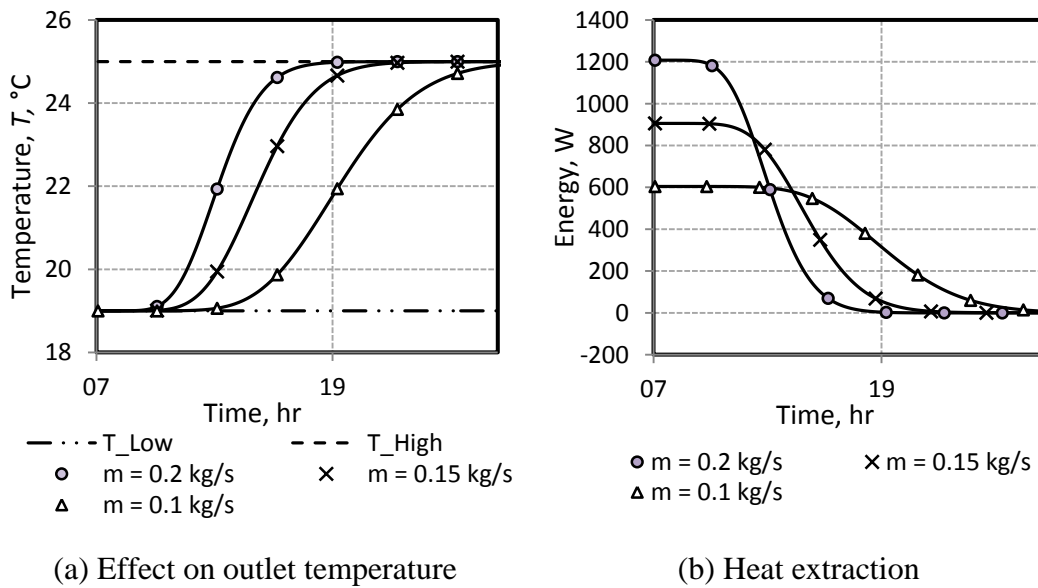$$\Delta \dot{E} = \dot{m}_a c_{p,a}(T_{a,out} - T_{a,in}) \tag{5.3}$$

(a) Effect on outlet temperature   (b) Heat extraction

Figure 5.12: Control achieved by mass flow rate @ $(T_R\text{-}T_a) = 6 \,°C$

For broiler houses, the excess heat added to the house by chickens (body heat and litter) is fairly constant during a specific time in its growth cycle as well as heat supplied by lights and feed. Solar heat and ambient temperature on the other hand will typically heat the house during the day leading to higher heat removal rate required in the broiler house during daytime (for cooling). A temperature control can be achieved by varying mass flow rate at a low Biot number in the mornings and adjust linearly or by some fixed algorithm throughout the day to ensure sufficient heat removal from the broiler house. Figure 5.13 illustrates different mass flow rate algorithms and the effect they have on the heat from storage for a typical summer's day. All illustrations are presented per meter width for a forward cooling discharge cycle of the system with an effective outer radius of $R_{eff,o} = 2$ m and inner radius of $R_{eff,i} = 0.5$ m. Maximum mass flow rate occurs at a Biot number of $Bi = 0.2$.

The first scenario is the case of constant mass flow rate at a maximum forward discharge Biot number as shown in Figure 5.13(a). The system must be designed for worst case scenarios where cooling must be supplied at maximum mass flow rate to meet the cooling loads for a specified time. It can be seen that an outlet temperature of less than 20 °C can be supplied until approximately 14:00 at a maximum heat extraction rate. Cooling, at an outlet temperature less than ambient temperature, can be supplied at 11.2 kWh per meter width of the bed. During the morning and afternoon when ambient temperatures are lower than system outlet temperatures, the ambient air would typically be used in the enclosed environment. If dry cooling provides sufficient cooling for chickens with the wind chill effect, no further cooling enhancement would be required. Further evaporative cooling is possible to lower outlet temperature further.

Maximum heat removal rate is not always necessary and mass flow rate can be adjusted linearly throughout the day to a maximum in the late afternoon as shown in Figure 5.12 (b). It is clear from the figure that the same amount of energy can be used from the stored energy but with a shift in the energy further right, to the afternoon. The cooling supplied for this mass flow variation per meter width is 10.04 kWh.

Similarly in Figure 5.12 (c) mass flow rate is varied linearly to a maximum at approximately 13:00 and kept constant thereafter. The outlet temperature for this scenario rises above 20 °C round about 15:30. Thus in order to supply a temperature lower than 20 °C for a whole day, the mass flow rate should be lowered to achieve this at a lower heat rate or a larger bed would be required to achieve this at the same mass flow rate as discussed in Section 5.2. Cooling of 10.94 kWh can be achieved.

Another scenario is illustrated in Figure 5.12 (d) where mass flow rate is increased linearly from the morning to a maximum at 13:00 and decreased linearly again to a Biot number of $Bi = 0.1$ during the afternoon. The effect of this algorithm is that energy removal occurs more gradually with maximum heat removal ability at 13:00 when mass flow rate is at its highest. Cooling of 10.18 kWh can be supplied for the day per meter width.

Consider another scenario where the bed is cold charged during a typical summer's night. Figure 5.13 (e) illustrates the mass flow rate profile required to achieve constant 700 W storage profile to be as square as possible. Thus, during the mornings when the temperature difference between inlet and outlet is low, a maximum mass flow rate is required until 700 W is achieved. As the ambient temperature increase during the day the mass flow rate from Eq.(5.3) should be adjusted accordingly as shown.

In Appendix G, more illustrations can be found where the inlet temperature of the system is fixed at a constant room temperature during the day. This would typically be the case in a used circulation cycle as described in Figure 1.8 (a). The performance effects of different set points are also presented in Appendix G.
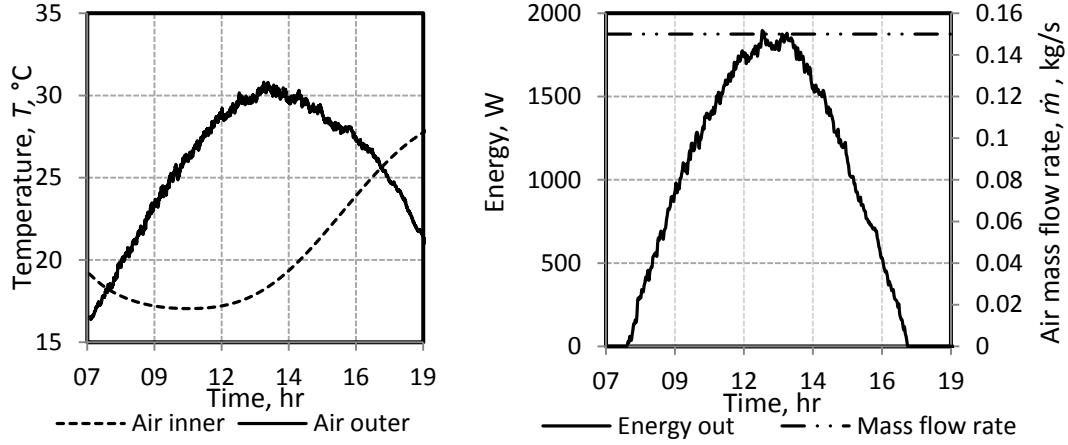
(a) Constant mass flow rate $Bi_{max} = 0.2$
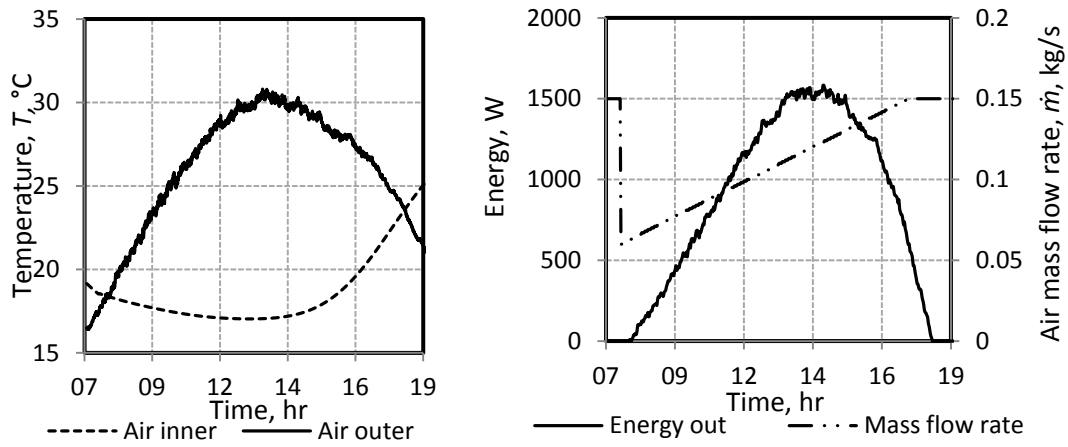
(b) Linear mass flow rate $Bi = 0.1 @ 7:30 \; to \; Bi_{max} = 0.2 @ 17:30$
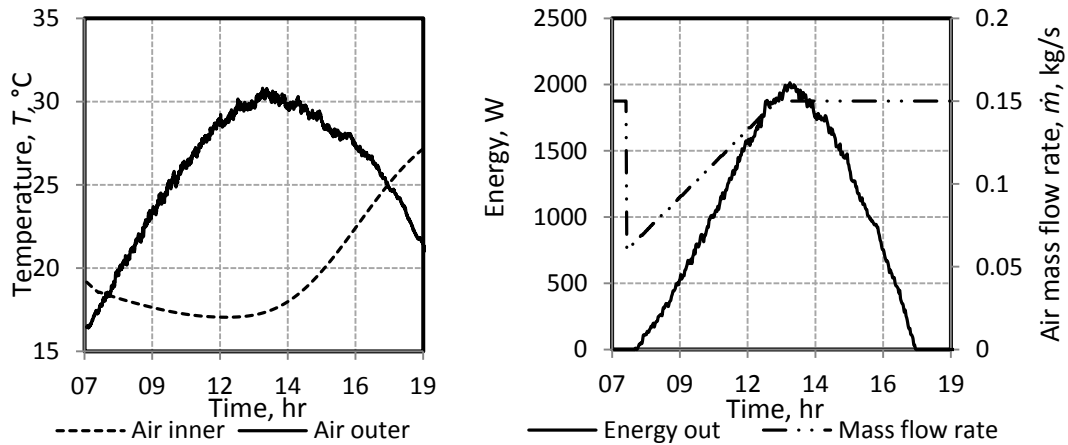
(c) Linear mass flow rate $Bi = 0.1 @ 7:30 \; to \; Bi_{max} = 0.2 @ 15:00$
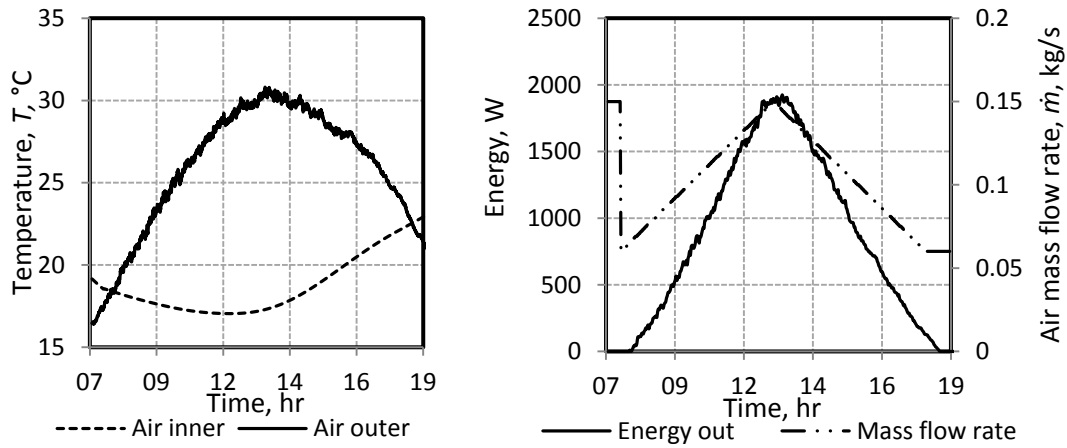
(d) Linear mass flow rate $Bi = 0.1$ @ $7{:}30$ to $Bi_{max} = 0.2$ @ $13{:}00$ to $Bi = 0.1$ @ $18{:}00$
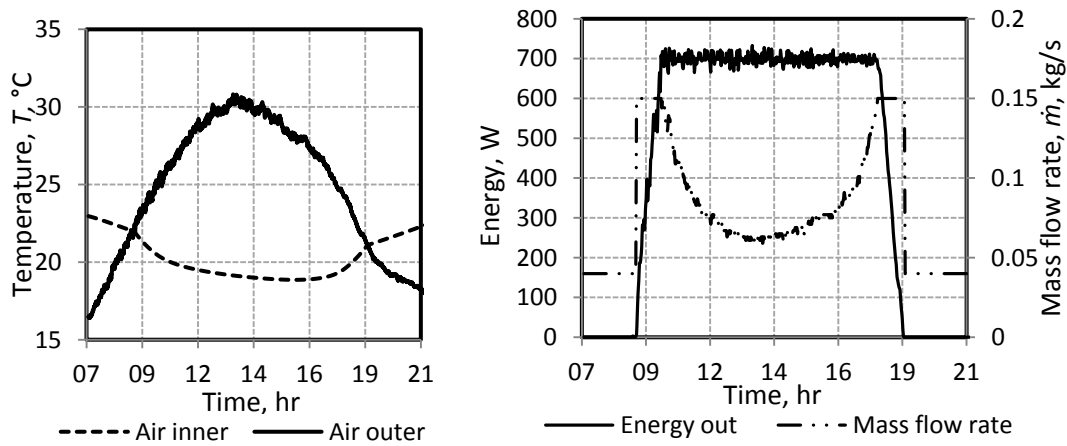
(e) Adjusting mass flow rate for 700 W $Bi_{max} = 0.2$

Figure 5.13: Air mass flow rate control on system for dry cooling

Consider Figure 5.16 that illustrates the comparison between dry-, wet and evaporative cooling, having 75 % efficiency, during a week in the summer for a system having an outer radius of 2 m and inner radius of 0.5 m. It can clearly be seen that by making use of evaporative cooling, day and night, a much lower outlet temperature can be achieved and the average temperature of the rock bed becomes much lower. However, to lower water consumption wet cooling is used where the rocks are cooled during the night using evaporative cooling while using ambient air in the enclosed environment. The extra cooling capacity can be seen in the illustration. It is clear that more cooling is achieved in the mornings, but in the afternoon the temperature rises to the same as it was with only dry cooling.

As discussed earlier, when no other rock type is a practical solution, physical dimensions can be adjusted to provide more storage capacity and control can be achieved by varying mass flow rate.

Figure 5.14: Comparison between dry-, wet- and evaporative cooling
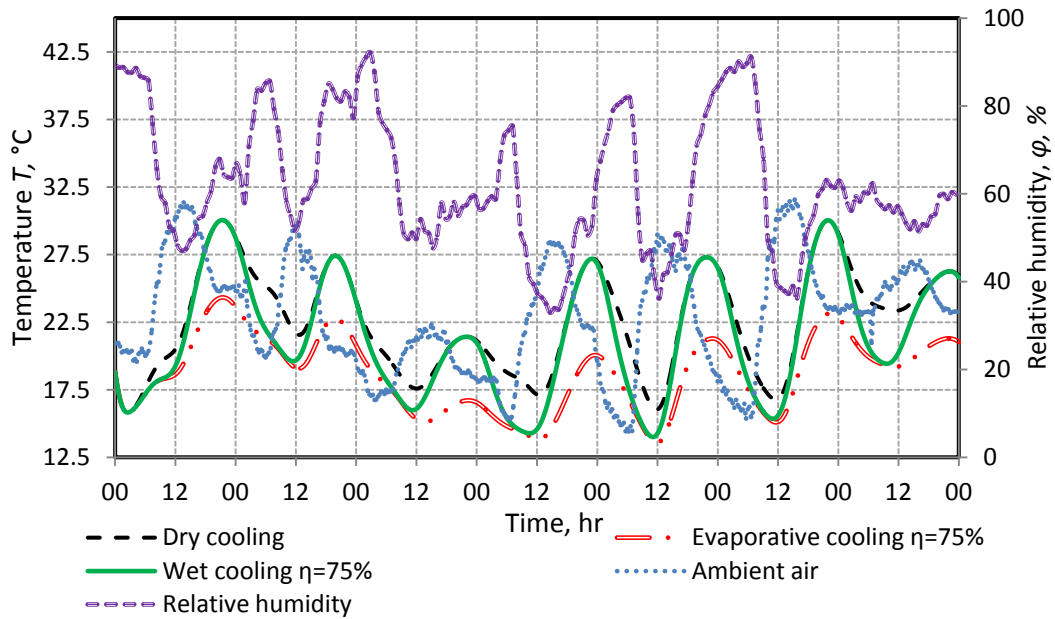
By increasing the inner radius, the fixed Biot number is based on a larger area for flow resulting in a higher mass flow rate through the system. Thus, by increasing the inner radius 50 % of the original value, results in a 50 % increase in mass flow rate of the original value to satisfy the $Bi < 0.2$ requirement for lumped capacity modelling. In order to find the same temperature profile, the outer radius should be increased so that the total volume of the rock bed is also increased by 50 %.

From Figure 5.11 it is found that by increasing the outer effective radius while keeping the inner radius constant, a shift to the right in the temperature profile occurred. However, at a constant mass flow rate, the outlet air temperature is lower during the afternoons but warmer in the mornings compared to systems having a smaller effective outer diameter. Consider Figure 5.15 illustrating the outlet temperature of a system for wet cooling operation having an outlet diameter of 2.5 m, while keeping the inner radius at 0.5 m. A step mass flow rate is compared to a constant mass flow rate. To lower the outlet temperature during the mornings, the mass flow rate during the night is increased by the step profile as shown. It can clearly be seen that the outlet temperature becomes much lower in the mornings and remains essentially the same for the afternoons. More heat is stored during the night by increasing the mass flow rate. The step in mass flow occurs when the system outlet temperature becomes higher than the inlet temperature, indicating the switch between charge and discharge.
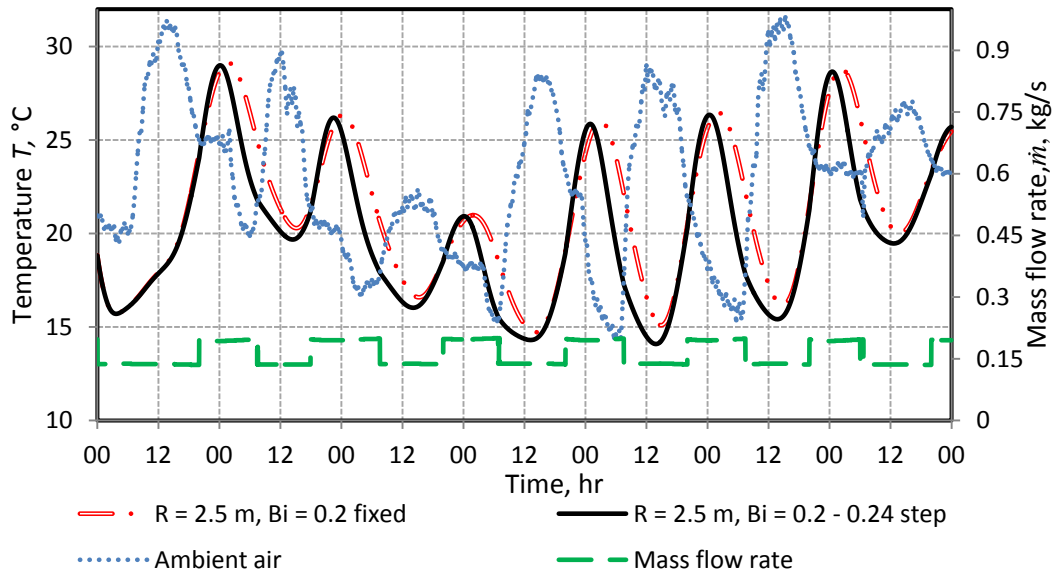
Figure 5.15: Increasing effective radius and mass flow step control

The maximum outlet temperature from the system to be used in a broiler house is approximately 25 °C. Selecting appropriate system dimensions to supply broiler houses with the right amount of mass flow in order to achieve a 6 °C wind chill effect, a maximum effective temperature experienced by the birds will be roughly 19 °C.

5.4   Suitable system design

Based on the above, it is found that broiler houses should preferably be designed according to capacity of the HYDROSOL system. For a tunnel ventilation setup, in order to provide the wind chill effect of 6 **°C** to 7 °C, consider the installation to broiler house as depicted in Figure 5.13. The rocks are dumped in a north facing container in the length of the broiler house. At the lower extremity of the bed, an air duct is situated. The duct is divided in half where the bottom part directs the outlet air for a forward discharge operation to HYDROSOL fan. The top part is used to redirect air with the air damper back to the system inlet. In order to maintain a constant pressure drop over the bed, the duct frontal area is reduced gradually to the far side of the wall. Mixing of HYDROSOL outlet air and ambient air occurs to lower the temperature and provide the wind chill effect over broilers at the required air velocity. Air is exhausted at the opposite side of the building. As the HYDROSOL system dumps unwanted air or prepares itself for the following day, ventilation is provided by the mixing fans alone to remove carbon dioxide and ammonia and provide fresh air while also cooling the birds.

Figure 5.17 illustrates the cross-sectional side view (A-A) of the concept. The roof needs to be sloped to the opposite side of the HYDROSOL to redirect rain water away from the system. The broiler house needs to be air-tight so that mass flow

75

and temperature can be controlled. Air is exhausted at the far end of the house with a wind chill established over the chicks.
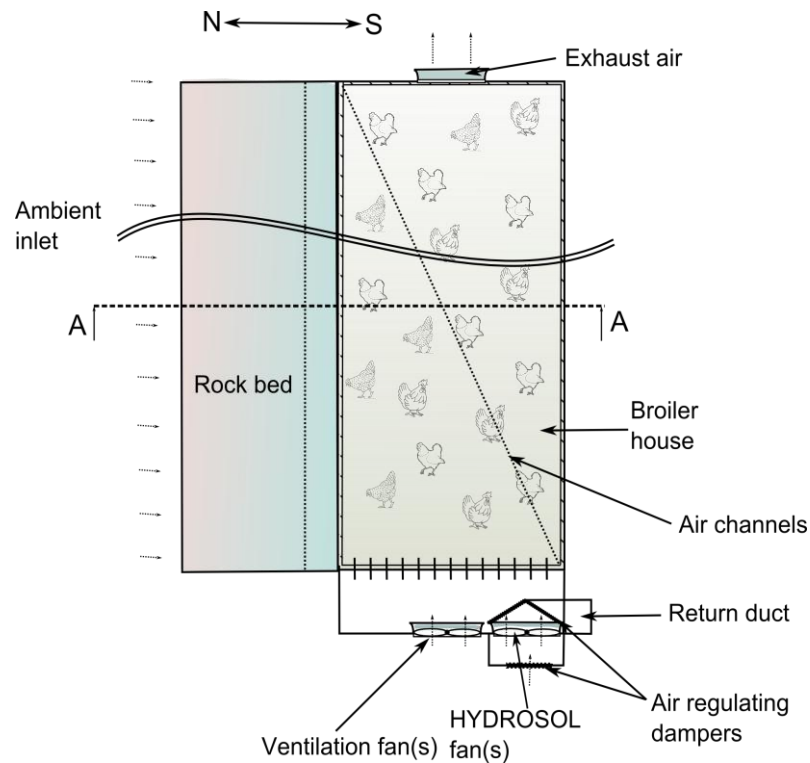

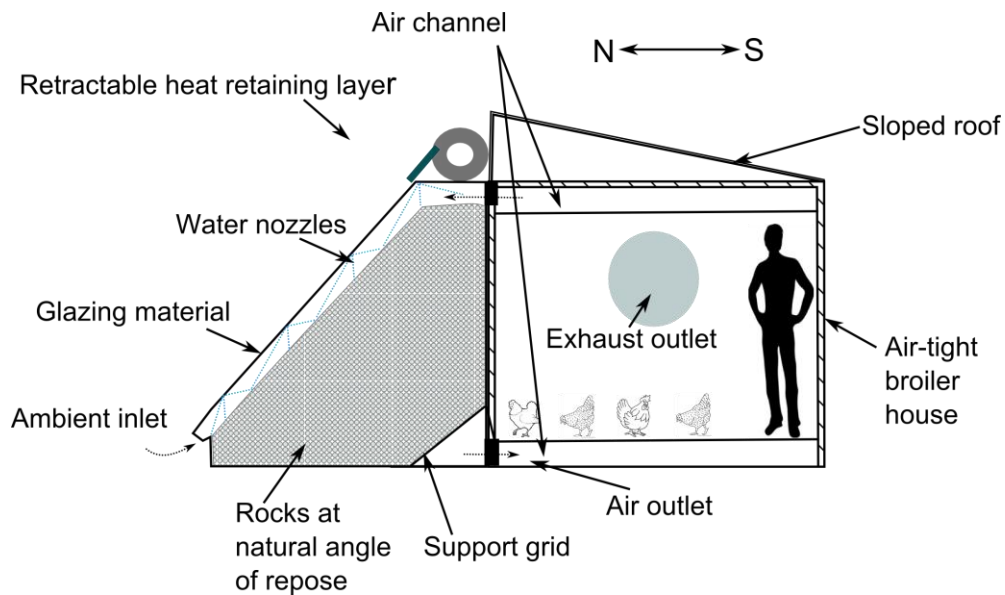**Figure 5.16: Top view: HYDROSOL system connected to broiler house (A)**

Figure 5.17: Cross sectional view (A-A): HYDROSOL system connected to broiler house (A)

76

The effective radius of the rock bed should be based on sufficient storage to operate at a maximum mass flow rate, for a specified time, required for heating or cooling. The more suitable air from either the system outlet or ambient air at the time is to be used in the broiler house.

Implementing the system in an existing broiler house, with some modifications, having typical dimensions of 120 m x 12 m x 2 m as found in Cobb (2012) would result in a required mass flow rate of approximately $\dot{m} = 57$ kg/s in order to provide a $u_a = 2$ m/s air velocity across the chicks. The HYDROSOL system with a 120 m length would be able to deliver about 28.2 kg/s at the fixed maximum Biot number at an inner radius of 0.5 m. Thus, almost half of the mass flow rate is required and can be filled up by mixing ambient air from the mixing fan. Consider a cold charged system of 20 °C and maximum, constant ambient temperature of 30 °C, will result in an outlet temperature of 25.05 °C by mixing the air from a simple energy balance. If the wind chill effect provides 5 °C additional cooling, the effective temperature experienced by chicks is about 20.05 °C (assuming no heat gain through the broiler house). The hot air inside the broiler house is flushed out of the house at the end of the building.

The problem with modifying existing tunnel ventilation broilers for cooling is that large mass flow rates of air is required to achieve a wind velocity of $u_a = 2$ m/s because of the large frontal area. In order to effectively implement the HYDROSOL system, the broiler house should be redesigned having a smaller frontal area with a greater length. Ideally, only fans from the HYDROSOL should operate to provide sufficient heat and ventilation. This can be achieved by reducing the frontal area and increasing the length of the house. Designing the house to be half of the volume mentioned earlier having the same length with 1.8 m x 6 m frontal area with the HYDROSOL at the same length and inner diameter of 0.45 m. This system would be able to provide about 26 kg/s at a maximum Biot number (based on hornfel rock properties). The wind velocity in the house would be approximately 2 m/s. The effective radius of the outer space should be determined according to heating and cooling loads, expected to be typically between 2 m to 2.5 m, to provide cooling at the outlet temperature of stored energy during the night (cooling).

During the night when system outlet temperature is unwanted, the mixing fan(s) can be used to provide the house with sufficient ventilation and heat removal while the system is prepared for the next day. Evaporative cooling can be used during the night to cold charge the bed, cooling the rocks even further. During extreme days, evaporative cooling can be directly used to lower air temperature.

Shade considerations and space availability is the main considerations for positioning other broiler houses in order to save space. The HYDROSOL system should be fixed in facing north and the broiler houses positioned according to the air channel reduction angle.

By performing a shade analysis for system installation in concept Figure 5.17 it can be seen that different units should be spaced at least 8 m from each other in order to harness solar heat from 8:00 in the mornings to about 16:00 in the afternoons during the winter months (based on Stellenbosch coordinates). This analysis is based on the extreme positions on the HYDROSOL system that causes a shade on it. The full aperture is required to receive solar heat. Figure 5.18 illustrates the basic layout with solar considerations of multiple broiler houses fitted with HYDROSOL systems

(a) Top view layout for broiler houses   (b) Side view layout for broiler houses

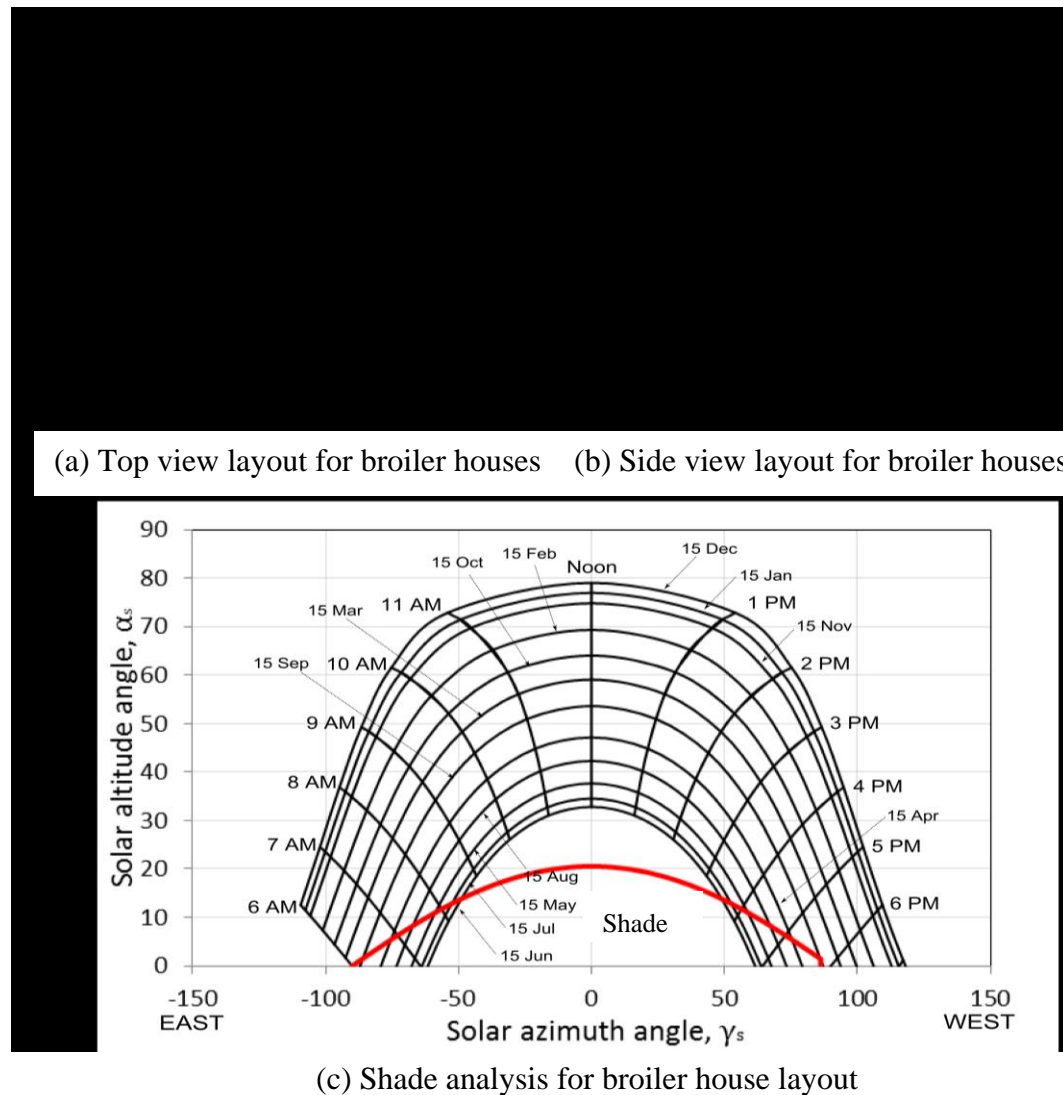(c) Shade analysis for broiler house layout

Figure 5.18: Broiler houses layout- solar considerations

Further concept development needs to address detail design of the broiler house, duct design, insulation, air mixing and distribution. Optimum broiler house design is not in the scope of this thesis. Another concept can be found in Appendix J.

5.5 Conclusion

A 2-D model for predicting temperature profiles and pressure drop in rock beds is successfully developed in Scilab. The developed model, discussed in Section 3, is found to correlate well with data obtained experimentally from the test facility described in Section 4. Pressure drop experiments are conducted by measuring the pressure drop as the mass flow rate of air is varied through the system.

The pressure drop is found to be in better agreement with the cross-current correlation proposed by Allen et al. (2013). Parameters influencing the pressure drop are considered and presented in a parametric study. It is found, as stated in the literature, that larger rock particles will result in lower pressure drops over the bed whereas smaller void fractions increase the pressure drop and thus fan power.

The parameters influencing the temperature profile from literature are investigated. It is seen that smaller rock particles results in better heat transfer rates since more surface area is exposed to air. However, by reducing the particle size, the pressure drop increases. Depending on the application for the system, best suitable particle size is based on the energy requirements and the operating cost in the long term. It is further found that smaller void fractions increase the velocity in the pores of the bed resulting in higher pressure drops but for the same volume rock, more voids would be present bringing more of the rock surface into contact with air.

By doubling the width of the bed, at the same Biot number, the mass flow rate can also be doubled. The effective outlet radius has no effect on the Biot number since this is fixed at the inner space. By increasing the outlet radius, the storage capacity increases. Similarly, by making the inner radius larger, as well as the outlet radius to get the same volume of rocks, the mass flow rate can be much higher at the same Biot number.

Different mass flow rate algorithms and the effect on outlet temperature as well as heat extraction from the storage are investigated. Typically, for cooling, the sun heats a building during the day and ambient temperatures become higher. Thus, more heat removal would be required in the afternoons than early mornings. By adjusting the mass flow rate linearly or by some other control profile, the heat removal reaches a maximum at a limiting Biot number.

A proposed broiler house design/ modification is presented for tunnel ventilation operation. Modifying existing broiler house may not be ideal since most are designed having large frontal areas for tunnel ventilation that would result in large mass flow rates to establish a wind chill effect. Ideally, broiler houses must be designed so that the mass flow rate from the rock bed, limited by the Biot number, should provide a required wind velocity to establish a wind chill effect, without having to switch on ventilation-mixing fans.

6 Conclusion and recommendations

This section provides an overall conclusion to the thesis as well as recommendations for possible further work that needs to be conducted. It should be noted that more detailed conclusions can be found at the end of each section.

6.1 Conclusion

A new sustainable space heating and cooling assembly, the HYDROSOL, that uses solar heat to provide space heating, and night ambient air /and or water to achieve cooling, is presented in this thesis. The multipurpose HYDROSOL system uses less or no water compared to conventional cooling systems specifically used for broiler houses in South Africa. Similarly, the conventional heating systems in poultry houses use fuel, electric elements or wood pellets to heat air in the environment where as the proposed system harnesses solar heat, stores it, and dispatches it as needed.

Rocks dumped in a container, allowed to form at its natural angle of repose, are the storage medium to rectify the mismatch in ambient temperatures during day and night. Rock diameter, void fraction, specific heat, and density are important factors to consider when selecting rocks for the system. Selected rocks should be fairly uniform in size and be tough so that they would not fracture and break into smaller particles since it increases pressure drop.

Site selection is based primarily on solar levels, precipitation levels, diurnal temperature as well as rock availability in the region. The price of rocks is only a small fraction of the transport cost.

A shade analysis is very important, especially for broiler houses that are lined up behind one another. Also, obstructions, such as mountains, need to be considered in order to know the exact time that a system can harness solar heat. Solar air heater theory is used in order to predict the amount of useful heat for the system available for storage.

The governing equations describing performance of the system are derived from first principles with some simplifying assumptions. A 2-D model is successfully developed in order to predict performance of the system using Scilab. Correlations used in the analysis are found to be in good agreement with measured data. However, pressure drop correlations should be determined empirically for each rock bed.

Broiler houses should be designed according to the capacity of the HYDROSOL system since space availability and shadows caused by other broiler houses on the system will be a problem. The house should be designed to have a smaller frontal area than most existing broiler houses, in tunnel ventilation configuration, to achieve a wind chill effect without mixing ambient air.

6.2   Recommendations and further work required

Further work is required in pressure drop predictions, especially for packed beds consisting of rocks. A correlation that includes all the parameters, such as rock size, shape, packing orientation, void fraction and rock type is necessary in order to eliminate the need to obtain empirical correlations for each rock bed.

A detailed cost analysis for a complete system design, installation and operation is required for specific applications. Since broiler house must be designed according to the specifications of the HYDROSOL system, the complete broiler cost should also be considered.

Evaporative cooling is an important cooling aspect of the system that needs to be investigated. Experimental data is required in order to verify numerical models in order to define water usage and evaporative cooling efficiency. Slight modifications to the existing test facility need to be incorporated.

Health risks from air quality and parameters that influence air quality must be considered. Especially with evaporative cooling where fungus and bacteria tend to grow on rocks. Appropriate water treatment, as well as preventative techniques that are not harmful, should be addressed.

A better understanding and numerical model needs to be developed for higher Biot numbers where the lumped capacitance model is not valid. Higher mass flow rates will be possible if it is possible to accurately predict the temperature profile in these higher Biot number ranges.

Detailed duct design and air distribution in broiler houses along with appropriate air dampers will have to be considered and designed for practical implementation. This along with appropriate PLC control is necessary to fully automate the system.

More detailed heating and cooling loads for a specific broiler house for HYDROSOL implementation is required in order to fully specify the control algorithms. Making use of weather predictions would be beneficial since system preparation needs to happen ahead of time.

A CFD model for flow through the packed bed as well as broiler house air temperature and flow distribution is required for better understanding of the flow patterns and air distribution.

Suggested improvements in the test facility would be to include a reversible fan to easily reverse flow direction. Better insulation to pipes should to be considered. It would definitely be beneficial to add more thermocouples at various positions in the bed in order to better understand the flow through bed.

7 References

Abdel-Salam, M., Aly, S., El-Sharkawy, A. & Abdel-Rehim, Z., 1991. Thermal characteristics of packed bed storage system. *International journal of energy research,* Volume 15, pp. 19-29.

Abdel-Wahed, R., Emerson, P., Blackshear, P. & Riaz, M., 1979. *Effects of thermal storage efficiencies of modifying heat-transport properties of indigenous sandstones.* Chicago, Pergamon.

Alkilani, M. M. et al., 2011. Review of solar air collectors with thermal storage units. *Renewable and sustainable Energy Reviews,* Volume 15, pp. 1476-1490.

Allen, K., 2010. *Performance characteristics of packed bed thermal energy storage for solar power plants, MScEng thesis,* s.l.: University of Stellenbosch.

Allen, K., von Backström, T. & Kröger, D., 2013. Packed bed pressure drop dependence on particle shape, size distribution, packing arrangement and roughness. *Powder Technology,* Volume 246, pp. 590-600.

Anderson, N., 2014. *Evaluation of the performance charcteristics of a hybrid (dry/wet) induced draft dephegmator,* Stellenbosch: Stellenbosch University.

Barton, N., 2013. Simulations of air-blown thermal storage in a rock bed. *Applied thermal Engineering,* Volume 55, pp. 43-50.

Carman, P., 1937. Fluid flow through granular beds. *Transactions of the institute of chemical engineers (London),* Volume 15, pp. 150-166.

Chandra, P. & Willits, D., 1981. Pressure drop and heat transfer characteristics of air-rockbed thermal storage systems. *Solar Energy,* Volume 6, pp. 547-553.

Cobb, 2012. *Broiler management guide.* s.l.:s.n.

Department of Energy, 2009. *Clean Energy,* Pretoria: Department: Energy Republic of South Africa.

Duffie, J. & Beckmann, W., 1991. *Solar engineering of thermal processes.* 3rd ed. New York: Wiley.

Eckhof, S. & Okos, M., 1978. *Solar energy heat storage for home,farm and small business: Sugestions on selecting and using thermal storage materials and facilities,* Indianapolis: Purdue University.

Fawaz, H., Abiad, M. G., Ghaddar, N. & Ghali, K., 2013. Solar-assisted localized ventilation system for poultry brooding. *Energy and Buildings,* Volume 71, pp. 142-154.

Furnas, C., 1929. Heat transfer from a gas stream to a bed of broken solids. *Industrial engineering and chemistry,* Volume 22, pp. 26-31.

Heaton, H., Reynolds, W. & Kays, W., 1964. Heat transfer in annular passages. Simulataneous development of velocity and temperature fields in laminar flow. *Heat Mass transfer,* Volume 7, pp. 763-781.

Hughes, P., Klein, S. & Close, D., 1976. Packed bed thermal storage models for solar air heating and cooling systems. *Journal of heat transfer,* Volume 98, pp. 336-338.

J.N. Rohwer, 2013. *One dimensional numerical model of a HYDROSOL thermal rockbed storage system, Final year report,* Stellenbosch: Stellenbosch University.

Jalalzadeh-Azar, A., Steele, W. & Adebiyi, G., 1996. Heat transfer in a High-Temperature packed bed thermal energy storage syste-Roles of radiation andintrparticle conduction. *Journal of energy resources technology,* Volume 18, pp. 50-57.

Jefferson, C., 1972. Preciction of breakthrough curves in packed beds.. *American institute of chemical enigineers journal (AIChE),* Volume 18, pp. 409-420.

Kalogirou, S. A., 2009. *Solar energy engineering: Process and Systems.* 1st ed. Amsterdam: Elserivier inc.

Kentucky, U. o., 2005. *Kentucky poultry energy efficient project.* [Online] Available   at: http://www2.ca.uky.edu/poultryprofitability/production_manual.html   [Accessed 2014].

King, R. & Burns, A., 1981. *Sensible heat storage in packed beds.* Brighton, International conference on energy storage. Paper N1, pp.231-245.

Kröger, D.G., 2004. *Air-Cooled Heat Exchangers and cooling Towers.* Tulsa,Oklahoma: Penwell Corporation.

Liu, B. & Jordan, R., 1963. The long term average performance of flat-plate solar energy collectors. *Solar Energy,* Volume 7, p. 53.

Löff, G. & Hawley, R., 1948. Unsteady-state heat transferbetween air and loose solids. *Industrial Engineering and Chemistry,* Volume 40, pp. 1061-1070.

Macdonald, I., El-Sayed, S., Mow, K. & Dullien, F., 1979. Flow through porous media-the Ergun revisited. *Department of chemical engineering,* Volume 18, pp. 199-208.

Martin, H., 2005. *The Levêque-analogy or how to predict heat and mass transfer from fluid friction.* Cairo, HEFAT2005 4th international conference on heat transfer, fluid mechanics and thermodynamics.

McAdams, W., 1954. *Heat Transmission.* 3rd ed. New York: McGraw-Hill.

Meyer, A. J. & van Niekerk, J. L., 2012. Roadmap for the deployment of concentrating solar power in South Africa.

Nemec, D. & Levec, J., 2005. Flow through packed reactors:1. Single- phase flow. *Chemical Engineering Science,* Volume 60, pp. 6947-6957.

Pascal Coutier, J. & Farber, E., 1982. Two applications of a numerical approach of heat transfer process within rock beds. *Solar Energy,* Volume 29, pp. 451-462.

Prieur du Plessis, J. & Woudberg, S., 2008. Pore-scale derivation of the Ergun equation to enhance its adaptability and generalization. *Chemical engineering sciences,* Volume 63, pp. 2576-2586.

Ramadan, M., El-Sebaii, A., Aboul-Enein, S. & El-Bialy, E., 2007. Thermal performance of a packed bed double-pass solar air heater. *Energy,* Volume 32, pp. 1524-1535.

Rohwer, J., 2013. *One dimensional numerical model of a HYDROSOL thermal rockbed storage system,* Stellenbosch: Stellenbosch University.

Ross, 2010. *Environmental management in the broiler house.* s.l.:s.n.

Schumann, T. E. W., 1929. Heat transfer: a liquid flowing through a porous prism. *Journal of the Franklin Institute,* Volume 208, pp. 405-416.

Shitzer, A. & Levy, M., 1983. Transient behaviour of a rock-bed thermal storage systems subjected to variable inlet air temperature: Analysis and experimentation. *Journal of solar engineering,* Volume 105, pp. 200-206.

Singh, R., Saini, R. & Saini, J., 2006. Nusselt number and friction factor correlations for a packed bed solar energy storage system having larged size elements of different shapes. *Solar Energy,* Volume 80, pp. 760-771.

Stine, W. & Geyer, M., n.d. *Power from the sun.NET.* [Online]Available at: http://www.powerfromthesun.net/[Accessed 2013].

TradeKorea, 2014. *TradeKorea.com.* [Online] Available at: http://www.tradekorea.com/product/detail/P390447/Evaporative-cooling-system.html[Accessed 09 10 2014].

Wakao , N., Kaguei, S. & Funazkri, T., 1978. Effect of fluid dispersion coefficients on particle-to-fluid heat transfer coefficients in packed beds. *Chemical engineering science,* Volume 34, pp. 325-336.

Waked, A. M., 1986. Solar energy storage in rocks. *Solar and wind technology,* Volume 3, pp. 27-31.

Waples, D. & Waples, J., 2004. A review and evaluation of specific heat capacities of rocks, mineral and subsurfaces fluids. *Natural Resources Research,* Volume 13, pp. 97-122.

Appendix A: Correlations convective heat transfer coefficients and pressure drop

A.1: Pressure drop

The semi empirical Ergun (1952) equation to predict pressure drop over packed beds is given by;

$$-\frac{\Delta p}{L} = A\frac{(1-\varepsilon)^2}{\varepsilon^3}\frac{\mu u_s}{D_h} + B\frac{(1-\varepsilon)}{\varepsilon^3}\frac{\rho u_s^2}{D_h} \tag{A.1}$$

where constants A and B are 150 and 1.75 for the original Ergun equation with improvements proposed by Macdonald et al. (1979) in Table A.1. u_s is the superficial velocity of air and D_h is defined as the particle size in terms of particle volume and surface area;

$$D_h = \frac{6\sum V_p}{\sum A_p} \tag{A.2}$$

The Ergun Reynolds number is defined in terms of the superficial velocity, u_s and particle size D_h as;

$$Re_{Er} = \frac{\rho u_s D_h}{\mu(1-\varepsilon)} \tag{A.3}$$

where ρ and μ are the density and viscosity of the fluid respectively. The void fraction, ε, can be defined as the fraction of void volume to the total volume of the bed and can be expressed as:

$$\varepsilon = \frac{V_v}{V_{tot}} \tag{A.4}$$

Table A.1: Ergun constants proposed by Macdonald et al. (1979)

Type of particle	A	B
Gravel (110 mm)	841	1.01
Sand (0.46 mm)	179	2.52
Smooth marbles (29 mm)	546	1.14

The correlation proposed by Singh et al. (2006) also includes a sphericity factor;

$$f_s = 4.466(Re_p)^{-0.2}\Psi^{0.696}(\varepsilon)^{-2.945}[\exp\{11.85(log\ \Psi)^2\}] \tag{A.5}$$

valid for $1000 < Re_p < 2700$, where Ψ is the sphericity factor is calculated as;

$$\Psi = \frac{A_s}{A_p} \tag{A.6}$$

where A_s is the surface area of an irregular shaped particle considered as a sphere.

Nemec and Levec (2005) also included a sphericity factor and presents a correlation based on the Ergun Reynolds number as;

$$f_{NL} = \frac{150}{\Psi^{3/2} Re_{Erg}} + \frac{1.75}{\Psi^{4/3}} \tag{A.7}$$

Valid for $Re_{Erg} < 400$

Allen et al. (2013) presents correlations for a counter- current packing and a cross current packing respectively as a frictional force experienced by the flowing air as;

$$f_v = \frac{\Delta p}{L(\rho u_s^2/2)} \frac{\varepsilon^3}{(1-\varepsilon)} D_v \approx 76.47 \left(\frac{1-\varepsilon}{Re_{pv}} \right)^{0.343} \tag{A.8}$$

valid for $0.38 < \varepsilon < 0.45$ and $0.009 \text{ m} < D_v < 0.045 \text{ m}$ and $50 < Re_{pv} < 400$ where D_v is determined from Eq. (2.10) and Re_{pv} from Eq.(2.16).

$$f_v = \frac{\Delta p}{L(\rho u_s^2/2)} \frac{\varepsilon^3}{(1-\varepsilon)} D_v \approx 80.94 \left(\frac{1-\varepsilon}{Re_{pv}} \right)^{0.41} \tag{A.9}$$

valid for $0.38 < \varepsilon < 0.45$ and $0.009 \text{ m} < D_v < 0.029 \text{ m}$ and $50 < Re_{pv} < 400$.

where D_v is the volume equivalent diameter of the rocks, ε is the void fraction of the bed and Re_{pv} the particle Reynolds number.

A.2:   Heat transfer models and correlations

The Schumann (1929) model, as derived for axial flow through a cylinder divided in segments of Δx and air at temperature T_a flowing in over rocks of temperature T_R having a velocity of v_s, is considered. The Schumann assumptions are: infinite conductivity in the radial direction, no temperature gradient within the rocks, no axial thermal dispersion, no mass transfer occurs and no heat losses to surrounding environment. The model to predict thermal behaviour of the air is given as;

$$\frac{\partial T_a}{\partial t} = -v_s \frac{\partial T_a}{\partial x} - \frac{h_c a_{Ri}}{\varepsilon c_{pa} \rho_a} (T_a - T_R) \tag{A.10}$$

and the rock temperature is found from;

A.2

$$\frac{\partial T_R}{\partial t} = \frac{h_c a_{Ri}}{(1-\varepsilon)c_{v,R}\rho_R}(T_a - T_R) \tag{A.11}$$

Hughes (1979) assumed negligible thermal capacitance of air and derived an extension to the Schumann (1929) model to obtain the effectiveness-NTU model with losses to surroundings included;

$$\frac{\partial T_a}{\partial x} = \frac{NTU}{L}(T_R - T_a) + \frac{UP}{\dot{m}_a c_{pa}}(T_{env} - T_a) \tag{A.12}$$

And for the solid temperature;

$$\frac{dT_a}{dt} = \frac{L}{\Delta x}\frac{\dot{m}_a c_{p,a}}{m_R c_{v,R}}(T_a - T_R)\left(1 - e^{-NTU\left(\frac{\Delta x}{L}\right)}\right) \tag{A.13}$$

Jefferson (1972) replaces the original *NTU* with *NTU$_c$* that is corrected for particle adjustment as;

$$NTU_c = NTU/(1 + Bi/5) \tag{A.14}$$

The dimensional convective volumetric heat transfer coefficient proposed by Löff and Hawley is written as;

$$h_v = 652\left(\frac{G}{D_h}\right)^{0.7} \tag{A.15}$$

The correlation of Chandra and Willits (1981) based on tests from rock beds;

$$h_v D^2/k_f = 1.45 Re_p^{0.7} \tag{A.16}$$

Valid for $100 < Re_p < 1000$.

Pascal Coutier and Farber (1982) propose a correlation for volumetric heat transfer coefficient as;

$$h_v = 700\left(\frac{G}{D}\right)^{0.75} \tag{A.17}$$

Wakao et al. (1978) propose a correlation corrected for thermal dispersion as;

$$Nu = \frac{hD}{k_a} = 2 + 1.1 Pr^{1/3} Re_p^{0.7} \tag{A.18}$$

Martin (2005) gives a correlation based on the definition of the Hagen, *Ha,* number as;

$$Nu/Pr^{\frac{1}{3}} = 0.4038\left(2x_f Hg d_h/L_f\right)^{1/3} \tag{A.19}$$

A.3

where L_f is defined as;

$$L_f = D/(1 - \varepsilon)^{1/3} \qquad\qquad (A.20)$$

and the hydraulic diameter, D_h, calculated as;

$$\frac{D_h}{L_f} = \frac{(2/3)\varepsilon}{(1 - \varepsilon)^{2/3}} \qquad\qquad (A.21)$$

The Hagen equation is;

$$Hg = Re_p\big[150(1 - \varepsilon) + 1.75Re_p\big](1 - \varepsilon)/\varepsilon \qquad\qquad (A.22)$$

Values for the frictional fraction of the total pressure drop are 0.197 for a cube and 0.447 for a sphere and differently shaped particles should fall between the ranges (Allen, 2010).

Appendix B: Rock properties

The density of the rocks is measured by weighing a random rock batch sample and measuring the displacement of water in a cylindrical measuring tube. Rock density is found by taking the average of the mass samples divided by its volume displacement.
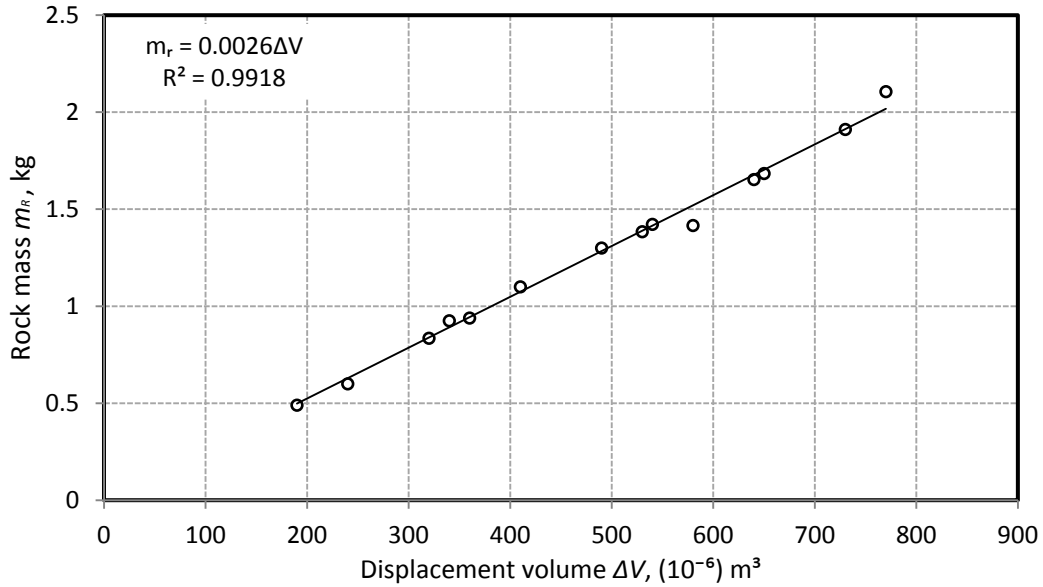

Figure B.1: Water volume displacement for added rocks

The average rock density is found to be approximately 2591 kg/m^3 for the selected hornfel rock type located near Durbanville in the Western Cape.

Similarly, By knowing the quantity of rocks, n, per sample, the volume equivalent diameter is found to be 35,2 mm using Eq.(B.1);

$$D_v = \left[\frac{6}{\pi} \left(\frac{1}{n} \sum_{i=1}^{n} V_{pi} \right) \right]^{1/3} \tag{B.1}$$

The mass of the rock samples is measured with a Nagata FAT 12 scale with a rated uncertainty of $2(10^{-3})$ kg.

The specific heat of the rocks from Waples and Waples (2004);

$$c_p = -0.00129 T_R^2 + 1.518 T_R + 748 \tag{B.2}$$

where T_R is the rock temperature in degrees Celsius resulting in a specific heat with units, J/kgK

Thermal conductivity of hornfel rocks, $k_R = 2.9 W/mK$ (British Geological Survey, s.a.)

Table B.1: Properties of various rock types (Allen, 2013)

Rock type	ρ_R kg/m³	$c_{pR @ 20°C}$ J/kgK	$\rho_{pR}c_{pR}$, MJ/m³K
Amphibolite	3010	700	2.11
Amphibolite	3010	1134	3.41
Basalt	2870	898	2.58
Clay	2680	860	2.30
Diabase	2790	731	2.04
Diabase	2790	860	2.40
Diorite	2870	1140	3.27
Dolerite	2900	900	2.61
Gabbro	3000	650	1.95
Gneiss	2700	770	2.08
Gneiss	2700	979	2.64
Granite	2650	600	1.59
Granite	2620	1172	3.07
Granodiorite	2840	650	1.85
Granodiorite	2730	1046	2.86
Limestone	2770	680	1.88
Limestone	2760	880	2.43
Marble	2760	883	2.44
Quartzite	2640	731	1.93
Quartzite	2640	1013	2.67
Sandstone	2640	775	2.05
Schist	2770	790	2.19
Schist	2900	1096	3.18
Slate	2780	740	2.06
Slate	2770	1113	3.08
Tuff	2690	795	2.14
Tuff	2750	1090	3.00

Appendix C: Calibrations

All instruments used in the experiments are calibrated beforehand, while some instruments had to be calibrated on a regular basis, such as the pressure transducers.

C.1:   Thermocouples

The T-type (copper- constantan) thermocouples are connected to an Agilent data card and calibrated with a FLUKE 9142 Field Metrology Well. The card was never removed from the Agilent data logger after calibration. A Platinum Resistance Temperature Detector (PRTD) is used as the reference thermocouple to which the other thermocouples are calibrated to. The FLUKE is set to 0 °C and increased in steps of 10 °C to 60 °C. For each set temperature, the FLUKE is allowed to stabilize for at least 7 minutes and then 20 minutes for each set reference point while logging data for each thermocouple every 10 seconds. An average reading for each thermocouple over the 20 minutes is used. The kOhm output (Ω_{ref}) from the calibrated PRTD is converted to temperature by;

$$T_{ref} = 0.00111611\Omega_{ref}^2 + 2.32652102\Omega_{ref} - 243.7648049 \qquad \text{(C.1)}$$

Four the measured average values for four thermocouples along with the reference temperature and Fluke set point are shown in Table C.2. The FLUKE only allowed four thermocouples to be calibrated at a time, so the procedure had to be repeated for all thermocouples.

Table C.2: Reference temperature compared to raw thermocouple readings

| Set point [°C]	kOhm reading [kΩ]	Reference Temperature [°C]	T_1 [°C]	T_2 [°C]	T_3 [°C]	T_4 [°C]
0	100.07	0.2269	0.516259	0.693444	0.607815	0.636852
10	103.949	10.1347	10.08217	10.16867	10.10511	10.11178
20	107.819	20.0531	19.92748	19.95014	19.88622	19.88143
30	111.689	30.0048	29.88681	29.87981	29.82442	29.81754
40	115.563	40.0004	40.08872	40.07744	40.02894	40.02756
50	119.421	49.9879	50.36165	50.3373	50.28905	50.28965
60	123.251	59.9359	60.74968	60.71595	60.69153	60.68374

The four thermocouples considered in the table are plotted in Figure C.1 with along with the PRTD temperature for a set point on the FLUKE.
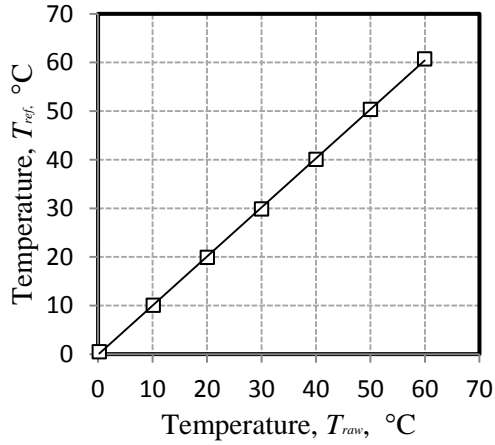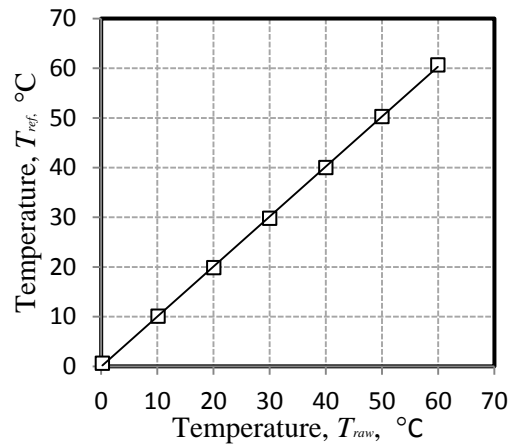
(a) Calibration fit for T_1
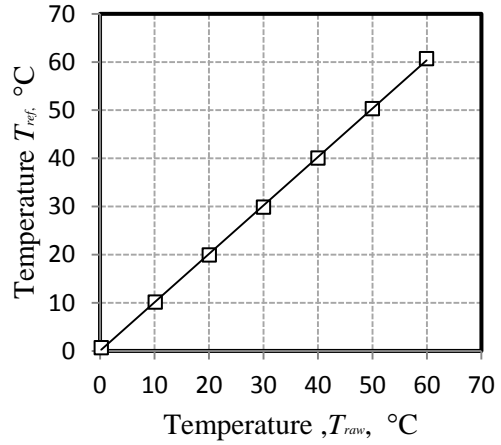
(b) Calibration fit for T_2
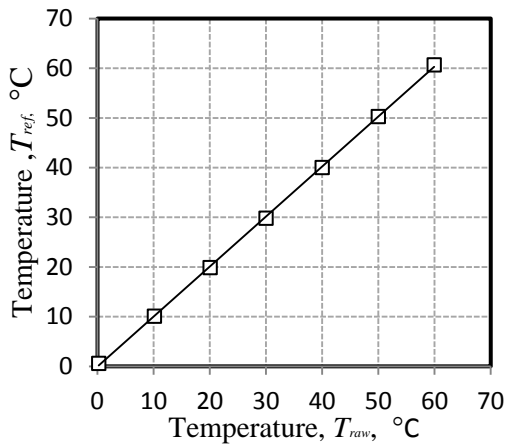
(c) The curve fit for T_3

(d) The curve fit for T_4

Figure C.1: Thermocouple calibration

A linear curve fit to the data for the four thermocouples is applied and the calibrated values from the raw data measurements can be found accordingly;

$$T_{1,cal} = 1.0095 T_{1,raw} - 0.1038 \tag{C.2}$$

$$T_{2,cal} = 1.0063 T_{2,raw} + 0.0219 \tag{C.3}$$

$$T_{3,cal} = 1.0071 T_{3,raw} - 0.0585 \tag{C.4}$$

$$T_{4,cal} = 1.0067 T_{4,raw} - 0.0435 \tag{C.5}$$
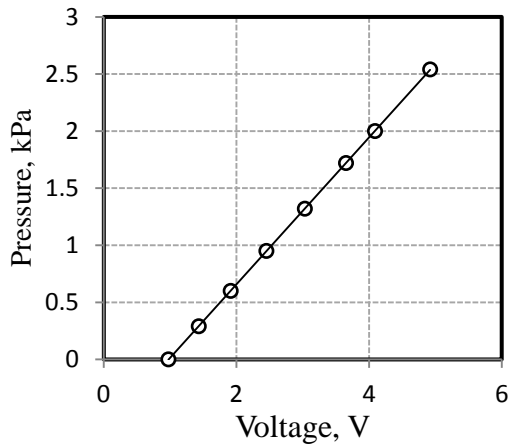
C.2: Pressure transducers

A total of three Endress & Hauser pressure transducers are calibrated at least once a month. The transducers are connected to the Agilent data logger and measures a output voltage (0 V – 5 V) for ranges 0 kPa – 2.5 kPa for two of the transducers

while the third in the same pressure ranges give an output of 0 V- 10 V. A Betz manometer that measures mmH$_2$O is used as the reference pressure. The Betz is tuned to zero with both positive and negative ports open to atmospheric pressure. The three transducers are connected in series with the negative port going into the positive port of the other. The negative port of the last transducer is connected to the negative port of the Betz. By blowing into the positive port and blocking the port, a reference value on the Betz is manually taken while logging the output voltages of the transducers. Some air is allowed to escape and a new set of data is logged. This is repeated until no more air trapped is in the network. Figure C.2 shows the plots of measured voltages and reference pressures for the three transducers.
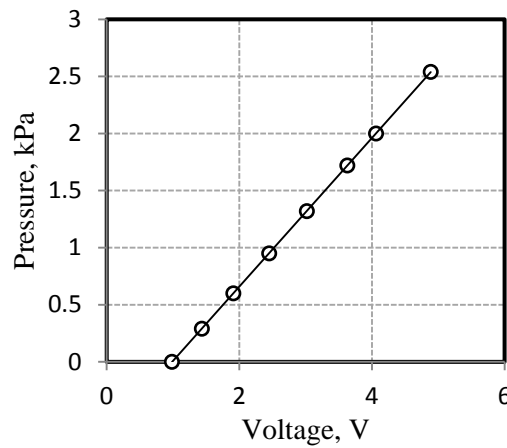
(a) Calibration fit for p_A

(b) Calibration fit for p_B
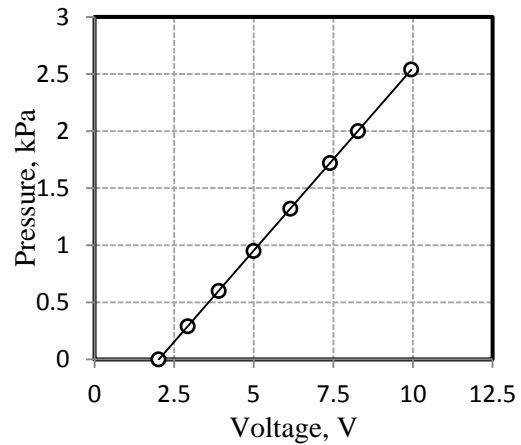
(c) Calibration fit for p_C

Figure C.2: Pressure transducers calibration

A linear curve fit to the data for the three pressure transducers is applied and the calibrated values from the raw data measurements can be found accordingly;

$$p_A = 0.6513V - 0.6444 \tag{C.6}$$

C.3

$$p_B = 0.6438V - 0.63 \tag{C.7}$$

$$p_C = 0.3201V - 0.6463 \tag{C.8}$$

C.3: Venturi

The venturi, constructed from two 110mm to 75 mm PVC reductions is connected to the wind tunnel setup as depicted in Figure C.3.
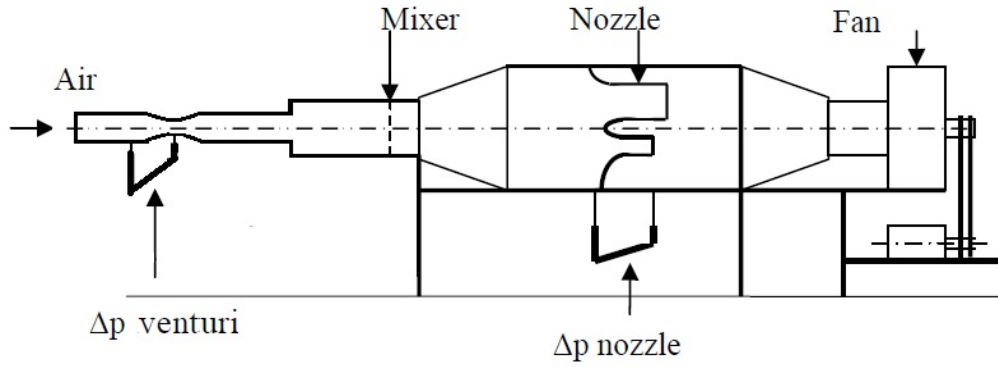

Figure C.3: Venturi calibration wind tunnel setup

The venturi is calibrated by connecting it to the wind tunnel setup consisting of mixing vanes and a settling chamber in which nozzles are located. The available nozzles in the tunnel are 50 mm, 75 mm, 150 mm, 200 mm and 250 mm. The pressure drop over this nozzle is converted to mass flow rate as presented by Kröger (2004) as;

$$\dot{m}_a = C_n \phi_g Y A_n (2\rho_n \Delta p_n)^{0.5} \tag{C.9}$$

where A_n is the cross sectional area of the nozzle in the setting chamber, ρ_n is the density at the nozzle temperature and pressure, Δp_n is the measured pressure drop over the nozzle, ϕ_g is the gas expansion factor, Y the approach velocity factor and C_n the discharge coefficient of the nozzle.

C_n is defined as;

$$C_n = 0.954803 + 6.37817(10^{-7})Re_n - 4.65394(10^{-12})Re_n^2 \\ + 1.33514(10^{-17})Re_n^3 \tag{C.10}$$

for $30000 < Re_n < 100000$ and

$$C_n = 0.9758 + 1.08(10^{-7})Re_n - 1.6(10^{-13})Re_n^2 \tag{C.11}$$

for $100000 < Re_n < 350000$ and

$$C_n = 0.994 \tag{C.12}$$

for $Re_n > 350000$

The Reynolds number over the nozzle can be found with;

$$Re_n = \frac{\rho_n u_n D_n}{\mu_n} \tag{C.13}$$

With D_n the nozzle diameter, u_n the velocity of the air in the nozzle, and μ_n the viscosity of air in the nozzle.

The approach velocity factor is found with;

$$Y = 1 + 05\left(\frac{A_n}{A_{tus}}\right)^2 + 2\left(\frac{A_n}{A_{tus}}\right)^2 \frac{\Delta p_n}{\left(p_{up} c_{pa}/c_{va}\right)} \tag{C.14}$$

With A_{tus}, the upstream cross sectional area before the nozzles which for the specific wind tunnel is 1.44 m^2. The cross sectional area of the nozzle (A_n) used is 0.001963 m^2.

The gas expansion factor is found from;

$$\phi_g = 1 - \frac{3\Delta p_n}{4 p_{up} c_{pa}/c_{va}} \tag{C.15}$$

where p_n is the pressure measured upstream from the nozzle. The ratio c_{pa}/c_{va} for air may be taken as 1.4.

In the setup, the air mass flow rate is varied from 0 kg/s to approximately 0.22 kg/s while converting to mass flow rate from the nozzle pressure drop. The venturi is calibrated by curve fitting the pressure drops measured over the venturi and the converted mass flow rate and shown in Figure C.4.
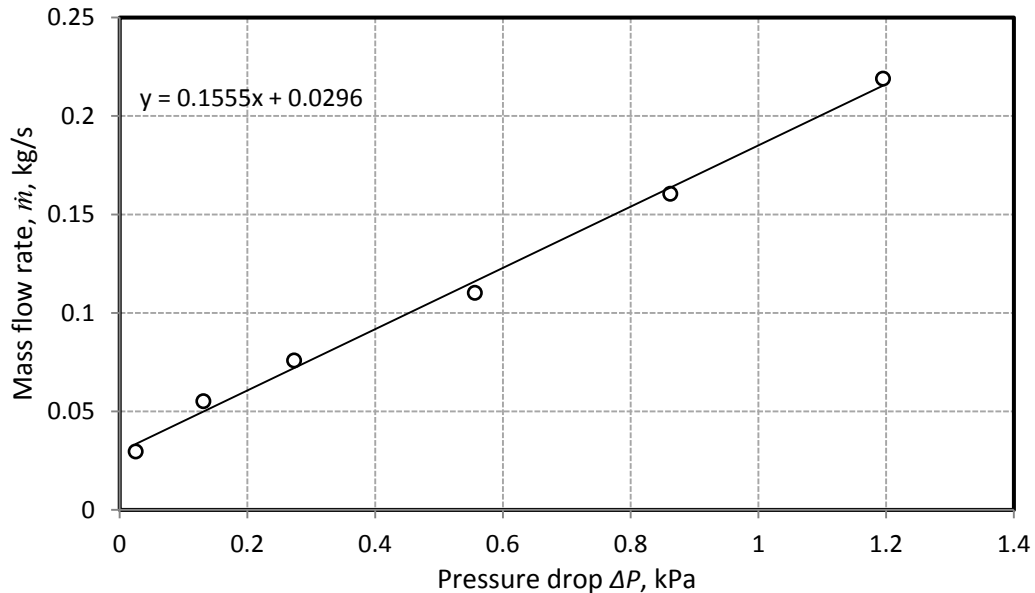

Figure C.4: Venturi calibration curve

Appendix D: Data acquisition

The variable speed drive is operated manually from the mass flow rate reading from the pressure transducers. All the thermocouples, pressure transducers and the pyranometer are connected to an Agilent 32323A data logger with two 20-channel logging cards. The thermocouples are directly converted to a temperature reading whereas the pyranometer and the pressure transducers logs DC voltage outputs and is then converted to the calibrated values from Appendix C.

The data is logged into an excel sheet and converted to the calibrated values with a VBA code while the experiments are in progress. The program receives inputs every 10 seconds from the data logger and performs a time average calculation over 1 minute before data is saved to the spreadsheet. Figure D.1 shows a screen shot of data obtained while performing an experiment.
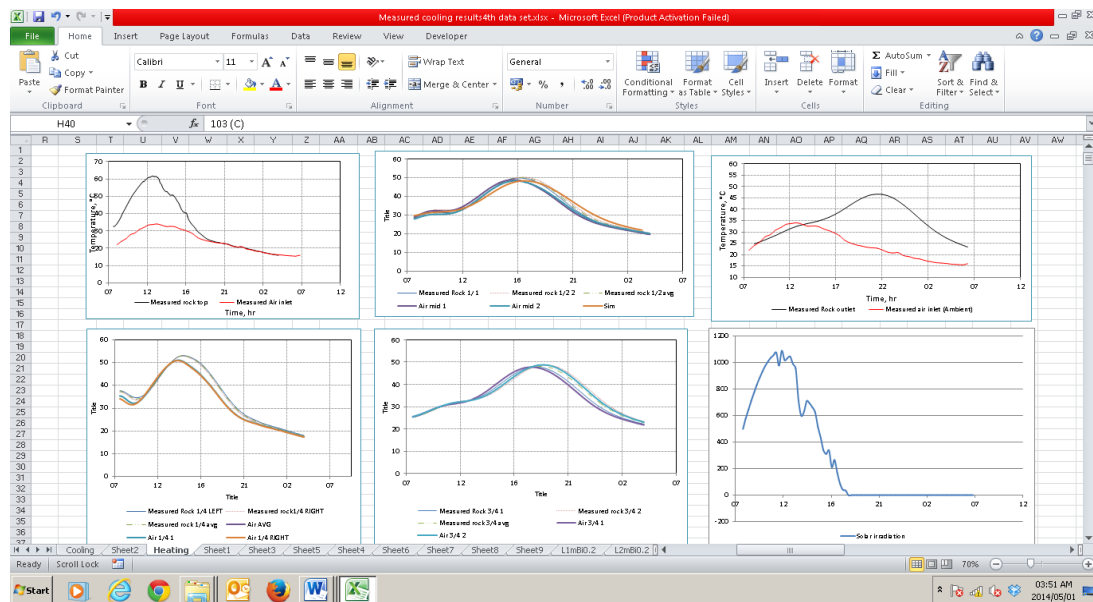

Figure D.1: Screenshot of data acquisition

Appendix E: Wind tunnel experiment

The wind tunnel setup used to verify correlations used in the analysis are illustrated in Figure E.1. Air is drawn through the wind tunnel by means of a centrifugal fan situated at the outlet of the tunnel. An insulated wooden box with a width of 470 mm, a height of 500 mm and a depth of 500 mm (inner dimensions) is used to pile rocks in. Expanded metal is used to hold rocks in place and still allow air through. Thermocouples are placed in the test section for rock and air temperatures. A water air heat exchanger is situated at the inlet in order to heat the air.

Mass flow rates of air are measured and controlled as discussed in Appendix C.2. The pressure drop is measured using an Endress & Hauss pressure transducer. Rocks are heated by the pre-heated air to a constant temperature at a constant mass flow rate. The heat exchanger is removed and room temperature is used to cool the rocks down. The rocks used in the experiment are sample hornfel rocks from the HYDROSOL apparatus having a volume equivalent diameter of 35.2 mm. All experiments are performed twice allowing sufficient time between experiments in order to see if large deviations exist.
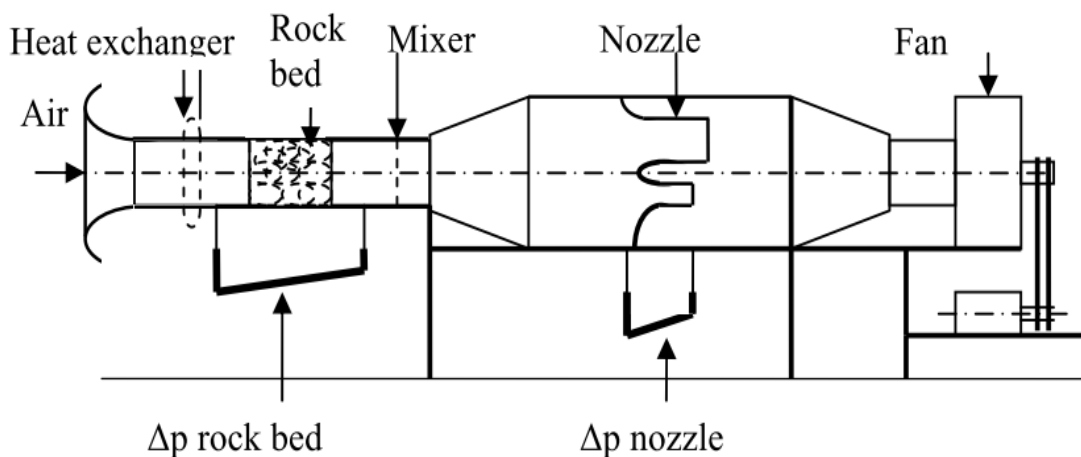

Figure E.1: Wind tunnel experimental setup (Allen, 2010)

Appendix F: Governing equations for mass and heat transfer in the packed rock bed

Derivations of governing equations for Cartesian coordinates are presented as well as the derivations for wet operation in cylindrical coordinates.

F.1:   Cartesian co-ordinate derivations

Consider the system as shown in Figure F.1. Air enters the outer surface in line with the fan position (left bottom). Thus, at the top of the bed, air would enter perpendicular to the horizontal plane and at the bottom inlet it would enter perpendicular to vertical plane.

The deluge water only enters from the top of the bed and flows vertically downwards due to gravity. An elementary control volume is selected at a position in the bed and shown in Figure F.2 with the parameters required for the derivation of the governing equations. It is assumed that constant mass and heat transfer occurs at a position through the width of the bed.
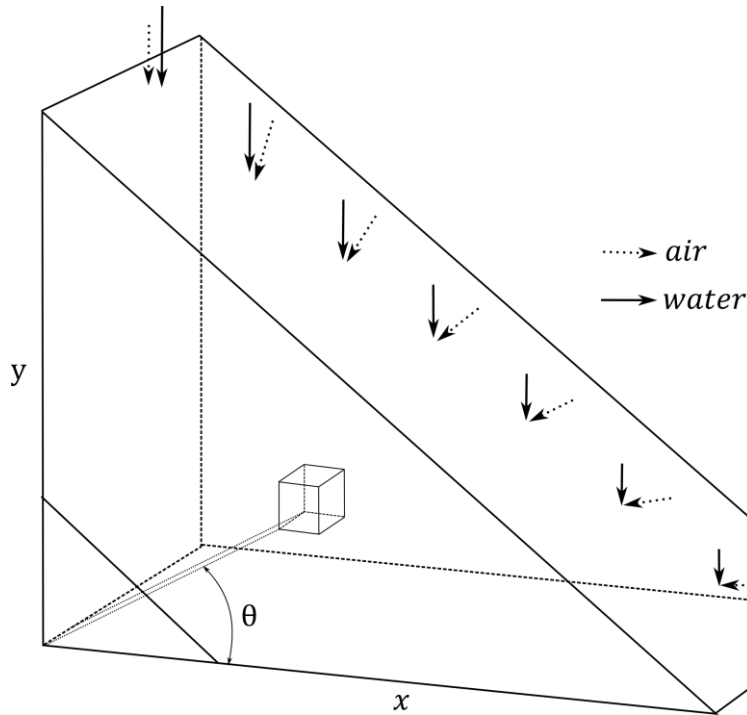

Figure F.1: Control volume in Cartesian co-ordinate system

A dry air mass balance for the control volume shown yields;

$$-G_{a,y+\Delta y}\Delta x\Delta z sin(\theta_{y+\Delta y}) - \left(-G_{a,y}\Delta x\Delta z sin(\theta_y)\right)$$
$$- G_{a,x+\Delta x}\Delta y\Delta z cos(\theta_{x+\Delta x})$$
$$- \left(-G_{a,x}\Delta y\Delta z cos(\theta_x)\right) = 0 \tag{F.1}$$

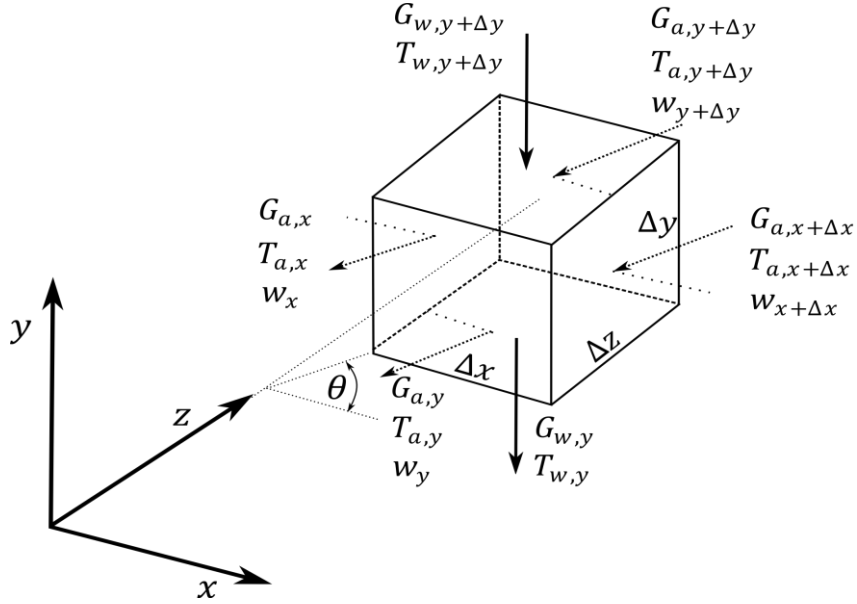**Figure F.2: Elementary control volume for Cartesian co-ordinates**

Divide Eq. (F.1) by $-\Delta x\Delta y\Delta z$ to obtain;

$$\frac{G_{a,y+\Delta y}sin(\theta_{y+\Delta y})}{\Delta y} - \frac{G_{a,y}sin(\theta_y)}{\Delta y} + \frac{G_{a,x+\Delta x}cos(\theta_{x+\Delta x})}{\Delta x}$$
$$- \frac{G_{a,x}cos(\theta_x)}{\Delta x} = 0 \tag{F.2}$$

Let $\Delta x, \Delta y \rightarrow 0$ and apply the product rule of differentiation to find;

$$sin(\theta_y)\frac{\partial G_{a,y}}{\partial y} + G_{a,y}\frac{\partial sin(\theta_y)}{\partial y} + cos(\theta_x)\frac{\partial G_{a,x}}{\partial x}$$
$$+ G_{a,x}\frac{\partial cos(\theta_x)}{\partial x} = 0 \tag{F.3}$$

It is assumed that the water transfer with the momentum is negligible so that no water moves in and out of the control volume in the x-direction. A water mass balance for the control volume yields;

$$-G_{w,y+\Delta y}\Delta x\Delta z - \left(-G_{w,y}\Delta x\Delta z\right)$$
$$- G_{a,y+\Delta y}w_{y+\Delta y}\sin\left(\theta_{y+\Delta y}\right)\Delta x\Delta z$$
$$- \left(-G_{a,y}w_y\sin\left(\theta_y\right)\Delta x\Delta z\right)$$
$$- G_{a,x+\Delta x}w_{x+\Delta x}\cos(\theta_{x+\Delta x})\Delta y\Delta z$$
$$- \left(-G_{a,x}w_x\cos(\theta_x)\Delta y\Delta z\right) = 0$$

(F.4)

Again, divide Eq.(F.4) by $-\Delta x\Delta y\Delta z$ to obtain;

$$\frac{G_{w,y+\Delta y} - G_{w,y}}{\Delta y} + \frac{G_{a,y+\Delta y}w_{y+\Delta y}\sin\left(\theta_{y+\Delta y}\right) - G_{a,y}w_y\sin\left(\theta_y\right)}{\Delta y}$$
$$+ \frac{G_{a,x+\Delta x}w_{x+\Delta x}\cos(\theta_{x+\Delta x}) - G_{a,x}w_x\cos(\theta_x)}{\Delta x}$$
$$= 0$$

(F.5)

Let $\Delta x, \Delta y \to 0$ and apply the product rule of differentiation;

$$\frac{\partial G_{w,y}}{\partial y} + G_{a,y}w_y\frac{\partial \sin\left(\theta_y\right)}{\partial y} + G_{a,y}\sin\left(\theta_y\right)\frac{\partial w_y}{\partial y}$$
$$+ w_y\sin\left(\theta_y\right)\frac{\partial G_{a,y}}{\partial y} + G_{a,x}w_x\frac{\partial \cos(\theta_x)}{\partial x}$$
$$+ w_x\cos(\theta_x)\frac{\partial G_{a,x}}{\partial x} + G_{a,x}\cos(\theta_x)\frac{\partial w_x}{\partial x} = 0$$

(F.6)

Substitute Eq.(F.3) into Eq. (F.6) to find;

$$\frac{\partial G_{w,y}}{\partial y} + G_{a,y}\sin\left(\theta_y\right)\frac{\partial w_y}{\partial y} + G_{a,x}\cos(\theta_x)\frac{\partial w_x}{\partial x} = 0$$

(F.7)

Also, the amount of water that evaporates into the air stream can be written in terms of the definition used by Merkel (1952) for the rate of evaporation as;

$$\frac{\partial G_{w,y}}{\partial y} = h_d a_{Ri}(w_{sw} - w)$$

(F.8)

The mass transfer coefficient, h_d, can be found by making use of the analogy between mass and heat transfer as discussed in Section 3.

Consider the mass and heat transfer of water at the air-water interface;

$$-c_{p,w}T_{w,y+\Delta y}G_{w,y+\Delta y}\Delta x\Delta z - \left(-c_{p,w}T_{w,y}G_{w,y}\Delta x\Delta z\right)$$
$$= -h_c a_{Ri}(T_w - T_a)\Delta x\Delta y\Delta z$$
$$- i_{v_{(T_w)}}h_d a_{Ri}(w_{sw} - w)\,\Delta x\Delta y\Delta z$$

(F.9)

Divide Eq.(F.9) by $-\Delta x\Delta z\Delta y$ to obtain;

F.3

$$\frac{c_{p,w}T_{w,y+\Delta y}G_{w,y+\Delta y} - c_{p,w}T_{w,y}G_{w,y}}{\Delta y}$$
$$= h_c a_{Ri}(T_w - T_a) + i_{v_{(T_w)}} h_d a_{Ri}(w_{sw} - w) \tag{F.10}$$

Let $\Delta x, \Delta y \to 0$ and apply product rule of differentiation;

$$c_{p,w}T_{w,y}\frac{\partial G_{w,y}}{\partial y} + c_{p,w}G_{w,y}\frac{\partial T_{w,y}}{\partial y}$$
$$= h_c a_{Ri}(T_w - T_a) + i_{v_{(T_w)}} h_d a_{Ri}(w_{sw} - w) \tag{F.11}$$

Substitute Eq.(F.8) into Eq.(F.11) to find;

$$c_{p,w}T_{w,y}\big(h_d a_{Ri}(w_{sw} - w)\big) + c_{p,w}G_{w,y}\frac{\partial T_{w,y}}{\partial y}$$
$$= h_c a_{Ri}(T_w - T_a) + i_{v_{(T_w)}} h_d a_{Ri}(w_{sw} - w) \tag{F.12}$$

Eq.(F.12) can be rearranged and simplified to obtain a differential equation describing the water temperature;

$$\frac{\partial T_{w,y}}{\partial y} = \frac{c_{pma}}{c_{pw}}\frac{h_d a_{Ri}}{G_{w,y}}\left[Le_f(T_w - T_a) + \frac{i_{fg_{(Tw)}}}{c_{pma}}(w_{sw} - w)\right] \tag{F.13}$$

The Lewis factor Le_f can be assumed to be $Le_f = 1$ (Merkel (1925) assumption) and with the mean specific heat, $c_{pma} = c_{p,a} + wc_{p,v}$.

Similarly, the mass and heat transfer to air at the air-water interface can be expressed as;

$$-G_{a,y+\Delta y}i_{ma,y+\Delta y}\sin(\theta_{y+\Delta y})\,\Delta x\Delta z$$
$$- \big(-G_{a,y}i_{ma,y}\sin(\theta_y)\,\Delta x\Delta z\big)$$
$$- G_{a,x+\Delta x}i_{ma,x+\Delta x}\cos(\theta_{x+\Delta x})\,\Delta y\Delta z$$
$$- \big(-G_{a,x}i_{ma,x}\cos(\theta_x)\,\Delta y\Delta z\big)$$
$$= h_c a_{Ri}(T_w - T_a)\Delta x\Delta y\Delta z$$
$$+ i_{v_{(T_w)}} h_d a_{Ri}(w_{sw} - w)\,\Delta x\Delta y\Delta z \tag{F.14}$$

Divide Eq.(F.14) by $-\Delta x\Delta y\Delta z$ to find;

$$\frac{G_{a,y+\Delta y}i_{ma,y+\Delta y}\sin(\theta_{y+\Delta y}) - G_{a,y}i_{ma,y}\sin(\theta_y)}{\Delta y}$$
$$+ \frac{G_{a,x+\Delta x}i_{ma,x+\Delta x}\cos(\theta_{x+\Delta x}) - G_{a,x}i_{ma,x}\cos(\theta_x)}{\Delta x} \tag{F.15}$$
$$= -h_c a_{Ri}(T_w - T_a) - i_{v_{(T_w)}} h_d a_{Ri}(w_{sw} - w)$$

Let $\Delta x, \Delta y \to 0$ and apply product rule of differentiation to find;

$$G_{a,y} i_{ma,y} \frac{\partial \sin(\theta_y)}{\partial y} + G_{a,y} \sin(\theta_y) \frac{\partial i_{ma,y}}{\partial y} + i_{ma,y} \sin(\theta_y) \frac{\partial G_{a,y}}{\partial y}$$
$$+ G_{a,x} i_{ma,x} \frac{\partial \cos(\theta_x)}{\partial x} + \cos(\theta_x) G_{a,x} \frac{\partial i_{ma,x}}{\partial x} \quad \text{(F.16)}$$
$$+ i_{ma,x} \cos(\theta_x) \frac{\partial G_{a,x}}{\partial x}$$
$$= -h_c a_{Ri} (T_w - T_a) - i_{v_{(T_w)}} h_d a_{Ri} (w_{sw} - w)$$

Substitute Eq.(F.7) into Eq.(F.16) to simplify to;

$$G_{a,y} \sin(\theta_y) \frac{\partial i_{ma,y}}{\partial y} + \cos(\theta_x) G_{a,x} \frac{\partial i_{ma,x}}{\partial x}$$
$$= -h_c a_{Ri} (T_w - T_a) - i_{v_{(T_w)}} h_d a_{Ri} (w_{sw} - w) \quad \text{(F.17)}$$

Substitute the enthalpy of air from Kröger (2004) into Eq.(F.17) and differentiate to find;

$$G_{a,y} \sin(\theta_y) c_{pa} \frac{\partial T_a}{\partial y} + G_{a,y} \sin(\theta_y) i_{fgwo} \frac{\partial w_y}{\partial y}$$
$$+ G_{a,y} \sin(\theta_y) w_y c_{pv} \frac{\partial T_a}{\partial y}$$
$$+ G_{a,y} \sin(\theta_y) T_{a,y} c_{pv} \frac{\partial w}{\partial y} + G_{a,x} \cos(\theta_x) c_{pa} \frac{\partial T_a}{\partial x}$$
$$+ G_{a,x} \cos(\theta_x) i_{fgwo} \frac{\partial w_x}{\partial x} \quad \text{(F.18)}$$
$$+ G_{a,x} \cos(\theta_x) w_x c_{pv} \frac{\partial T_a}{\partial x}$$
$$+ G_{a,x} \cos(\theta_x) T_a c_{pv} \frac{\partial w_x}{\partial x}$$
$$= -h_c a_{Ri} (T_w - T_a) - i_{v_{(T_w)}} h_d a_{Ri} (w_{sw} - w)$$

Substitute Eq.(F.8) into Eq.(F.18), the definition for the Lewis factor ($Le_f = h_c/c_p h_d$) and rearrange to obtain the differential equation describing the change of the air temperature through the rock bed;

$$G_{a,y} \sin(\theta_y) \frac{\partial T_a}{\partial y} + G_{a,x} \cos(\theta_x) \frac{\partial T_a}{\partial x}$$
$$= -h_d a_{Ri} (T_w - T_a) \left[Le_f + \frac{c_{pv}}{c_{pma}} (w_{sw} - w) \right] \quad \text{(F.19)}$$

The humidity ratio can be determined by substituting Eq.(F.7) into Eq.(F.8) as follow;

$$G_{a,y} \sin(\theta_y) \frac{\partial w_y}{\partial y} + G_{a,x} \cos(\theta_x) \frac{\partial w_x}{\partial x} = -h_d a_{Ri} (w_{sw} - w) \quad \text{(F.20)}$$

Heat transfer to air at the rock surface can be expressed as;

$$
\begin{aligned}
c_{v,R}(1-\varepsilon)\rho_R \frac{\partial T_{R/w}}{dt}\Delta x\Delta y\Delta z \\
= h_c a_{Ri}\left(T_{R/w}-T_a\right)\Delta x\Delta y\Delta z \\
+ i_{v_{(T_w)}}h_d a_{Ri}(w_{sw}-w)\,\Delta x\Delta y\Delta z
\end{aligned}
\tag{F.21}
$$

Divide by $\Delta x\Delta y\Delta z$ and rearrange to obtain;

$$
\frac{dT_{R/w}}{dt} = \frac{\left[h_c a_{Ri}\left(T_{R/w}-T_a\right) + i_{v_{(T_w)}}h_d a_{Ri}(w_{sw}-w)\right]}{c_{v,R}(1-\varepsilon)\rho_R}
\tag{F.22}
$$

F.2: Cartesian co-ordinate governing equations for pressure drop

Consider the momentum diagram as shown in Figure F.3. The momentum accumulation for this case is zero and the only forces are body and surface forces, thus;

$$
\Sigma\vec{F}_{tot} = \Sigma\vec{F}_b + \Sigma\vec{F}_s = \sum_{out}\dot{m}\,u - \sum_{in}\dot{m}u
\tag{F.23}
$$

The net pressure forces acting in normal on the surfaces of the control volume in Figure F.3 can be expressed for the x-direction as;

$$
\Sigma F_{s,x} = p_x\Delta y\Delta z - p_{x+\Delta x}\Delta y\Delta z
\tag{F.24}
$$

Again, frictional force can be found by assuming;

$$
f_{tot} = (f_{co} - f_{cross})\frac{\theta}{\pi/2} + f_{cross}
\tag{F.25}
$$

Substitute the correlations for counter- and cross- current packing into Eq.(F.25) to find;

$$
\begin{aligned}
f_{tot} = \left(76.47\left(\frac{1-\varepsilon}{Re_{pv}}\right)^{0.343} - 80.94\left(\frac{1-\varepsilon}{Re_{pv}}\right)^{0.41}\right)\frac{\theta}{\pi/2} \\
+ 80.94\left(\frac{1-\varepsilon}{Re_{pv}}\right)^{0.41} = \frac{\Delta p}{L^*\left(\frac{\rho_a u_a^2}{2}\right)}\frac{\varepsilon^3}{(1-\varepsilon)}D_v
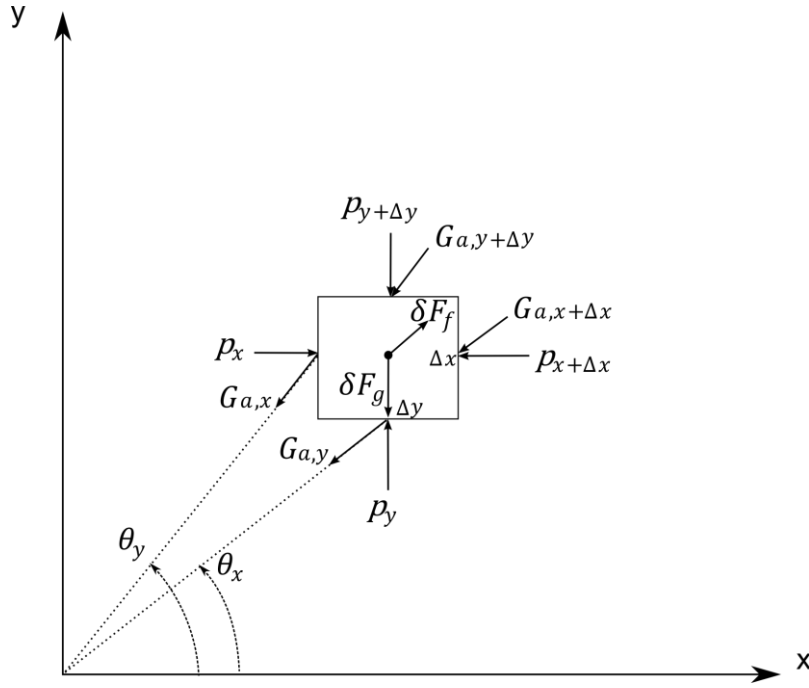\end{aligned}
\tag{F.26}
$$

Figure F.3: Momentum conservation Cartesian co-ordinates

Where the length L^* is also a linear variation from Δx at $\theta = 0$ to Δy at $\theta = \pi/2$;

$$\delta F_{res} = \frac{\Delta p Q}{u} = f_{tot}\left(\frac{\rho_a u_a^2}{2}\right)\frac{(1-\varepsilon)}{\varepsilon^3}\frac{Q}{u D_v} \tag{F.27}$$

The net convective transport for x- and y direction can be found respectively by;

$$-p_x \Delta y \Delta z - (-p_{x+\Delta x}\Delta y \Delta z) + f_{tot}\left(\frac{\rho_a u_a^2}{2}\right)\frac{(1-\varepsilon)}{\varepsilon^3}\frac{Q}{u_{a,x}}\cos(\theta)$$
$$= -(-\rho_a u_{a,x+\Delta x}^2 \cos(\theta_{x+\Delta x})\,\Delta y \Delta z)$$
$$- \rho_a u_{a,x}^2 \cos(\theta_x)\Delta y \Delta z \tag{F.28}$$

$$-p_y \Delta y \Delta z - (-p_{y+\Delta y}\Delta y \Delta z) + f_{tot}\left(\frac{\rho_a u_a^2}{2}\right)\frac{(1-\varepsilon)}{\varepsilon^3}\frac{Q}{u_{a,y}}\sin(\theta)$$
$$= -(-\rho_a u_{a,y+\Delta y}^2 \sin(\theta_{y+\Delta y})\,\Delta x \Delta z)$$
$$- \rho_a u_{a,y}^2 \sin(\theta_y)\,\Delta x \Delta z - \rho_w u_{w,y}^2 \Delta x \Delta z \tag{F.29}$$
$$- (-\rho_w u_{w,y+\Delta y}^2 \Delta x \Delta z)$$

Divide by $\Delta x \Delta y \Delta z$ to find;

$$\frac{p_{x+\Delta x} - p_x}{\Delta x} + f_{tot}\Delta x \left(\frac{\rho_a u_a^2}{2}\right)\frac{(1-\varepsilon)}{\varepsilon^3}\cos(\theta)$$
$$= \frac{\rho_a u_{a,x+\Delta x}^2 \cos(\theta_{x+\Delta x}) - \rho_{a,x} u_{a,x}^2 \cos(\theta_x)}{\Delta x} \tag{F.30}$$

F.7

$$\frac{p_{y+\Delta y} - p_y}{\Delta y} + f_{tot}\Delta y \left(\frac{\rho_a u_a^2}{2}\right)\frac{(1-\varepsilon)}{\varepsilon^3}\sin(\theta)$$
$$= \frac{\rho_a u_{a,y+\Delta y}^2 \sin(\theta_{y+\Delta y}) - \rho_a u_{ay}^2 \sin(\theta_x)}{\Delta y}$$
$$+ \frac{\rho_w u_{w,y+\Delta y}^2 - \rho_w u_{w,y}^2}{\Delta y} \tag{F.31}$$

Let $\Delta x, \Delta y \to 0$ and rearrange to obtain;

$$\frac{\partial p}{\partial x} = -\left[\left(76.47\left(\frac{1-\varepsilon}{Re_{pv}}\right)^{0.343} - 80.94\left(\frac{1-\varepsilon}{Re_{pv}}\right)^{0.41}\right)\frac{\theta_x}{\frac{\pi}{2}}\right.$$
$$\left. + 80.94\left(\frac{1-\varepsilon}{Re_{pv}}\right)^{0.41}\right]\Delta x\left(\frac{\rho_a u_a^2}{2}\right)\frac{(1-\varepsilon)}{\varepsilon^3}\cos(\theta_x) \tag{F.32}$$
$$+ \rho_a u_{a,x}^2 \frac{\partial \cos(\theta_x)}{\partial x} + \rho_a 2u_{a,x}\cos(\theta_x)\frac{\partial u_{a,x}}{\partial x}$$

$$\frac{\partial p}{\partial y} = -\left[\left(76.47\left(\frac{1-\varepsilon}{Re_{pv}}\right)^{0.343} - 80.94\left(\frac{1-\varepsilon}{Re_{pv}}\right)^{0.41}\right)\frac{\theta_x}{\frac{\pi}{2}}\right.$$
$$\left. + 80.94\left(\frac{1-\varepsilon}{Re_{pv}}\right)^{0.41}\right]\Delta x\left(\frac{\rho_a u_a^2}{2}\right)\frac{(1-\varepsilon)}{\varepsilon^3}\sin(\theta_x)$$
$$+ \rho_a u_{a,y}^2 \frac{\partial \sin(\theta_y)}{\partial y} + \rho_a 2u_{a,y}\sin(\theta_x)\frac{\partial u_{a,y}}{\partial y} \tag{F.33}$$
$$+ u_{w,y}^2 \frac{\partial \rho_w}{\partial y} + 2u_{w,y}\rho_w\frac{\partial u_w}{\partial y}$$

F.3: Cylindrical co-ordinate governing equations for wet cooling

Consider the control volume depicted in Figure 3.2 and consider the system during an evaporative cooling cycle using water. It is assumed that the water layer on the rock surfaces is infinitely thin so that the rocks can be modelled as large stationary water drops having the properties of rock. Also the water leaving the first control volume is saturated with water vapour. The thermal capacitance of air can be neglected when compared to that of the rock. The RHRL at the top is assumed to be insulated and no heat is lost to the atmosphere. A water mass balance for the control volume in Figure 3.2 can be performed in a similar way as dry air with some trigonometry, to account for the angles of water flowing vertically downwards, and be written as;

$$-G_{w,r+\Delta r}\sin(\theta+\Delta\theta/2)\,(r+\Delta r)\Delta\theta\Delta z$$
$$-\left(-G_{w,r}\sin(\theta+\Delta\theta/2)\,r\Delta\theta\Delta z\right)$$
$$+\left(-G_{w,\theta+\Delta\theta}\cos(\theta+\Delta\theta)\,\Delta r\Delta z\right)$$
$$-\left(-G_{w,\theta}\cos(\theta)\,\Delta r\Delta z\right) \tag{F.34}$$
$$+\left[-G_{a,r+\Delta r}w_{r+\Delta r}(r+\Delta r)\Delta\theta\Delta z\right]$$
$$-\left(-G_{a,r}w_r r\Delta\theta\Delta z\right)=0$$

Divide Eq. (F.34) by $-r\Delta\theta\Delta r\Delta z$ to obtain;

$$\frac{(\rho u)_{w,r+\Delta r}\sin(\theta+\Delta\theta/2)}{\Delta r}+\frac{(\rho u)_{w,r+\Delta r}\sin(\theta+\Delta\theta/2)}{r}$$
$$-\frac{(\rho u)_{w,r}\sin(\theta+\Delta\theta/2)}{\Delta r}+\frac{(\rho u)_{w,\theta+\Delta\theta}\cos(\theta+\Delta\theta)}{r\Delta\theta}$$
$$-\frac{(\rho u)_{w,\theta}\cos(\theta)}{r\Delta\theta}+\frac{(\rho u)_{a,r+\Delta r}w_{r+\Delta r}}{\Delta r} \tag{F.35}$$
$$+\frac{(\rho u)_{a,r+\Delta r}w_{r+\Delta r}}{r}-\frac{(\rho u)_{a,r}w_r}{\Delta r}=0$$

Let $\Delta r,\Delta\theta\to 0$, differentiate and substitute Eq.(3.3) to obtain a differential equation describing the mass flow rate of water;

$$\sin(\theta)\frac{\partial(\rho u)_w}{\partial r}+\cos(\theta)\frac{\partial(\rho u)_w}{r\,\partial\theta}+(\rho u)_a\frac{\partial w}{\partial r}=0 \tag{F.36}$$

Employing the definition of Mass transfer rate of Merkel (1925), the rate of evaporation can be expressed as;

$$\sin(\theta)\frac{\partial(\rho u)_w}{\partial r}+\cos(\theta)\frac{\partial(\rho u)_w}{r\,\partial\theta}=-h_d a_{Ri}(w_{sw}-w) \tag{F.37}$$

where h_d is the mass transfer coefficient obtained from the analogy between mass and heat transfer as discussed in Section 2.4.

For the thermal governing equations, consider the heat transfer of water at the air-water interface;

$$-c_{p,w}T_{w,r+\Delta r}G_{w.r+\Delta r}\sin(\theta + \Delta\theta/2)\,(r + \Delta r)\Delta\theta\Delta z$$

$$- \left[-c_{p,w}T_{w,r}G_{w,r}\sin(\theta + \Delta\theta/2)\,r\Delta\theta\Delta z \right]$$

$$+ \left[-c_{p,w}T_{w,\theta+\Delta\theta}G_{w,\theta+\Delta\theta}\cos(\theta + \Delta\theta)\Delta r\Delta z \right]$$

$$- \left[-c_{p,w}T_{w,\theta}G_{w,\theta}\cos(\theta)\,\Delta r\Delta z \right]$$

$$- h_{c,R/w-aRm}(T_w - T_{a,Rm})dA_c \tag{F.38}$$

$$- i_{v_{(T_w)}}h_{d,R/w-aRm}(w_{sw} - w)dA_d$$

$$= (1 - \varepsilon)\rho_R c_{v,R}\mathrm{r}\Delta\mathrm{r}\Delta\theta\Delta z\frac{dT_w}{dt}$$

The specific heat of water and air is assumed to be constant. The surface area for diffusion dA_d and convection dA_c is the same. Divide Eq. (F.38) with $-r\Delta\theta\Delta r\Delta z$ to obtain;

$$\frac{c_{p,w}T_{w,r+\Delta r}G_{w.r+\Delta r}\sin(\theta + \Delta\theta/2)}{\Delta r}$$

$$+ \frac{c_{p,w}T_{w,r+\Delta r}G_{w.r+\Delta r}\sin(\theta + \Delta\theta/2)}{r}$$

$$- \frac{c_{p,w}T_{w,r}G_{w,r}\sin(\theta + \Delta\theta/2)}{\Delta r}$$

$$+ \frac{c_{p,w}T_{w,\theta+\Delta\theta}G_{w,\theta+\Delta\theta}\cos(\theta + \Delta\theta)}{r\Delta\theta} \tag{F.39}$$

$$- \frac{c_{p,w}T_{w,\theta}G_{w,\theta}\cos(\theta)}{r\Delta\theta} + h_{c,R/w-aRm}a_{Ri}(T_w - T_a)$$

$$+ i_{v_{(T_w)}}h_{d,R/w-aRm}a_{Ri}(w_{sw} - w)$$

$$= -(1 - \varepsilon)\rho_R c_{v,R}\frac{dT_w}{dt}$$

Let $\Delta r, \Delta\theta \to 0$ and apply chain rule of differentiation to obtain the following differential equation;

$$c_{p,w} \sin(\theta) T_w \frac{\partial G_{w.r}}{\partial r} + c_{p,w} \sin(\theta) G_{w,r} \frac{\partial T_w}{\partial r} + \frac{c_{p,w} T_w G_{w,r} \sin(\theta)}{r}$$

$$+ c_{p,w} \cos(\theta) T_w \frac{\partial G_{w\theta}}{r\partial\theta} + c_{p,w} \cos(\theta) G_{w,\theta} \frac{\partial T_w}{r\partial\theta}$$

$$- \frac{c_{p,w} T_w G_{w,\theta} \sin(\theta)}{r} + h_{c,R/w-aRm} a_{Ri}(T_w - T_a) \qquad (F.40)$$

$$+ i_{v(T_w)} h_{d,R/w-aRm} a_{Ri}(w_{sw} - w)$$

$$= -(1 - \varepsilon)\rho_R c_{v,R} \frac{dT_{R/w}}{dt}$$

Substitute Eq.(F.37) into above equation as well as the definition of water vapour from Kröger (2004) at the bulk water temperature and rearrange to obtain;

$$c_{p,w} \sin(\theta) G_{w,r} \frac{\partial T_w}{\partial r} + \frac{c_{p,w} T_w \sin(\theta)}{r}(G_{w,r} - G_{w,\theta})$$

$$+ c_{p,w} \cos(\theta) G_{w,\theta} \frac{\partial T_w}{r\partial\theta}$$

$$+ h_{c,R/w-aRm} a_{Ri}(T_{R/w} - T_a) \qquad (F.41)$$

$$+ i_{fg(T_w)} h_{d,R/w-aRm} a_{Ri}(w_{sw} - w)$$

$$= -(1 - \varepsilon)\rho_R c_{v,R} \frac{dT_{R/w}}{dt}$$

Eq. (F.40) can be further simplified by substituting the definition of Lewis factor, $Le_f = h_c/(c_{p,ma} h_d)$, into the equation. The water (and in effect rock) temperature can thus be described by;

$$\frac{dT_{R/w}}{dt} = -\left\{ c_{p,w} \sin(\theta) G_{w,r} \frac{\partial T_{R/w}}{\partial r} \right.$$

$$+ \frac{c_{p,w} T_{R/w} \sin(\theta)}{r}(G_{w,r} - G_{w,\theta})$$

$$+ c_{p,w} \cos(\theta) G_{w,\theta} \frac{\partial T_{R/w}}{r\partial\theta} \qquad (F.42)$$

$$+ c_{p,ma} h_{d,R/w-aRm} a_{Ri} \left[Le_f(T_{R/w} - T_a) \right.$$

$$\left. \left. + \frac{i_{fg(T_w)}}{c_{p,ma}}(w_{sw} - w) \right] \right\} / (1 - \varepsilon)\rho_R c_{v,R}$$

F.11

Following the same procedure, the air temperature can be described by considering the heat transfer of air at the air- water interface;

$$-G_{a,r+\Delta r}i_{ma,r+\Delta r}(r + \Delta r)\Delta\theta\Delta z - \left[-G_{a,r}i_{ma,r}r\Delta\theta\Delta z\right]$$
$$- h_{c,aRm-R/w}(T_{aRm} - T_{R/w})dA_c \tag{F.43}$$
$$- i_{v_{(T_w)}}h_{d,aRm-R/w}(w_{sw} - w)dA_d = 0$$

Again, dividing Eq.(F.43) by $-r\Delta\theta\Delta r\Delta z$ yields the following;

$$\frac{G_{a,r+\Delta r}i_{ma,r+\Delta r}}{\Delta r} + \frac{G_{a,r+\Delta r}i_{ma,r+\Delta r}}{r} - \frac{G_{a,r}i_{ma,r}}{\Delta r}$$
$$= \left[-h_{c,aRm-R/w}a_{ri}(T_{aRm} - T_{R/w})\right. \tag{F.44}$$
$$\left. - i_{v_{(T_w)}}h_{d,aRm-R/w}a_{Ri}(w_{sw} - w)\right]$$

Let $\Delta r, \Delta\theta \to 0$, differentiate, substitute Eq.(3.3), Eq. (F.36), Eq. (F.37) and the enthalpy of air-vapour mixture from Kröger (2004) into the above equation to obtain;

$$G_a\frac{\partial T_a}{\partial r}c_{p,ma} - h_{d,aRm-R/w}a_{Ri}(w_{sw} - w)(i_{fg} + c_{p,v}T_a)$$
$$= -h_{c,aRm-R/w}a_{ri}(T_{aRm} - T_{R/w}) \tag{F.45}$$
$$- i_{v_{(T_w)}}h_{d,aRm-R/w}a_{Ri}(w_{sw} - w)$$

Substitute the enthalpy of water vapour from Kröger (2004) and rearrange to find;

$$G_a\frac{\partial T_a}{\partial r}c_{pma} = -h_{c,aRm-R/w}a_{ri}(T_{aRm} - T_{R/w})$$
$$- c_{pv}(T_a - T_{R/w})h_{d,aRm-R/w}a_{Ri}(w_{sw} - w) \tag{F.46}$$

By using the definition of the Lewis factor the air temperature can be described with;

$$G_a\frac{\partial T_a}{\partial r} = -h_{d,aRm-R/w}a_{ri}(T_{aRm} - T_{R/w})\left[Le_f\right.$$
$$\left. + \frac{c_{p,v}}{c_{p,ma}}(w_{sw} - w)\right] \tag{F.47}$$

Appendix G: Control and parametric study cont.
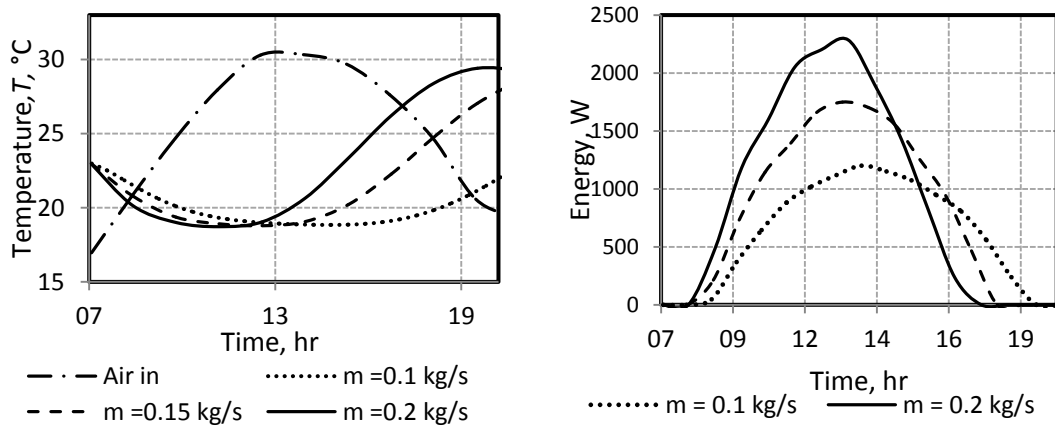
Figure G.1: Mass flow rate on outlet temperature and energy –winter's day
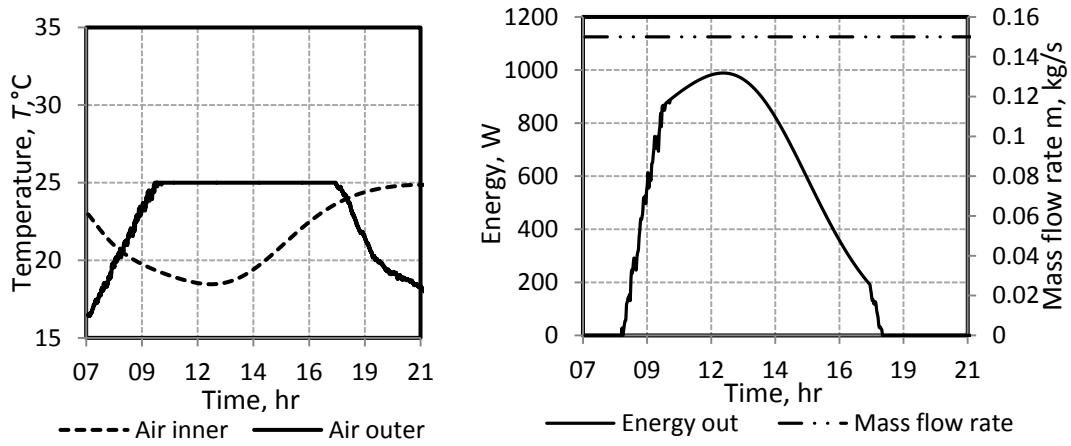
(a) Constant mass flow rate $Bi_{max} = 0.2, T_{set} = 25°C, R = 2$ m
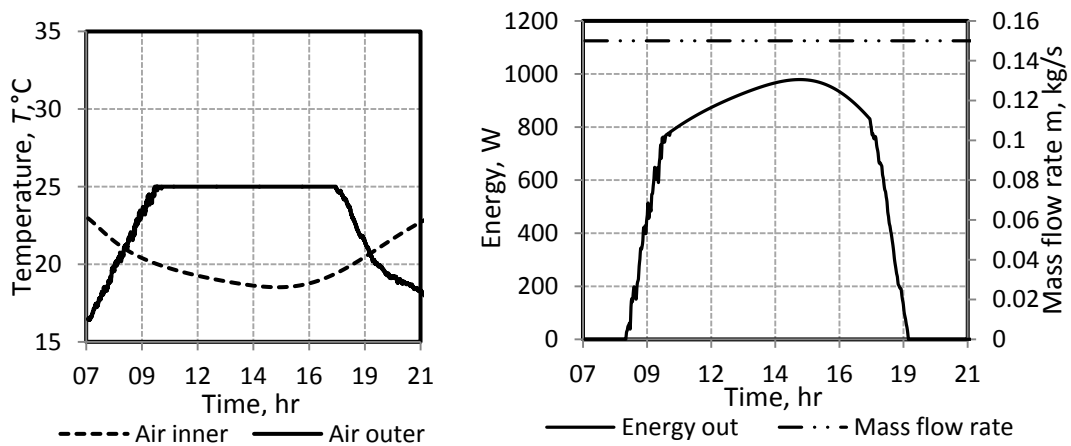
(b) Constant mass flow rate $Bi_{max} = 0.2, T_{set} = 25°C, R = 2.5$ m
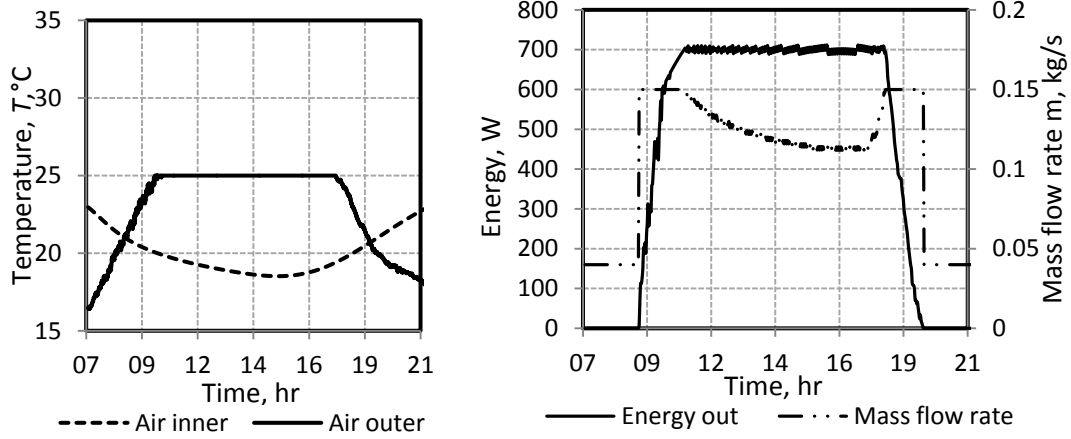
(c) Constant energy $Bi_{max} = 0.2, T_{set} = 25°C, R = 2.5$ m
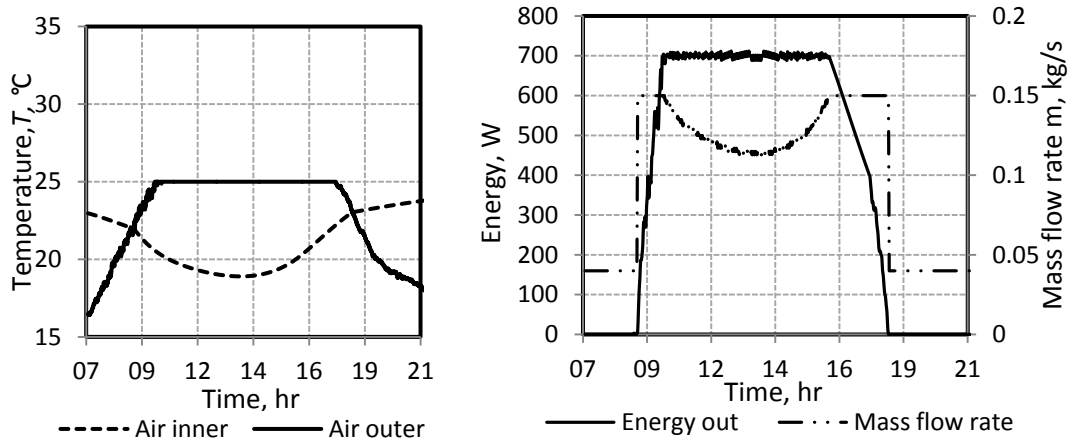
(d) Constant energy $Bi_{max} = 0.2, T_{set} = 25°C, R = 2$ m
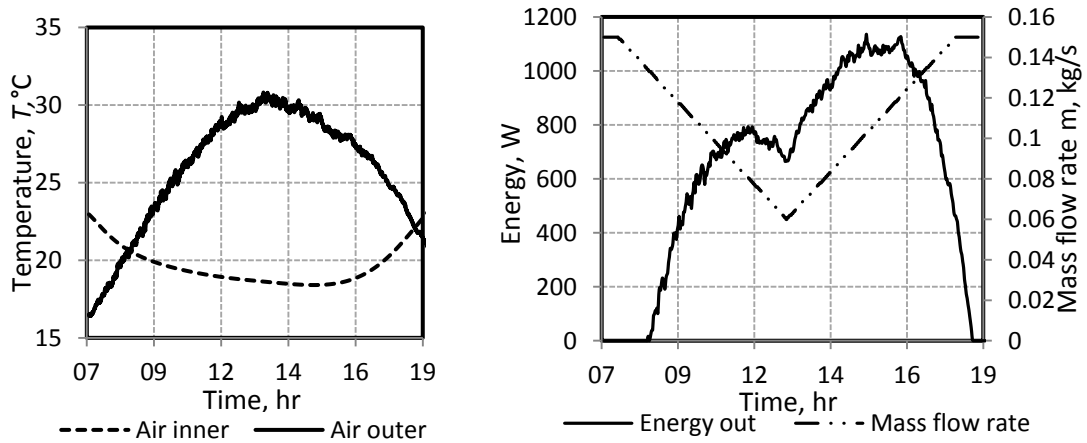
(d) Linear mass flow rate $Bi \approx 0.2$ @ $7:30$ to $Bi \approx 0.1$ @ $13:00$ to $Bi = 0.2$ @ $18:00$, $R = 2$ m

G.2
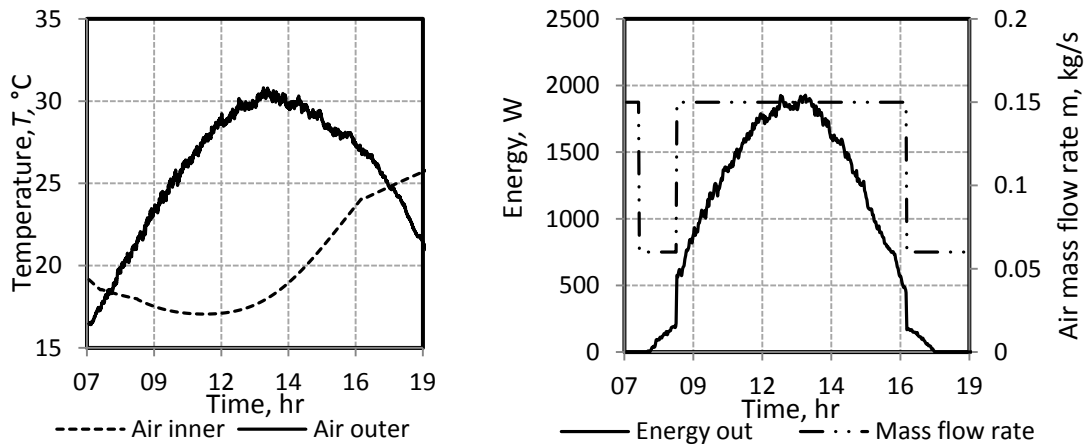
(e) Step mass flow rate, $Bi \approx 0.1$ @ $7{:}30$ to $Bi_{max} \approx 0.2$ @ $9{:}00, Bi = 0.1$ @ $17{:}00$, $L = 2$ m

Figure G.2: Mass flow rate control parametric study cont.
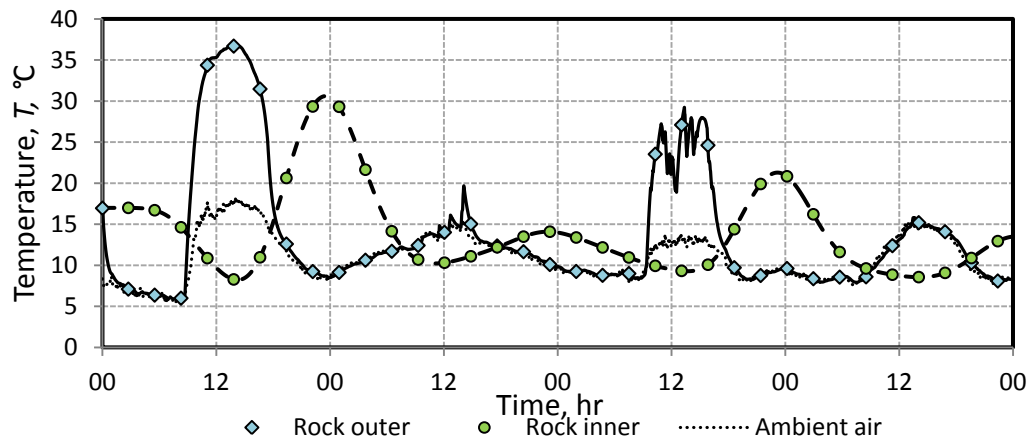
Figure G.3: PFC/PFD, $\dot{m}_a$ = 0.15 kg/s
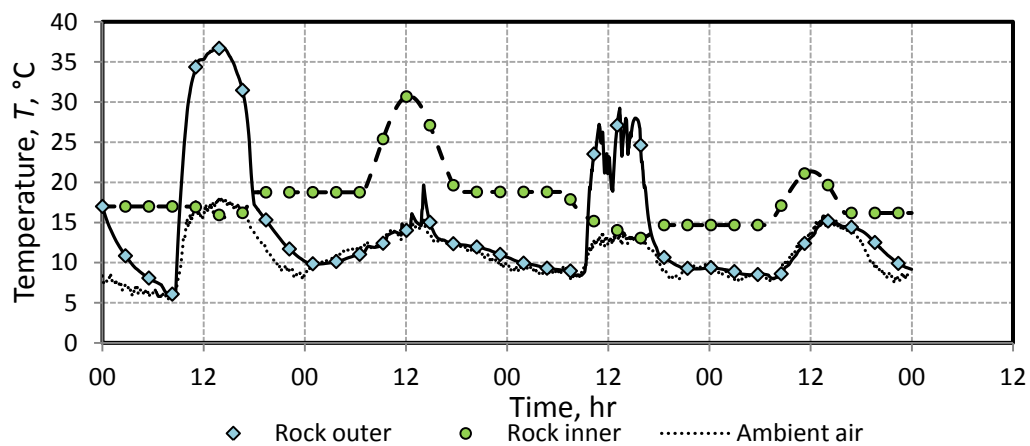
Figure G.4: PFC/PFD, switch off night, $\dot{m}_a$ = 0.15 kg/s
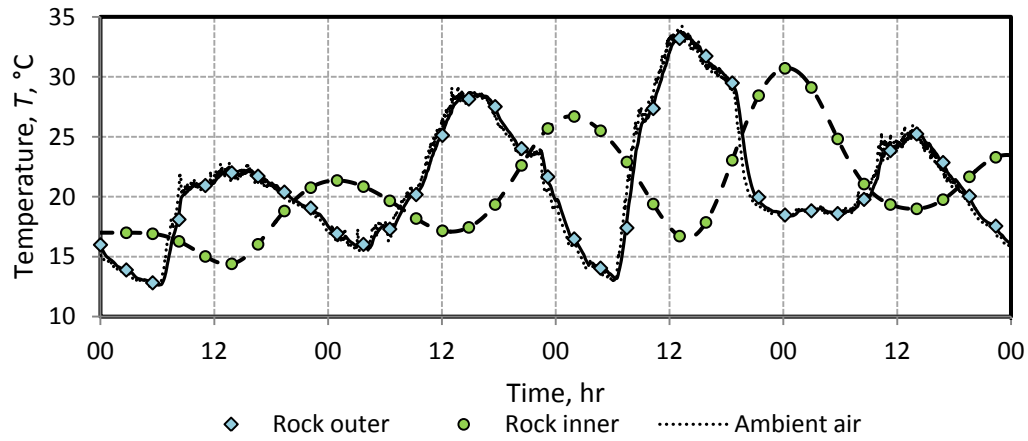
Figure G.5: NFC/NFD, $\dot{m}_a = 0.15$ kg/s
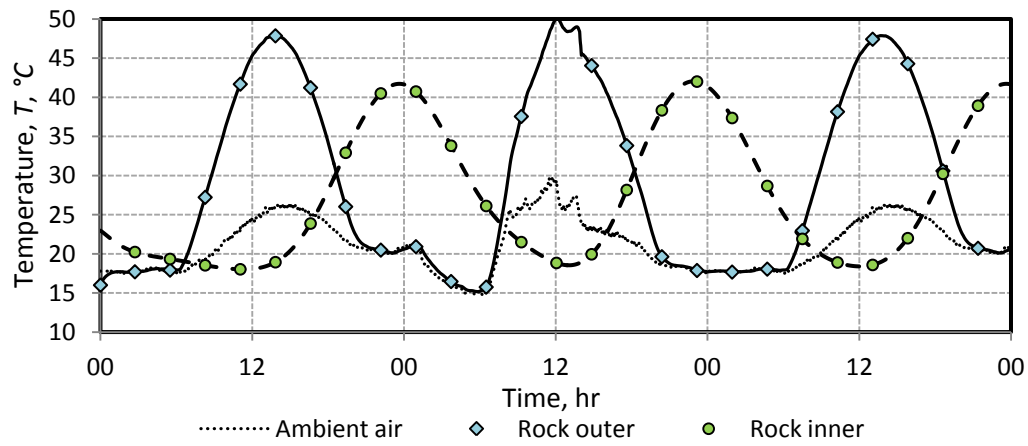
Figure G.6: PFC/PFD, $\dot{m}_a = 0.13$ kg/s

G.4
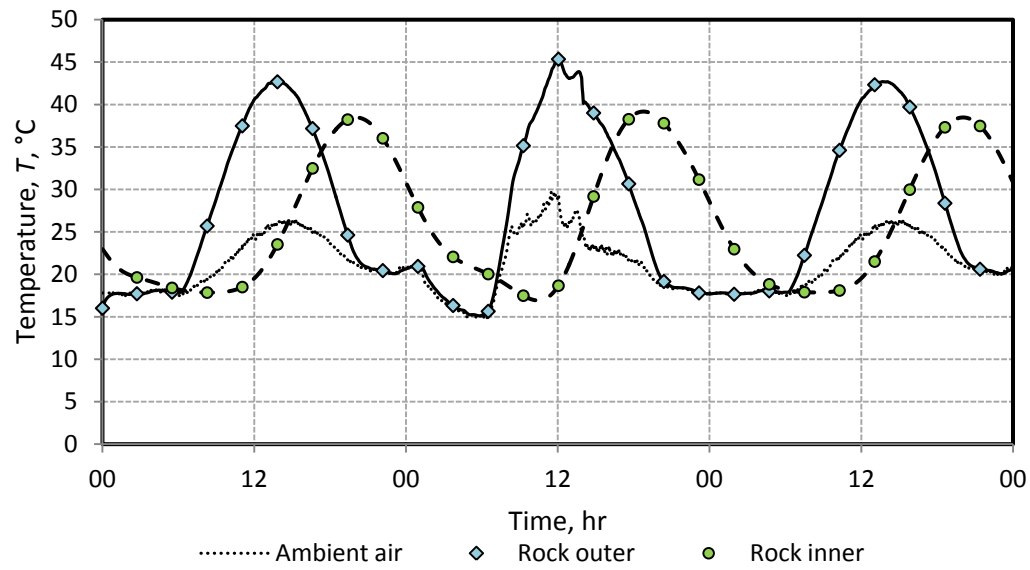
Figure G.7: PFC/PFD, $\dot{m}_a$ = 0.15 kg/s

Appendix H: PETG specifications

Polyethylene Terephthalate Glycol-modified (PETG)

Transmissivity experimentally determined by Rohwer (2013) at a fixed angle as shown in Figure H.1 as well as at different angles as shown in Figure H.2. A cost comparison of different glazing materials are shown in Table H.1. The PETG specifications can be found in

Table H.2.
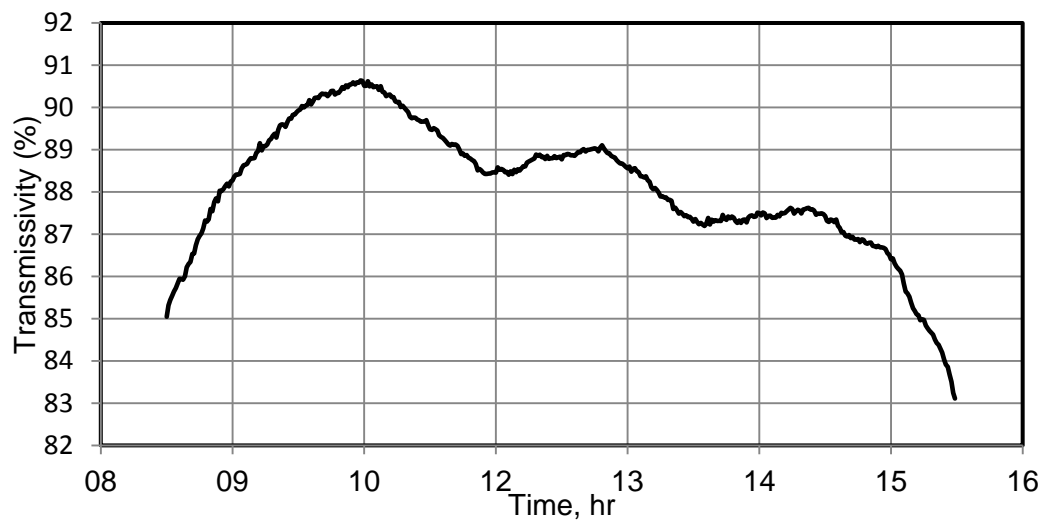
Figure H.1: Transmissivity @ 40° fixed (Rohwer, 2013)
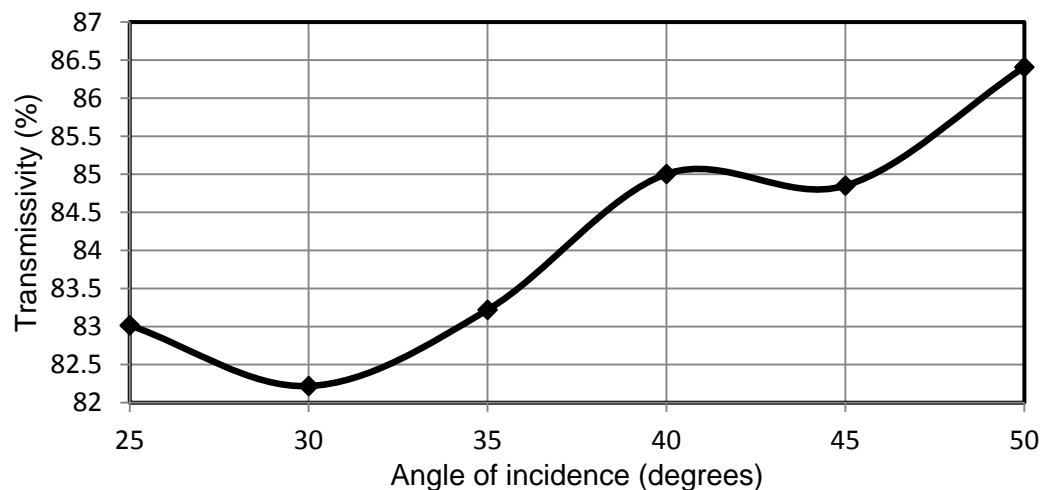
Figure H.2: Transmissivity @ 25° to 50° (Rohwer, 2013)

H.1

Table H.1: Cost comparison of glazing materials (Rohwer, 2013)

Material	Transmissivity	Cost (R/m^2) (thickness)
Glass	85.78	222.66 (4 mm)
PETG	84.83	238.12 (3 mm)
Greenhouse polymer	78.70	135.5 (1.6 mm)

Table H.2: PETG specification sheet

Density (kg/m^3)	1270
Specific heat (J/kgK)	1200
Thermal conductivity (W/mK)	0.24
Melting point (°C)	140
Minimum transparency (%)	81
Emissivity	0.9

Appendix I: Sample Calculations

Ambient conditions

Atmospheric pressure	$p_{atm} = 101325\ \text{Pa}$
Ambient dry bulb temperature	$T_{amb,db} = 15\ °\text{C}$
Ambient wet bulb temperature	$T_{amb,wb} = 13.5\ °\text{C}$

Numerical inputs

Radial increment	$\Delta r = 0.035\ \text{m}$
Theta increment	$\Delta\theta = 0.035\ °$
Time step	$\Delta t = 10\ \text{s}$
Initial rock temperature	$T_{R,init} = 20\ °\text{C}$
Initial cover temperature	$T_{cp,init} = 15\ °\text{C}$
Maximum Biot number	$Bi = 0.2$

Physical properties of the system

Bed width	$L_b = 1.22\ \text{m}$
Effective outer radius	$R_o = 2\ \text{m}$
Effective inner radius	$R_i = 0.5\ \text{m}$

Rock density	$\rho_R = 2500\ \text{kg/m}^3$
Rock specific heat	$c_{p,R} = 820\ \text{J/kgK}$
Rock thermal conductivity	$k_R = 2.1\ \text{W/mK}$
Rock emissivity	$\varepsilon_R = 0.9$
Rock bed void fraction	$\varepsilon = 0.4$
Rock volume equivalent diameter	$D_v = 0.035\ \text{m}$
Rock absorptivity	$\alpha_R = 1$

PETG density	$\rho_{cp} = 1270\ \text{kg/m}^3$
PETG transmissivity	$\tau_{cp} = 0.85$
PETG reflectivity	$\rho_{cp} = 0.9$
PETG emissivity	$\varepsilon_{cp} = 0.9$

Air channel hydraulic diameter	$d_h = 0.48\ \text{m}$

Geometric relations and Areas

Outer frontal area

$$A_{fr,o} = R_o \frac{\pi}{2} L_b = 3.833\ \text{m}^2$$

Inner frontal area

$$A_{fr,i} = R_i \frac{\pi}{2} L_b = 0.958 \text{ m}^2$$

Volume equivalent Particle Reynolds number- inner space

$$Re_{pv} = \left[2\, Bi \frac{k_R}{k_a} - 2/1.1 Pr^{\frac{1}{3}} \right]^{1/0.6} = 466.2$$

Maximum velocity at inner space

$$u_{max} = \frac{Re_{pv}\mu_a}{\rho_a D_v} = 0.197 \text{ m/s}$$

Rock surface area per volume

$$a_{Ri} = \frac{6(1-\varepsilon)}{D_v} = 102.85 \text{ m}^{-1}$$

Maximum mass flow rate

$$\dot{m}_{max} = \rho_a u_{max} A_{fr,i} = 0.191 \text{ kg/s}$$

Air channel Reynolds number

$$Re_{L,max} = \frac{\rho_a u_a D_h}{\mu_a} = 7200$$

Converged iteration parameters for outer bottom control volume first time step

Rock temperature	$T_{R(1,1)}^1 = 19.9\,°C$
Air temperature	$T_{a(1,1)}^1 = 16.12\,°C$
Convective heat transfer coefficient	$h_{c(1,1)}^1 = 15.46 \text{ W/m}^2\text{K}$
Particle Reynolds number	$Re_{pv(1,1)}^1 = 156.19$
Superficial velocity	$u_{s(1,1)}^1 = 0.069 \text{ m/s}$
Pressure drop	$\Delta p_{(1,1)}^1 = 0.11 \text{ Pa}$

Converged iteration parameters for inner bottom control volume 500 time steps

Rock temperature	$T_{R(Nr,1)}^{500} = 19.97\,°C$
Air temperature	$T_{a(Nr,1)}^{500} = 19.958\,°C$
Convective heat transfer coefficient	$h_{c(Nr,1)}^{500} = 34.51 \text{ W/m}^2\text{K}$
Particle Reynolds number	$Re_{pv(Nr,1)}^{500} = 583.62$
Superficial velocity	$u_{s(Nr,1)}^{500} = 0.259 \text{ m/s}$
Pressure drop	$\Delta p_{(Nr,1)}^{500} = 1.542 \text{ Pa}$
Total pressure drop	$\Delta p_{tot}^{500} = 23 \text{ Pa}$

Broiler house calculations (a)

Broiler house length $\qquad$ $L_{bh} = 200$ m
Broiler house width $\qquad$ $W_{bh} = 6$ m
Broiler house height $\qquad$ $H_{bh} = 1.8$ m

Geometric relations and areas

Broiler house frontal area for tunnel ventilation

$$A_{fr} = W_{bh}H_{bh} \quad = 10.8 \text{ m}^2$$

Maximum mass flow rate from HYDROSOL system 200 m long with Biot maximum at 0.5 m inner radius

$$\dot{m}_a = 28.6 \text{ kg/s}$$

Velocity in broiler house

$$u_{bh} = \dot{m}_a / \rho_a A_{bh} = 2.21 \ m/s$$

Broiler house calculations (b)

Broiler house length $\qquad$ $L_{bh} = 120$ m
Broiler house width $\qquad$ $W_{bh} = 12$ m
Broiler house height $\qquad$ $H_{bh} = 1.8$ m

Geometric relations and areas

Broiler house frontal area for tunnel ventilation

$$A_{fr} = W_{bh}H_{bh} \quad = 21.6 \text{ m}^2$$

Maximum mass flow rate from HYDROSOL system 120 m long with Biot maximum at 0.5 m inner radius

$$\dot{m}_a = 17.17 \text{ kg/s}$$

Velocity in broiler house

$$u_{bh} = \dot{m}_a / \rho_a A_{bh} = 0.662 \text{ m/s}$$

Appendix J: Suitable concept cont.
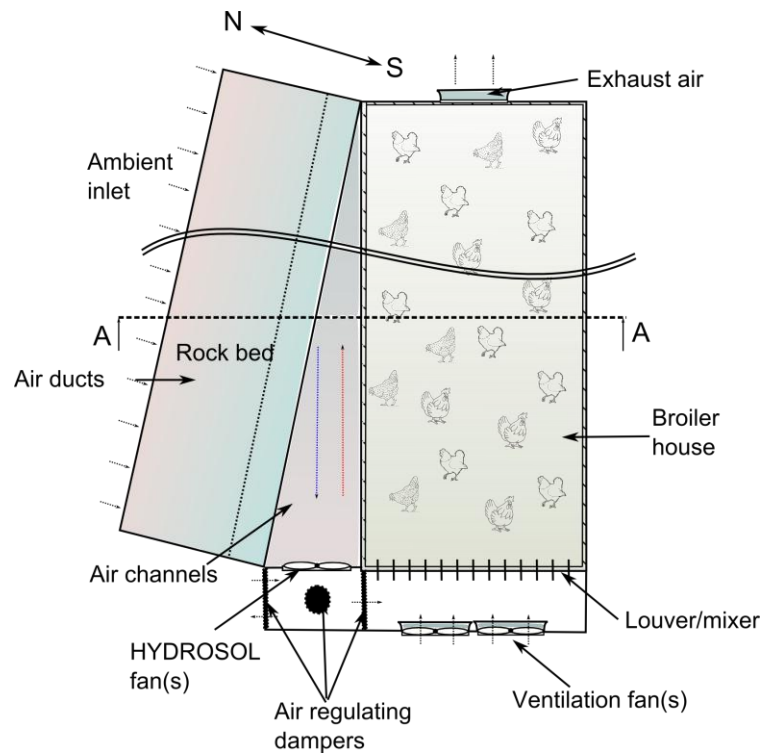
Figure J.1: Top view: HYDROSOL system connected to broiler house (B)
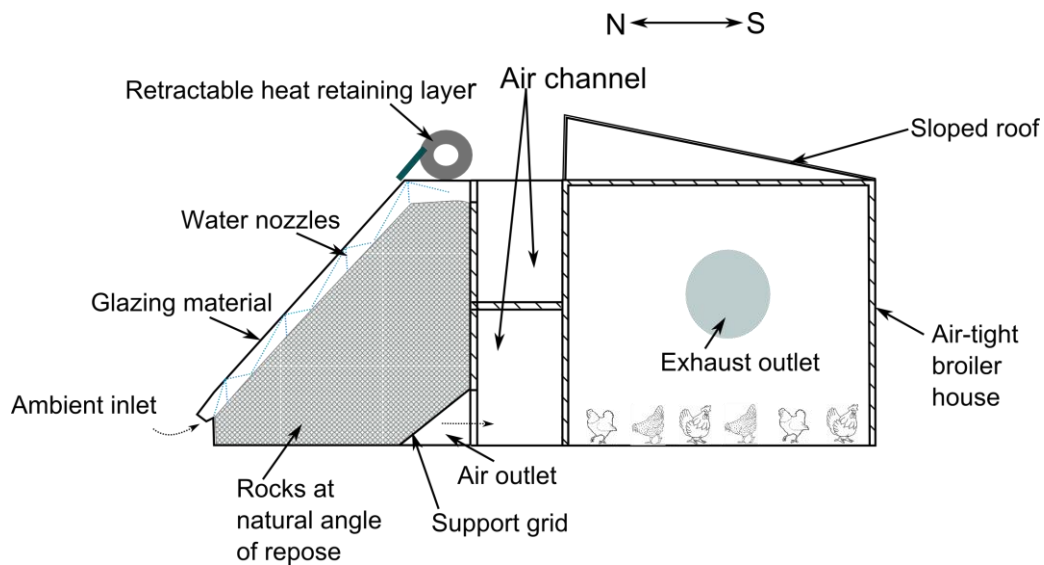
Figure J.2: Cross sectional view (A-A): HYDROSOL system connected to broiler house (B)

Appendix K: Measured data

An average reading for the thermocouples at the selected positions is used in the analysis. Figure K.1 and Figure K.2 shows air and rock temperature for different thermocouples at two selected positions in the rock bed during a typical experiment.
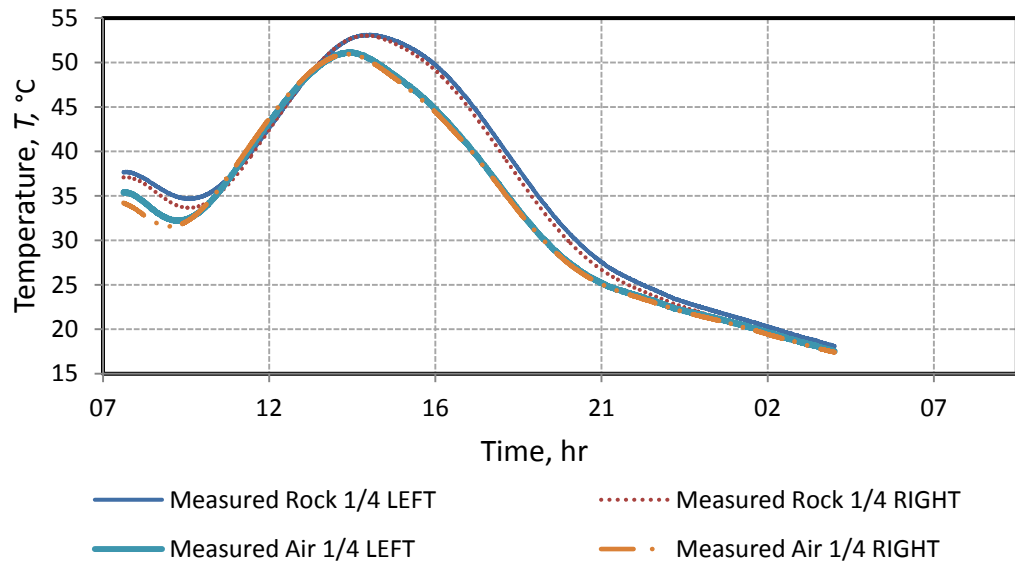
Figure K.1: Measured temperatures at *r* = 1.625 m
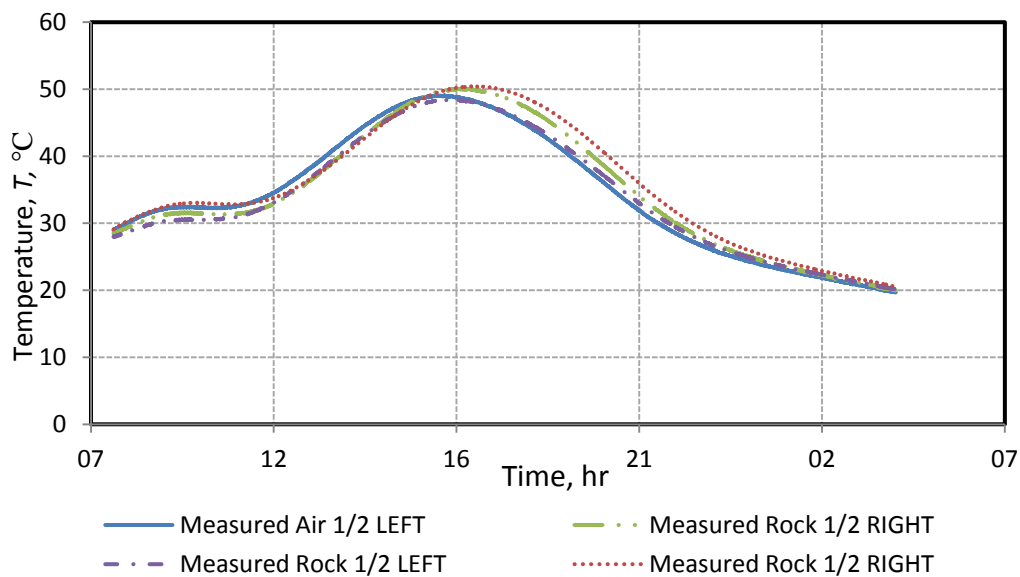
Figure K.2: Measured temperatures at *r* = 1.25 m

Appendix L: Active aggregate mines in RSA

The following list is obtained from the Council of Geoscience (2014) for all the active aggregate mines in South- Africa.

MINE NAME	MAGISTERIAL DISTRICT (PROVINCE)
565 MP	WATERBERG (LP)
A CROMHOUT - SUBUNGU MINE	EAST LONDON (EC)
AFRICA QUARRIES	UITENHAGE (EC)
AFRIMAT - BREWELSKLOOF	WORCESTER (WC)
AFRIMAT - COOKHOUSE EASTER CAPE	BEDFORD (EC)
AFRIMAT - DE KOP	VREDENBURG (WC)
AFRIMAT - DRIEFONTEIN	BREDASDORP (WC)
AFRIMAT - HAMLET	CERES (WC)
AFRIMAT - HARTEBEESFONTEIN	BRONKHORSTSPRUIT (GT)
AFRIMAT - KEURKLOOF	ROBERTSON (WC)
AFRIMAT - SMALBLAAR	WORCESTER (WC)
AFRIMAT - SPITSKOP	BRONKHORSTSPRUIT (GT)
AFRIMAT - STANFORD QUARRIES	HERMANUS (WC)
AFRISAM - COEDMORE	DURBAN (KZN)
AFRISAM - EIKENHOF	JOHANNESBURG (GT)
AFRISAM - FERRO	PRETORIA (GT)
AFRISAM - JUKSKEI	JOHANNESBURG (GT)
AFRISAM - LADYSMITH	KLIPRIVIER (KZN)
AFRISAM - MAMRE QUARRIES	MALMESBURY (WC)
AFRISAM - NEWCASTLE - ALPHA	NEWCASTLE (KZN)
AFRISAM - OLIFANTSFONTEIN	KEMPTON PARK (GT)
AFRISAM - PENINSULA QUARRIES	BELLVILLE (WC)
AFRISAM - PIETERMARITZBURG	PIETERMARITZBURG (KZN)
AFRISAM - RHEEBOK QUARRIES	MALMESBURY (WC)
AFRISAM - ROODEKRANS	KRUGERSDORP(GT)
AFRISAM - ROOIKRAAL	BRAKPAN (GT)
AFRISAM - UMLAAS ROAD	CAMPERDOWN (KZN)
AFRISAM - VERULAM QUARRIES	INANDA (KZN)
AFRISAM - ZEEKOEWATER	WITBANK (MP)
AFRISAM EAST RAND	SPRINGS (GT)
AFROVEST (PTY) LTD	PIETERSBURG (LP)
AL PLANT HIRE - FARM 520	EAST LONDON (EC)
AL PLANT HIRE TRUST - FARM 1338	EAST LONDON (EC)
AL PLANT HIRE TRUST - FARM 435	EAST LONDON (EC)
ALIWAL DOLERITE QUARRIES (PTY) LTD	ALIWAL NORTH (EC)
ALTON QUARRY	EAST LONDON (EC)
ALUINKRANTZ	ALEXANDRIA (EC)
AMASUNDU GRAVEL CC	MTUNZINI (KZN)
AMERSA ROCK PRODUCTS CC	LETABA (LP)
ANTONVILLA - BOELIE VISSER GROEP	SOUTPANSBERG (LP)

AP BECKER	WARMBAD (LP)
ARGENT INDUSTRIAL ENGINEERING(PTY)LTD	CALEDON (WC)
B & E INT (PTY) LTD - ERF 375	KIMBERLEY (NC)
B & E INTERN (PTY) LTD - DWAALFONTEIN	WITBANK (MP)
B & E INTERN (PTY) LTD - ROODEKRANS	BETHAL (MP)
B & E INTERNATION (PTY) LTD - KRANSPOORT	ERMELO (MP)
B COHEN VELLEFONTEIN	WARMBAD (LP)
BALLITO CRUSHERS	LOWER TUGELA (KZN)
BAZ-WAR TRADING CC	BEDFORD (EC)
BEAUMONT ESTON FARMERS ASSOCIATION	MAHLABATINI (KZN)
BECKER CRUSHERS	HARTSWATER (NC)
BEGANE QUARRIES	LOWER UMFOLOZI (KZN)
BENONI GOLD MINE (PTY) LTD	BENONI (GT)
BITOU QUARRIES	KNYSNA (WC)
BLESBOKFONTEIN	BRONKHORSTSPRUIT (GT)
BLOEMENDALSFONTEIN 704	MALMESBURY (WC)
BLUESTONE QUARRY	ESTCOURT (KZN)
BLUESTONES SAND AND STONE	BLOEMFONTEIN (FS)
BON ACCORD KLIPGROEF	PRETORIA (GT)
BOSPOORT 450 KR	WARMBAD (LP)
BOTSHABELO KLIPBREKERY	BOTSHABELO (FS)
BOWENITE MINE	NAMAKWALAND (NC)
BUFFELSFONTEIN GRAVEL MINE	RIVERSDAL (WC)
CANDERO MINING & CONSULTANTS CC	KLERKSDORP (NW)
CENTRAL AFRICA CRUSHERS (PTY) LTD	MESSINA (LP)
CENTRAL LAKE - MANTELLA TRADING	THABAZIMBI (LP)
CHIRUDINI BELEGGINGS CC - ANTONVILLA	SOUTPANSBERG (LP)
CIVIL & GENERAL	QUEENSTOWN (EC)
CLC TUTT	EAST LONDON (EC)
CLOGGS FORESTRY	UMVOTI (KZN)
CONCOR HOLDINGS - GROOTFONTEIN	SOMERSET EAST (EC)
CONCRETE MIX T/A NPC AGG- MARGATE DWY	PORT SHEPSTONE (KZN)
CORPCLO 1982 CC	QUEENSTOWN (EC)
CRADOCK QUARRY	CRADOCK (EC)
DE AAR STONE CRUSHERS	DE AAR (NC)
DE HOOP QUARRY BK	UITENHAGE (EC)
DENVER QUARRIES	PORT ELIZABETH (EC)
DF MALAN AGGREGATE	KURUMAN (NC)
DIE DAM QUARRY	BREDASDORP (WC)
DOORNKRAAL BORROWPIT	CULLINAN (GT)
DOORNLAAGTE	UITENHAGE (EC)
DROOGEHOUT NO 442	GORDONIA (NC)

L.2

DYSSELSRUST	BLOEMFONTEIN (FS)
EASTERN CAPE QUARRIES CC	NQAMAKWE (EC)
ECKRAAL QUARRIES	WONDERBOOM (GT)
EKURHULENI DOLOMITE - ZIMBIWA DOLOMIT	BENONI (GT)
ELANGENI BUILD IT - STATE LAND	UMTATA (EC)
ELSANA QUARRY (PTY) LTD	MALMESBURY (WC)
ESKAY CRUSHERS	PIET RETIEF (MP)
FAIRVIEW	CAMPERDOWN (KZN)
FELICIDAD CC	LETABA (LP)
FRIERSDALE NORTHERN CAPE	GORDONIA (NC)
FRIK GEYSER KLIP&SAND & MACHERO QUARR	GROBLERSDAL (MP)
FRONTIER QUARRY	ALBANY (EC)
FUNGUBABA TRADING CC	INGWAVUMA (KZN)
GANSBAAI GRUISMYN	HERMANUS (WC)
GEELHOUTBOOM	ALEXANDRIA (EC)
GLEN CRAIG QUARRY	ALBANY (EC)
GLENDORE SAND QUARRY - MOUNTAIN DALIA	PORT ELIZABETH (EC)
GOMES SAND CC	PRETORIA (GT)
GOODHOPE	UITENHAGE (EC)
GRAN SASSO QUARRY	CAPE (WC)
GRASSVALLEY CRUSHERS	POTGIETERSRUS (LP)
GREAT CORMORANT INVESTMENTS 113	MALMESBURY (WC)
GUMTREA	UITENHAGE (EC)
HAMMARS QUARRY	LOWER UMFOLOZI (KZN)
HARTENBOS QUARRY	MOSSEL BAY (WC)
HENQUE 4052 CC T/A PIKA MINING	BLOEMFONTEIN (FS)
HERMANUS GRAVEL MINE	CALEDON (WC)
HERMANUS RIVER GRAVEL (PINE BLOCK)	CALEDON (WC)
HERSCHEL SANDSTONE MINE	EAST LONDON (EC)
HIGHVELD CRUSHERS	STANDERTON (MP)
HOOIKRAAL GRUISGROEF	SWELLENDAM (WC)
HOWARDS CRUSHERS	WITBANK (MP)
IKWEZI QUARRIES	LIBODE (EC)
ILLOVU GOLDEN SANDS	UMBUMBULU (KZN)
IXOPO QUARRIES	IXOPO (KZN)
J DU PREEZ T/A TEKS DOLORIET	HIGHVELD RIDGE (MP)
JLJ LOGISTICS	CAPE (WC)
JOHBO	PRETORIA (GT)
JOHN SMIT - BOTHASVLEY	WARMBAD (LP)
JP MBETE AND SONS	BUTTERWORTH (EC)
JUNCTION 14 QUARRY MINE	BUTTERWORTH (EC)
KARIEGA QUARRY	ALEXANDRIA (EC)
KING WILLIAMS TOWN ROCK QUARRY	KING WILLIAM'S TOWN (EC)

KLIPFONTEIN SAND (PTY) LTD	KEMPTON PARK (GT)
KLU KLU HARD ROCK QUARRY	FORT BEAUFORT (EC)
KNOTT	PIETERSBURG (LP)
KRANTZHOEK QUARRY	ALEXANDRIA (EC)
KUIPERSBULT	WATERBERG(LP)
LAFARGE - BLUE ROCK QUARRY	EAST LONDON (EC)
LAFARGE - COEGAKOP EAST	PORT ELIZABETH (EC)
LAFARGE - EVANDER QUARTZITE CRUSHERS	HIGHVELD RIDGE (MP)
LAFARGE - KING WILLIAM'S TOWN QUARRY	KING WILLIAM'S TOWN (EC)
LAFARGE - KNYSNA QUARRY	KNYSNA (WC)
LAFARGE - MOREGROVE QUARRY	PORT ELIZABETH (EC)
LAFARGE - NELSPRUIT QUARRY	NELSPRUIT (MP)
LAFARGE - NINIANS GRANITE QUARRY	LOWER UMFOLOZI (KZN)
LAFARGE - OLIVE HILL QUARRY	BLOEMFONTEIN (FS)
LAFARGE - PEAK QUARRY	STELLENBOSCH (WC)
LAFARGE - POLOKWANE CRUSHERS	PIETERSBURG (LP)
LAFARGE - RICHARDS BAY QUARRY	LOWER UMFOLOZI (KZN)
LAFARGE - RIDGEVIEW QUARRY	PINETOWN (KZN)
LAFARGE - SALDANHA QUARRY	MALMESBURY (WC)
LAFARGE - STANGER QUARRY	LOWER TUGELA (KZN)
LAFARGE - STONETECH KOMATIPOORT	BABERTON (MP)
LAFARGE - STONETECH MACHADODORP	BELFAST (MP)
LAFARGE - TONGAAT QUARRY	INANDA (KZN)
LAFARGE - TYGERBERG QUARRY	BELLVILLE (WC)
LAFARGE - WHITE RIVER QUARRY	WITRIVIER (MP)
LAFARGE - WITFONTEIN QUARRY	GEORGE (WC)
LAMAN (PTY) LTD	TSOLO (EC)
LANCASTER QUARRIES - DUNDEE	DUNDEE (KZN)
LANCASTER QUARRIES - HARRISMITH	HARRISMITH (FS)
LANCASTER QUARRIES - HLUHLUWE	HLABISA (KZN)
LANCASTER QUARRIES - MARITZBURG	PIETERMARITZBURG (KZN)
LANCASTER QUARRIES - QWA QWA	HARRISMITH (FS)
LANCASTER QUARRIES - SCOTTBURGH	UMZINTO (KZN)
LANCASTER QUARRIES - UMFOLOZI	VRYHEID (KZN)
LANCASTER QUARRIES - VRYHEID	VRYHEID (KZN)
LEPHALALE AGGREGATES (PTY) LTD	WATERBERG (LP)
LESAKA CRUSHERS	RUSTENBURG (NW)
LEZMIN 2021 CC T/A K1 QUARRY	GEORGE (WC)
LOLO & LOLO - 359 KWT - 417 MP	KOMGA (EC)
LOLO & LOLO - ERF 106 KOMGA - 212 MP	KOMGA(EC)
LTA MARITZBURG QUARRIES	PIETERMARITZBURG (KZN)
LUGHAWE GRUISGROEF	GEORGE (WC)
LYTTELTON DOLOMITE MINE	PRETORIA (GT)

MAANDAGSKOP CRUSHER	MOSSEL BAY (WC)
MABALENI QUARRY	UMTATA (EC)
MACCSAND (PTY) LTD - ERF 13625	MITCHELLS PLAIN (WC)
MAKHULU QUARRY	KNYSNA (WC)
MAKUKUKWE VERVOER BK	POSTMASBURG (NC)
MAMELODI QUARRIES (PTY) LTD	BRONKHORSTSPRUIT (GT)
MANROTRADE SEVENTEEN T/A BLOEM BRICKS	BLOEMFONTEIN (FS)
MANTSOPA LOCAL MUNICIPALITY	LADYBRAND (FS)
MATSHELONI CONSTRUCTION	SOUTPANSBERG (LP)
MBOGOTO MINING	ALFRED (KZN)
MENTORSKRAAL FAM TRUST	HUMANSDORP (EC)
METRO QUARRIES (PTY) LTD	PORT ELIZABETH (EC)
MIDMAR CRUSHERS CC	LIONS RIVER (KZN)
MOKGAMELA MULTIMINERALS	DZANANI (LP)
MOOIFONTEIN GROEF	BATHURST (EC)
MOOINOOI STONE CRUSHERS CC	RUSTENBURG (NW)
MOSES NHLANHLA VUNDLA	NQUTU (KZN)
MT NOVAL TDG	BLOEMFONTEIN (FS)
MUKULA STONE CRUSHERS CO-OP LTD	THOHOYANDOU (LP)
MUNICIPAL DOLERITE QUARRY	KING WILLIAM'S TOWN (EC)
MUNICIPAL GRAVEL QUARRY	GORDONIA (NC)
MVUBU QUARRIES CC	EAST LONDON (EC)
MZINTLAVA QUARRIES	LUSIKISIKI (EC)
NANDONI QUARRY	MESSINA (LP)
NDWEDWE ROAD QUARRIES - T/A CANELANDS QUARRIES	INANDA (KZN)
NELSPRUIT CRUSHERS (ALKMAAR)	NELSPRUIT (MP)
NIGEL STONE CRUSHERS	NIGEL (GT)
NIRVANA CRUSHERS CC	SCHWEIZER - RENEKE (NW)
NYLSTROOM CRUSHERS	WATERBERG (LP)
OESTERBAAI - EASTERN CAPE	HUMANSDORP (EC)
OMV CRUSHERS	KIMBERLEY (NC)
OMV CRUSHERS - MARGARETSKAG	KLERKSDORP (NW)
OMV CRUSHERS - VIRGINIA AND MERRIESPRUIT	VIRGINIA (FS)
ONVERWACHT BORROW-PIT	PIETERSBURG (LP)
PAKAMA CRUSHER - VOGELENSANG	SOUTPANSBERG (LP)
PALMIET	CALEDON (WC)
PARYS GRUISGROEF	PARYS (FS)
PETRA QUARRY	BLOEMFONTEIN (FS)
PLATISTONE (PTY) LTD	SOUTPANSBERG (LP)
PONDOLAND QUARRIES CC	LUSIKISIKI (EC)
PORT NOLLOTH BOUMARK	NAMAKWALAND (NC)
PORT SHEPSTONE QUARRY	PORT SHEPSTONE (KZN)
PORTERSHOEK QUARRY	MOUNT CURRIE (KZN)

PORTLAND QUARRY	BELLVILLE (WC)
POTGIETER KLIPWERKE	HUMANSDORP (EC)
POWER PLANT HIRE	EAST LONDON (EC)
POWER RUSH	EAST LONDON (EC)
PPC - LAEZONIA QUARRY	PRETORIA (GT)
PPC - MOOIPLAAS DOLOMITE (PTY) LTD	PRETORIA (GT)
QUEENSTOWN QUARRY	QUEENSTOWN (EC)
QUIN CRUSH QUARRIES	RIVERSDAL (WC)
RADIUM CRUSHERS	WARMBAD (LP)
RAUMIX - RIETVLEI UMZIMKHULU	UMZIMKULU (EC)
RED HILL GRAVEL AND SAND MINE	MALMESBURY (WC)
REGINALD MARK BREMNER	KURUMAN (NC)
RIETKUIL QUARRY	UITENHAGE (EC)
RIETSPRUIT AGGREGATES	BETHAL (MP)
RIETSPRUIT STONE CRUSHERS	ERMELO (MP)
ROBBERG QUARRY	KNYSNA (WC)
ROODEKRANTZ 203	QUEENSTOWN (EC)
ROOIBERG STONE (PTY) LTD	WARMBAD (LP)
ROSSLYN QUARRY	WONDERBOOM (GT)
ROSSWAY QUARRY	PRETORIA (GT)
ROUWKOOP QUARRY	MALMESBURY (WC)
SAKHISIZWE QUARRIES (PTY) LTD	BOKSBURG (GT)
SAND VAN HEERDEN - KROONSTAD	KROONSTAD (FS)
SILVER RUBY TRADING 15 (PTY) LTD	UMTATA (EC)
SKIETKUIL QUARRIES CC	MURRAYSBURG (WC)
SKYSANDS	VEREENIGING (GT)
SOUTH COAST STONE CRUSHERS - MARBURG	PORT SHEPSTONE (KZN)
SPRINGFONTEIN	UITENHAGE (EC)
ST LUKES QUARRY	EAST LONDON (EC)
STEELSERV (PTY) LTD	NEWCASTLE (KZN)
STERKFONTEIN CRUSHERS (PTY) LTD	RUSTENBURG (NW)
STERKSPRUIT AGGREGATES	CAMPERDOWN (KZN)
STOCKVILLE QUARRIES	PINETOWN (KZN)
STONE & ALLIED - ELANDSRAND PLANT	OBERHOLZER (GT)
STONE & ALLIED - WELKOM	WELKOM (FS)
STONE RIDGE QUARRIES	EAST LONDON (EC)
STONEWELL QUARRY CC	MOUNT CURRIE (KZN)
STUTT QUARRIES	STUTTERHEIM (EC)
STUTT QUARRIES - MARTINDALE FARM	EAST LONDON (EC)
SUNSHINE CRUSHERS	DUNDEE (KZN)
SUPACRUSH (PTY) LTD	HUMANSDORP (EC)
SUPER STONE MINING (PTY) LTD	KIMBERLEY (NC)
SYFERGAT	UITENHAGE (EC)
TAU SEJELA MABU MEETSE LE LEKGWARA SU	PIETERSBURG (LP)
TL BOWLES	ALBANY (EC)

TOWERHILL QUARRY	KOMGA (EC)
TRANSKEI QUARRIES - BUTTERWORTH	BUTTERWORTH (EC)
TRANSKEI QUARRIES - UMTATA	LIBODE (EC)
TREGARON QUARRIES	UITENHAGE (EC)
TRICHARDT CRUSHERS	HIGHVELD RIDGE (MP)
TSITSIKAMMA	HUMANSDORP (EC)
UILKRAAL GRUISMYN	BREDASDORP (WC)
UITKOMS KLIPBREKER	THABA'NCHU (FS)
UMFOLOZI SUGAR PLANTERS LTD	HLABISA (KZN)
UMHLALI QUARRY	LOWER TUGELA (KZN)
UMSO CONSTRUCTION QUARRY	MT AYLIFF (EC)
UVUYO HOLDINGS (PTY) LTD	INANDA (KZN)
VAALBOSCHFONTEIN	WOLMARANSSTAD (NW)
VAALRIVIER SANDWERKE - GOEDEHOOP	CHRISTIANA (NW)
VADUBA INVESTMENTS CC - FARM 800	EAST LONDON (EC)
VADUBA INVESTMENTS CC - FARM 860	EAST LONDON (EC)
VAN EEDEN HOLDING TRUST	LOWER UMFOLOZI (KZN)
VAN ZYL QUARRY	MOSSEL BAY (WC)
VERWEERDE DOLERIET GRUISGROEF	GRAAFF-REINET (EC)
VLAKFONTEIN ROCK DUMP	NIGEL (GT)
VLAKTEPLAAS CRUSHERS	HUMANSDORP (EC)
VOLMOED QUARRIES	OUDSHOORN (WC)
VREDE	UITENHAGE (EC)
VRYBURG CRUSHERS CC	VRYBURG (NW)
VUKA CRUSHERS CC	WITRIVIER (MP)
WEARNE QUARRIES KLOOF	WESTONARIA (GT)
WEARNE QUARRIES NATAL - WILLOWSFONTEI	PIETERMARITZBURG (KZN)
WESTSIDE TRADING 534 (PTY) LTD	NIGEL (GT)
WG WEARNE - BETHLEHEM	BETHLEHEM (FS)
WG WEARNE - MAKHADO	SOUTPANSBERG (LP)
WG WEARNE - TZANEEN	LETABA (LP)
WG WEARNE - WEST DRIE GM CRUSHERS	RANDFONTEIN (GT)
WG WEARNE LTD - POLOKWANE QUARRY	PIETERSBURG (LP)
WILLOWS QUARRIES (PTY) LTD	PRETORIA (GT)
WP BOTHA	THEUNISSEN (FS)
XUME DISTRICT	PORT ELIZABETH (EC)
ZENZELE MINING	MOUNT CURRIE (KZN)
ZULULAND QUARRIES	LOWER TUGELA (KZN)
ZWARTEBOSCH QUARRY (PTY) LTD	HUMANSDORP (EC)
AFRIMAT - KLIPRUG	BELLVILLE (WC)
ALEXANDERFONTEIN SAND & GRAVEL	MALMESBURY (WC)
APPELSDRIFT SANDGAT	ROBERTSON (WC)
BOEKENHOUT SAND (PTY) LTD	CULLINAN (GT)
BOTTELFONTEIN SAND MINE	MALMESBURY (WC)

BUNDU SAND (PTY) LTD	PRETORIA (GT)
CLEWER SAND	WITBANK (MP)
CLUSTER SAND	RANDFONTEIN (GT)
COUNTERPOINT TRADING 70 - MAATJESFONTEIN	HOPEFIELD (WC)
CRUSHCO (PTY) LTD	KEMPTON PARK (GT)
GANSBAAI SANDMYN	HERMANUS (WC)
HEIDELBERG KLIPBREKERY	HEIDELBERG WC (WC)
INZULU (PTY) LTD	UITENHAGE (EC)
IRHAFU SAND	GRAAFF-REINET (EC)
IZINYONI TRADING 142 (PTY) LTD	BRONKHORSTSPRUIT (GT)
KALKFONTEIN / DOORNBULT / PELGRIMSHOOP	PIETERSBURG (LP)
MARINA CRETE SANDMINE	PORT SHEPSTONE (KZN)
MIDDENIN SANDGROEF DE JAGER	WITRIVIER (MP)
MILLING EQUIPMENT	SASOLBURG (FS)
MK SAND - TD VAN NIEKERK	UITENHAGE (EC)
MR AUST - NOOITGEDACHT SAND	CULLINAN (GT)
MR AUST - RIETVLEI SAND	PRETORIA (GT)
MR AUST - ROOIKOPJES	CULLINAN (GT)
MUCERA TRADING CC - SINEMBE	DURBAN (KZN)
MULDERSDRIFT	KRUGERSDORP (GT)
MULTISAND (PTY) LTD	PRETORIA (GT)
QUARRY CATS - LAEZONIA	PRETORIA (GT)
SPH SAND (PTY) LTD	PRETORIA (GT)
SR OLIFANT MINING	BARKLY WEST (NC)
SUIDPUNT SAND MINE	BREDASDORP (WC)
TAAIFONTEIN MINERAL INDUSTRIES (PTY)	BRONKHORSTSPRUIT (GT)
WG WEARNE - GROENPLAATS	RANDFONTEIN (GT)